

ADVERTIMENT. L'accés als continguts d'aquesta tesi queda condicionat a l'acceptació de les condicions d'ús establertes per la següent llicència Creative Commons:  <https://creativecommons.org/licenses/?lang=ca>

ADVERTENCIA. El acceso a los contenidos de esta tesis queda condicionado a la aceptación de las condiciones de uso establecidas por la siguiente licencia Creative Commons:  <https://creativecommons.org/licenses/?lang=es>

WARNING. The access to the contents of this doctoral thesis it is limited to the acceptance of the use conditions set by the following Creative Commons license:  <https://creativecommons.org/licenses/?lang=en>

Industrial PhD Thesis

Microwave Technology for Quantum Processors

David Eslava Sabaté

Codirector: Pedro de Paco Sánchez

Codirector: Pol Forn Díaz

PHD in Electronic and Telecommunication Engineering
Telecommunications Systems Department
Escola d'Enginyeria
Universitat Autònoma de Barcelona (UAB)

September 2023

Microwave Technology for Quantum Processors

by

David Eslava Sabaté

A dissertation submitted in partial satisfaction of the
requirements for the degree of
Doctor of Philosophy

in

Electronic and Telecommunication Engineering

in the

Escola d'Enginyeria
of the
Universitat Autònoma de Barcelona, UAB

,

Autumn 2023

The dissertation of David Eslava Sabaté, titled Microwave
Technology for Quantum Processors, is approved:

Date

Date

Date

Universitat Autònoma de Barcelona, UAB

Microwave Technology for Quantum Processors

Copyright 2023
by
David Eslava Sabaté

Abstract

Microwave Technology for Quantum Processors

by

David Eslava Sabaté

Doctor of Philosophy in Electronic and Telecommunication
Engineering

Universitat Autònoma de Barcelona, UAB

Microwave technology is an essential aspect of the construction and operation of quantum computers. Quantum computers have the potential to revolutionize many fields by providing exponential improvements in computational power and efficiency. In this doctoral thesis, the author discusses the development and validation of microwave cryogenic interfaces, such as superconducting coaxial cables and microwave packaging, as well as the design of the quantum processor unit (QPU) chips, including single qubit and multi-qubit prototypes. Additionally, the thesis covers the system design of the quantum computer systems and interconnects, and the development of electronics, mechanical, and software solutions for high frequency readout of the QPU. The author also presents a case study on the integration of these QPU chips into a functional quantum computer prototype and discusses the results of tests performed on this prototype. The prototype was able to successfully demonstrate acceptable decay time and readout fidelity, a critical requirement for the operation of a scalable quantum computer. The author also discusses the future potential applications of quantum computers and the challenges that must be overcome for their widespread adoption.

Resumen

La tecnología de microondas es un aspecto esencial en la construcción y operación de las computadoras cuánticas. Las computadoras cuánticas tienen el potencial de revolucionar muchos campos al proporcionar mejoras exponenciales en la potencia y eficiencia computacional. En esta tesis doctoral, el autor discute el desarrollo y validación de interfaces criogénicas de microondas, como cables coaxiales superconductores y encapsulados compatibles a frecuencias de microondas, así como el diseño de chips de procesador cuántico (QPU), incluyendo prototipos de un solo qubit y múltiples qubits. Además, la tesis cubre el diseño del sistema de computadora cuántica e interconexiones, y el desarrollo de soluciones electrónicas, mecánicas y de software para la lectura de alta frecuencia del procesador cuántico. El autor también presenta un estudio de caso sobre la integración de estos chips QPU en un prototipo de ordenador cuántico funcional y discute los resultados de las pruebas realizadas en este prototipo. El prototipo pudo demostrar con éxito un tiempo de decaimiento y fidelidad de lectura aceptables, un requisito crítico para la operación de una computadora cuántica escalable. El autor también discute las posibles aplicaciones futuras de las computadoras cuánticas y los desafíos que deben superarse para su adopción generalizada.

Resum

La tecnologia de microones és un aspecte essencial en la construcció i operació dels ordinadors quàntics. Els ordinadors quàntics tenen el potencial de revolucionar molts camps proporcionant millores exponencials en la potència i eficiència computacional. En aquesta tesi doctoral, l'autor discuteix el desenvolupament i validació d'interfícies criogèniques de microones, com ara cables coaxials superconductors i encapsulats compatibles a freqüències de microones, així com el

disseny de xips d'unitat de processador quàntic (QPU), incloent prototips d'un sol qubit i múltiples qubits. A més, la tesi cobreix el disseny del sistema d'ordinadors quàntics i interconnexions, i el desenvolupament d'electrònica, mecànica i solucions de programari per a la lectura d'alta freqüència del processador quàntic. L'autor també presenta un estudi de cas sobre la integració d'aquests xips QPU en un prototip d'ordinador quàntic funcional i discuteix els resultats de les proves realitzades en aquest prototip. El prototip va poder demostrar amb èxit un temps de decaïment i fidelitat de lectura acceptables, un requisit crític per a l'operació d'un ordinador quàntic escalable. L'autor també discuteix les possibles aplicacions futures dels ordinadors quàntics i els desafiaments que s'han de superar per a la seva adopció generalitzada.

To my grandparents.

Contents

List of Figures	v
1 Quantum Computing: From Science Fiction to Reality	1
1.1 Introduction to Quantum Computing Main Components	3
1.2 Motivation and Purpose of the Thesis	6
1.2.1 Thesis outline	7
2 Exploring the Fundamentals of Quantum Computing: From Qubits to Purcell Filters	9
2.1 Quantum Information Layer of a Quantum Computer	10
2.1.1 Introduction to the Bloch Sphere	12
2.1.2 Introduction to One-Qubit Gates	13
2.1.3 Describing Quantum States with the Density Matrix	16
2.2 Quantum Physical Layer of a Quantum Computer . .	16
2.2.1 Utilizing Superconducting Materials for Quantum Computing	17
2.2.2 The Josephson Junction	18
2.2.3 The Transmon Qubit	21
2.3 Noise and Decoherence in Quantum Computing . . .	25
2.3.1 Understanding Qubit Decay time T_1	28
2.4 Microwave Resonators for Quantum Bits: Dispersive Readout Technique	29

2.4.1	Measuring Quantum Information in the Strong Coupling Regime	32
2.5	Enhancing Superconducting Qubit Measurements with the Purcell Filter	36
3	Effective Control and Measurement Strategies for Superconducting Qubits in Quantum Computing	43
3.1	Effective Control and Measurement Strategies for Qubits in Quantum Computing	44
3.1.1	Utilizing IQ Mixers for Precise Quantum State Control and Measurement	48
3.1.2	Uncovering Qubit State through Digital Signal Processing	54
3.2	Elevating Quantum Computing: Qilimanjaro's OS Innovation	58
3.3	Enhancing Quantum Computing Performance through Advanced Microwave Packaging Techniques	61
3.3.1	Optimizing a 12 Port PCB Housing for Quantum Computing	65
3.3.2	Design and Characterization of a 12 Port PCB for Quantum Computing Applications	69
4	Resonator Design for Quantum Computing: 3D Transmon in a Rectangular Cavity Resonator and Transmission Line Resonators	73
4.1	Enhancing Qubit Coherence with a 3D Transmon in a Rectangular Cavity Resonator: Design and Simulation	74
4.2	Exploring the Capabilities of Transmission Line Resonators for Quantum Computing	78
4.2.1	Optimizing Resonator Functionality through Reflection Measurements and Data Fitting	84
5	Data Analysis and Findings	89
5.1	Characterizing a Qubit: Punchout and Two-Tone Spectroscopy	90

5.2	Unveiling Quantum Control: Optimizing Gates in Transmon Qubits	93
5.3	Precision Measurements of High-Q Aluminum Resonators at 10 mK	103
5.4	Purcell Filters for Quantum Computing: Exploring the use of SAW Filters	105
5.5	Evolution of the Lab and Advancements in Quantum Technology in Spain	116
6	Conclusions and Future Work	119
6.1	Microwave Engineering challenges in Superconducting qubit Quantum Computing	122
	Bibliography	127
A	Crafting Cryogenic Cables with NbTi Superconductors for Quantum Processing Units	137
A.0.1	Process followed for Assembling superconducting high quality NbTi coaxial cables	138
B	List of Author's Contributions	145
B.1	International Congress	145

List of Figures

1.1	Quantum Computer main components	5
2.1	Bit vs. qubit possible states	12
2.2	Critical temperature in superconductor	18
2.3	Josephson Junction	20
2.4	Transmon and eigenenergies	25
2.5	Qubit state decay over time	29
2.6	Dispersive readout circuit hanger resonator	31
2.7	Dispersive readout measurement	34
2.8	Dispersive readout with Purcell filter	38
2.9	Purcell filter competitive matrix	42
3.1	Control electronics system diagram for a 3D transmon	45
3.2	Qubit control pulse	48
3.3	IQ mixer	50
3.4	IQ modulation phasor	51
3.5	Qubit measure constellation	53
3.6	Digital signal processing	57
3.7	Software layer stack	59
3.8	MW packaging of the processor chip	62
3.9	Cryogenic setup layout	63
3.10	Housing of the PCB	66
3.11	PCB housing resonances	68
3.12	PCB testbenches simulations	71

4.1	3D transmon design	75
4.2	3D transmon circuit	77
4.3	CPW geometry	81
4.4	Multi-qubit chip	83
4.5	Resonator fit	87
5.1	Punchout measurement	91
5.2	Qubit spectroscopy measurement	94
5.3	Rabi oscillations measurement	96
5.4	Decay time measurement	99
5.5	Fidelity measurement	102
5.6	Al resonators internal quality factor validation	104
5.7	Thin film SAW resonator microscope picture	108
5.8	Commercial BAW performance	109
5.9	Quality factor from SAW resonator	110
5.10	SAW performance vs temperature	112
5.11	Shift of f_a and f_r vs temperature.	113
5.12	Out of band thin film SAW filter.	115
5.13	Lab evolution over the years.	118
6.1	M qubit setup diagram	126
A.1	Assembled cables measurements	143

Preface

This doctoral thesis was developed over the course of three years under the AGAUR scholarship for industrial PhDs, in a collaboration between the Autonomous University of Barcelona (UAB) and Qilimanjaro Quantum Tech, S.L. Throughout this journey, I have metamorphosed from a microwave engineer to a quantum systems engineer.

The increasing demands of larger quantum processors have led to a shift in the community's focus from purely scientific discovery to the development of new engineering abstractions for the design, control, and readout of multi-qubit quantum systems. This has given rise to a new field called quantum engineering, which aims to bridge the basic sciences, mathematics, and computer science with traditional engineering disciplines.

At Qilimanjaro, we are a full stack quantum computer company, meaning that we not only develop quantum algorithms to solve our clients' problems, but also build the entire stack of a quantum computer, from the processor to the control software. This work requires collaboration between various disciplines, including theoretical physicists, experimental physicists, software engineers, electrical engineers, and mechanical engineers.

As part of this project, I have played a dual role as both a system engineer and a hardware development engineer in the ambitious goal of building the first quantum computer in Southern Europe. This transition to a rapidly evolving industry, which is largely driven by academia, has presented many challenges as we work to define and establish tools, processes, and certifications. However, my previous experience in research and development projects has helped me navigate these challenges and prepare for this project.

I believe we are on the cusp of another industrial revolution with the emergence of artificial intelligence and a shift in the paradigm of computation. The future looks bright, and I am excited to be a part of it.

If you have any questions or feedback about this thesis, please feel free to contact me at either david.eslava@qilimanjaro.tech or david.eslavasabate@gmail.com. I welcome all inquiries.

Acknowledgments

I am deeply grateful to the many individuals who have contributed to this work and played a crucial role in shaping me into the person and professional I am today. My former colleagues at Idneo, specially Eduard Ametller and Marc Guijosa for their guidance on systems engineering protocols and for their reminders to stay positive.

This work was made possible through the economic support of Pla de Doctorats Industrials from Departament de Recerca i Universitats de la Generalitat de Catalunya, specifically through the DI grant 2020 DI 040. David López's expertise, support, and dedication to keeping the lab running smoothly have been essential, and I also extend my appreciation to Albert Solana and the SW team for their contributions to developing the qililab infrastructure and for answering my questions.

I am also grateful to my lab mates at IFAE for their tireless efforts in keeping the lab running smoothly. A special thanks goes to Yifei Chen for allowing me to use some of her beautiful microscope chip images in this work.

Finally, I owe a debt of gratitude to my supervisors Ramiro Sagastizabal and Daniel Szombati for their unwavering guidance and support throughout this process. I would also like to express my appreciation to Qilimanjaro and Victor Canivell for providing me with this opportunity and to Manel Martínez for teaching me about project management and giving me the chance to be a system engineer.

I am immensely grateful to my exceptional team, including David Feldstein, Anna Moreso, and Amanda Scoles, for their unwavering dedication and remarkable progress in achieving our goals in just three months. Additionally, I extend my heartfelt thanks to Eloi Guerrero and Lluís Acosta for their invaluable support, technical expertise, and generous provision of SAW resonators, which played a vital role in our research.

Finally, I would like to give a special mention to my thesis co-directors Pedro de Paco and Pol Forn Díaz for their endless patience,

mentorship, and trust in me. They have truly taught me the meaning of research and have guided me through every step of this work.

I would also like to thank my family for their love and support during the challenging times of this mental marathon. Irene, thank you for always putting a smile on my face and for your patience and understanding when we had to put our plans on hold while I worked on this thesis. Your support has meant the world to me.

Chapter 1

Quantum Computing: From Science Fiction to Reality

“Devs is a highly secretive, cube-shaped laboratory with an exceedingly powerful computer at its center. This quantum computer is able to analyze the variables of absolutely everything, living or inanimate, down to an atomic level. By doing so, it can construct an accurate simulation of how that object or living thing came to be and where it will eventually end up, therefore projecting past and future events like a time traveling crystal ball. From roaming dinosaurs to Christ’s crucifixion, the Devs team can view it all. As far as they’re concerned, this all-seeing machine is now effectively God.” -*Devs 2020’s TV miniseries synopsis.*

Devs is a mind-bending science fiction series that explores the limits of simulation technology and raises thought-provoking questions about the nature of reality. As we follow the story, we are left to wonder: What are the current applications for simulations? How can we overcome the limitations of today’s simulations? Can life, the universe, and existence itself be simulated, making everything predetermined or are we simply participating in an illusion, watching life

unfold before our eyes?

I can answer to the first two questions. It is with great interest that we consider the application of high performance computing (HPC) to various fields of science and engineering in order to address complex problems and advance our understanding of the world around us. These state-of-the-art HPC machines, like the Barcelona Supercomputing Center-Centro Nacional de Supercomputación (BSC-CNS), are equipped with thousands of CPUs and GPUs, and they are capable of running simulations and calculations that would be impossible with traditional computers. Just a few examples of the work that the BSC supercomputer has been using for in the last years include: discovering new drugs to fight diseases like SARS-CoV-2, studying the effects of radiation on DNA, simulating experiments in particle physics and analyzing vast amounts of data from satellite missions and scientific instruments. Essentially, supercomputers allow scientists and engineers to perform *in silico* experiments that are too expensive, dangerous, or simply impossible to conduct in the real world. By harnessing the power of computation, we are able to accelerate the pace of scientific and engineering progress like never before.

As our need for more powerful computing continues to grow, technology is constantly making devices smaller and smaller. According to Moore's Law, we can expect to see transistors as small as 100 nanometers in 2010, 10 nanometers in 2030, and even 1 nanometer in 2050 - which is the size of a single molecule! However, this trend is predicted to reach its limits by 2036 [73], and some problems known as NP-hard problems can take millions of years to solve even on the most advanced supercomputers [44]. But there may be hope on the horizon: quantum computing has the potential to revolutionize the way we approach these challenges. In 2019, quantum computation was demonstrated to solve a problem that would take 10,000 years for 100,000 desktop computers to solve in just 3 minutes and 20 seconds [37]. This incredible breakthrough shows the potential for quantum computers to solve problems that would otherwise be insurmountable

with classical computers.

Quantum computers have the potential to revolutionize the way we approach complex combinatorial problems, such as database search algorithms and prime factorization. While traditional computers, including supercomputers, struggle to store and analyze all the possible combinations, quantum computers exploit the principles of entanglement and superposition to perform these tasks exponentially faster. This has led to the development of a range of exciting new applications for quantum computers, including weather forecasting, drug development, supply chain logistics, cryptography, fraud detection, and capital allocation.

At the core of quantum computing is the ability to store and process information using quantum states of matter and quantum gate operations, enabling us to "program" quantum interference and unlock new capabilities. Some companies, like Qilimanjaro Quantum Tech [13], are already offering cloud access to their quantum computers and customized quantum algorithm solutions for these types of problems. As quantum computers continue to improve, the possibilities are endless

1.1 Introduction to Quantum Computing Main Components

Quantum computing is an emerging field with the potential to revolutionize numerous industries through its exponential advancements in computational power and efficiency. Present-day QPUs are still in a nascent state, rendering them practically ineffective for practical applications. However, drawing inspiration from the evolution of classical computing, we can anticipate significant progress in QPUs over time, leading to increased computational capabilities, akin to the development of CPUs from the 4-bit Intel 4004 to the modern-day 64-bit multicore microprocessors like the Intel i7. While challenges such as qubit errors persist, it is crucial to recognize the advantages

of quantum computing, including its low power consumption, which presents substantial cost and environmental benefits. Notably, a few companies like Qilimanjaro Quantum tech and IBM are already utilizing quantum computers, such as IBM's 433-qubit processor accessible via the cloud [33], demonstrating the practical implementation of this technology in certain domains.

The hardware of a superconducting qubit quantum computer [30] could be divided into three main systems: the refrigeration system, the control electronics system, and the QPU system. The refrigeration system is necessary to keep the qubits at the extremely low temperatures needed to operate, while the control electronics system handles the manipulation and measurement of quantum states. The QPU system, made up of qubits, is the core of quantum computation, storing and controlling quantum states of matter. The main components for each of these systems can be observed in Fig. 1.1.

To fully understand the capabilities and applications of quantum computers, it is important to have a basic understanding of quantum information, quantum states, superconducting materials, and quantum physics. A good resource for this is [68], which provides an overview of quantum computation and quantum information. As we delve deeper into this exciting technology in the following chapters, we will explore the potential for quantum computers to transform the way we approach complex problems and advance our understanding of the world around us.

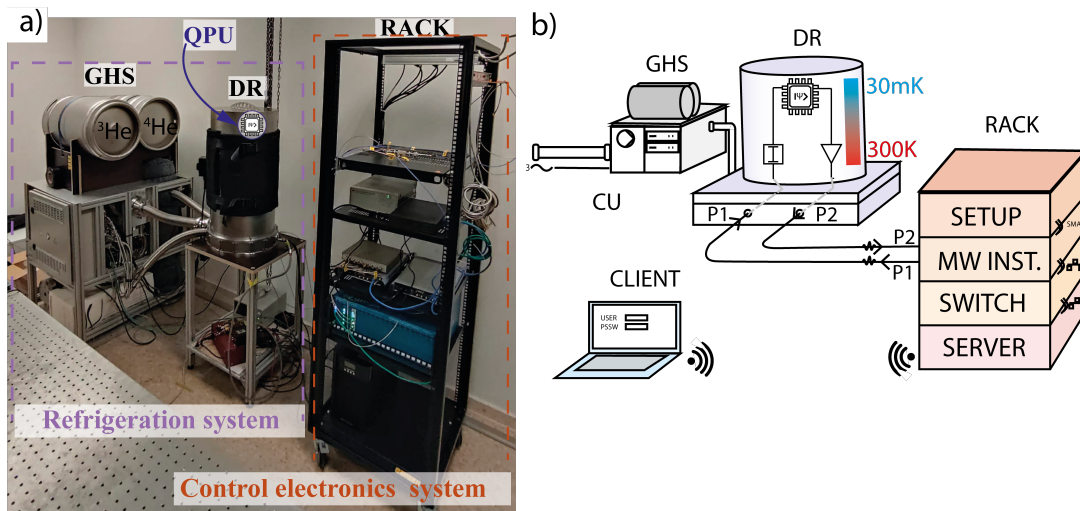


Figure 1.1: At the heart of the setup is the refrigeration system, which is responsible for maintaining the extremely low temperatures needed to run a quantum processing unit (QPU). The refrigeration system consists of a Gas Handling System (GHS) that holds and circulates $^3\text{He}/^4\text{He}$ gases, a Control Unit (CU) that manages pressures and directs valves, and a Dilution Refrigerator (DR) that houses the QPU system and its cryogenic components. In addition to the refrigeration system, the quantum computer setup includes a control electronics system, connected with the QPU through microwave cabling and cryogenic components orchestrated by the Software at the server that enables remote connections with clients sending quantum algorithms. (a) Picture of one of Qilimanjaro's lab quantum computer system. (b) Simplified schematic representation of the system in (a).

1.2 Motivation and Purpose of the Thesis

In 1994, Peter Shor provided a practical demonstration of the capabilities of quantum computers by showing that they could factor large numbers exponentially faster than classical computers [85]. However, at that time, the technology required to construct even a basic element of a quantum computer, a quantum bit (qubit), was not yet available. By 2019, over 100 academic groups and laboratories around the world were actively researching the design, construction, and manipulation of qubits [40].

Throughout this work, I have played a mix of roles as both a system engineer and a hardware development engineer at Qilimanjaro Quantum Tech, S.L., contributing to the novel project of building the first quantum computer in southern Europe. Some of my specific responsibilities have included collaborating with scientists to understand and refine control and readout requirements, working with software engineers to develop software for automated testing and calibration of complex quantum processors, developing and implementing measurement techniques to benchmark control and readout performance of superconducting quantum systems, designing, modeling, fabricating, and characterizing cryogenic and microwave (MW) components and infrastructure used in the construction of scalable quantum computers, contributing to project risk assessment through the completion of a DFMEA study and the development of contingency plans, providing progress and issue tracking control and communication. I have also been involved in product technical requirements gathering and analysis, interfacing with key stakeholders, and applying technical proficiency across different stages of the project life cycle, including requirements elicitation, system architecture definition, design, and development.

The ultimate goal of this work was to build the quantum computer architecture, integrate it into functional prototypes, and test and validate these prototypes. From 2020 to 2023, we have built three

quantum computer prototypes in Bellaterra, one in Abu Dhabi with the collaboration of the Technology Innovation Institute (TII), and we are currently building two more at the Barcelona Supercomputing Center (BSC). This thesis covers the system design of the quantum computer systems and interconnects, the development of electronics, mechanical, and software solutions for high frequency readout of the QPU, the design of the first QPU prototypes, and the validation of these prototypes.

1.2.1 Thesis outline

This thesis embarks on a comprehensive exploration of the dynamic field of quantum computing, with a specific focus on identifying engineering solutions and undertaking the characterization and design of crucial components spanning electronics, mechanics, microwaves, and software. To better understand the capabilities and applications of quantum computers, we start by introducing basic concepts for non-quantum engineers in *Chapter 2*, including the information layer of quantum computers, quantum states, and the use of superconductors to achieve qubits. We continue by reviewing the literature on qubit readout, specifically the state of the art of Purcell filters. We also present a preliminary study on the potential synergy between SAW filter technology and Purcell filters in the readout chain of the QPU.

Chapter 3 presents the proposed architecture for the control electronics system and signal processing using IQ modulation, including the main layers of the software we developed to benchmark the performance of the QPUs for quantum computers. We also discuss the design and validation of microwave cryogenic interfaces, such as superconducting coaxial cables and microwave packaging.

In *Chapter 4*, we present the design of the QPU chips we developed, including a single qubit prototype and a multi-qubit chip architecture. The single qubit is a 3D transmon and the multiqubit chip presents qubit to qubit interconnection with resonators. We

show some simulations and design parameters on those resonators.

Chapter 5 showcases the results of our performance benchmark on the QPU prototypes, including measurement protocols for key metrics for qubits and readout quality as the qubit decay time or the readout fidelity. We also show measurements of the designed resonators both CPW (CoPalanar Waveguide) resonators for qubit readout and the SAW resonator studied for the Purcell filter study. Finally, in *Chapter 6*, we draw conclusions from our measurements and propose future work.

Chapter 2

Exploring the Fundamentals of Quantum Computing: From Qubits to Purcell Filters

In this chapter, we provide a comprehensive introduction to the fundamental concepts of quantum computing for non-quantum engineers. We start by delving into the quantum information layer, where we explain the Bloch Sphere representation of quantum states, the importance of one-qubit gates in quantum operations, and the use of the density matrix for characterizing quantum information. Moving to the physical layer, we highlight the significance of superconducting materials in achieving qubits, focusing on the Josephson junction and its role in realizing the transmon qubit. We also address the challenges of noise and decoherence in quantum computing, particularly examining qubit decay time (T_1). Additionally, we explore microwave resonators and the dispersive readout technique for measuring quantum information. Lastly, we investigate the potential of Purcell filters in improving superconducting qubit measurements, aiming to enhance readout fidelity and the overall performance of

the quantum processing unit (QPU). This chapter lays the groundwork for a better understanding of the fundamental components of quantum computing and their importance in quantum information processing.

2.1 Quantum Information Layer of a Quantum Computer

In this section, we delve into the fundamental building block of a quantum computer: the quantum bit, or qubit. While a classical bit can be thought of as a switch with two possible positions (either 0 or 1), a qubit is more similar to a dial on a radio, Fig. 2.1a. Just like a dial can be turned to various positions to tune into different radio stations, a qubit can represent a range of states through a property known as superposition. This allows quantum computers to perform calculations that are not possible on classical computers. However, when the state of a qubit is measured, the quantum state collapses into one of its possible two states, $|0\rangle$ or $|1\rangle$.

To represent the quantum state of a qubit, we use the concept of a state vector, or ket. The notation $|0\rangle$ and $|1\rangle$ is used to refer to the quantum states. This is called Dirac or "bra-ket" notation. By using an orthogonal basis, we can express the state of a qubit in terms of a linear superposition of its basis states [68]

$$|0\rangle = \begin{pmatrix} 1 \\ 0 \end{pmatrix} \quad (2.1)$$

and

$$|1\rangle = \begin{pmatrix} 0 \\ 1 \end{pmatrix}. \quad (2.2)$$

In ket notation, an arbitrary quantum state is expressed using a column vector with complex coefficients. The squared magnitudes of the complex coefficients in the state vector represent the probabilities

of measuring a particular outcome. Given a pure qubit state $|\psi\rangle$, it can be expressed as a coherent superposition of the basis states, with probability amplitudes $|\alpha|^2$ and $|\beta|^2$

$$|\psi\rangle = \alpha |0\rangle + \beta |1\rangle = \alpha \begin{pmatrix} 1 \\ 0 \end{pmatrix} + \beta \begin{pmatrix} 0 \\ 1 \end{pmatrix} = \begin{pmatrix} \alpha \\ \beta \end{pmatrix}. \quad (2.3)$$

Let's take the example of a quantum state, represented as $|\psi\rangle = \begin{pmatrix} \frac{1}{\sqrt{2}} \\ \frac{1}{\sqrt{2}} \end{pmatrix}$. This means that there is a 50% chance of getting a measurement result of 1 and a 50% chance of getting a measurement result of 0. You can think of this like flipping a coin, where the outcome is undetermined until the coin is caught. Similarly, the measurement result of a quantum state in superposition is undetermined until the state is measured, collapsing it into one of the possible states. To perform multiple measurements on a quantum state, we repeat the measurement process independently. In this case, we would perform consecutive measurements on the same qubit. After each measurement, the quantum state collapses to one of the possible outcomes, either 0 or 1. By repeating this process many times, we can obtain statistical information about the measurement outcomes. In this example, if we perform numerous measurements on the same qubit prepared in the state $|\psi\rangle$, we would observe that approximately 50% of the measurements result in 0 and 50% result in 1. The statistical nature of quantum measurements allows us to infer probabilities based on a large number of repeated measurements.

Understanding the fundamentals of qubits and quantum states serves as a foundation for comprehending the operation of quantum computers and the transformative potential they offer in various domains, including cryptography and optimization. While it is true that a deep understanding of qubits and quantum states is not the sole requirement for grasping the intricacies of quantum computers, it plays a significant role in building a solid conceptual framework.

2.1.1 Introduction to the Bloch Sphere

Qubit states are geometrically represented using the Bloch sphere, Fig. 2.1b. In this representation, the probabilities of the two quantum states are represented by the points on the surface of the sphere, with $\alpha = \cos\frac{\theta}{2}$ and $\beta = e^{i\varphi}\sin\frac{\theta}{2}$ [68]. Where θ represents the altitude angle and φ represents the azimuth angle, being $e^{i\varphi}$ the physically significant relative phase.

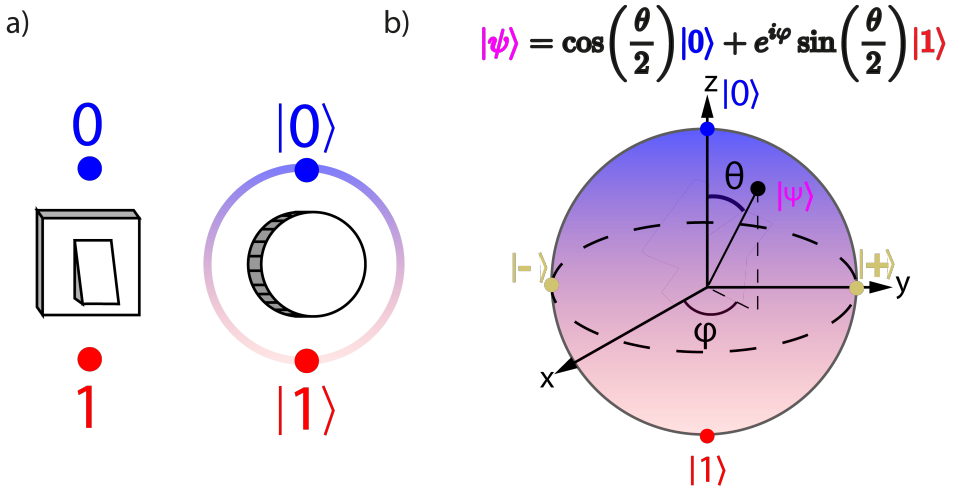


Figure 2.1: (a) Qubit vs bit possible states simplified concept as the number of possible states. (b) Bloch sphere representation of a quantum state $|\psi\rangle$ [68].

Using this representation, we can see that when $\theta = 0$ and $\varphi = 0$, north pole;

$$\alpha = \cos\frac{\theta}{2} = 1, \beta = \sin\frac{\theta}{2} = 0 \longrightarrow |\psi\rangle = \begin{pmatrix} 1 \\ 0 \end{pmatrix} = |0\rangle$$

and when $\theta = \pi$ and $\varphi = 0$, south pole;

$$\alpha = \cos\frac{\theta}{2} = 0, \beta = \sin\frac{\theta}{2} = 1 \longrightarrow |\psi\rangle = \begin{pmatrix} 0 \\ 1 \end{pmatrix} = |1\rangle .$$

In a similar way and by convention, the opposite states in the x-axis are called $|+\rangle$ and $|-\rangle$, also shown in Fig. 2.1.

Then, if $\theta = \frac{\pi}{2}$ and $\varphi = 0$;

$$\alpha = \cos \frac{\theta}{2} = \frac{1}{\sqrt{2}}, \beta = \sin \frac{\theta}{2} = \frac{1}{\sqrt{2}} \longrightarrow |\psi\rangle = \frac{1}{\sqrt{2}} \begin{pmatrix} 1 \\ 1 \end{pmatrix} = |+\rangle$$

and when $\theta = \pi$ and $\varphi = \pi$;

$$\alpha = \cos \frac{\theta}{2} = 0, \beta = e^{i\pi} \sin \frac{\theta}{2} = -\frac{1}{\sqrt{2}} \longrightarrow |\psi\rangle = \frac{1}{\sqrt{2}} \begin{pmatrix} 1 \\ -1 \end{pmatrix} = |-\rangle$$

Pure qubit states, represented by points on the surface of the Bloch sphere, can be transformed using unitary operations or rotations. One such operation is the X gate, which is the quantum equivalent of the classical NOT gate. The X gate corresponds to a rotation of 180° around the x-axis on the Bloch sphere.

When applied to a qubit in a pure state, the X gate flips the state of the qubit across the x-axis, effectively changing a state pointing to the right side of the sphere to the opposite side. For example, if the qubit is initially in the state $|0\rangle$, representing the point $(1, 0, 0)$ on the Bloch sphere, the application of the X gate would transform it to the state $|1\rangle$, represented by the point $(-1, 0, 0)$ on the sphere. Similarly, if the qubit is initially in the state $|1\rangle$, the X gate would flip it to the state $|0\rangle$.

In addition to pure states, the Bloch sphere can also represent mixed states, which occur when energy relaxation or dephasing into the environment takes place. These states are represented by points inside the sphere [92].

2.1.2 Introduction to One-Qubit Gates

In this subsection, we will introduce one qubit gates, which are fundamental building blocks of quantum circuits. Quantum gates are represented by unitary matrices, and a gate that operates on N qubits is represented by a $2^N \times 2^N$ unitary matrix. The quantum states that the gates act upon are vectors in 2^N complex dimensions, and quantum gates act on these states to produce new quantum

states. The universality theorem [68] in quantum computing states that any quantum circuit can be broken down into one- and two-qubit gates. These gates serve as fundamental building blocks, allowing researchers to construct complex quantum algorithms and explore diverse computations that surpass classical computing capabilities.

To calculate the output of a series of operations, we perform a matrix product. For example, if we have an initial state $|\psi\rangle$ and we apply two gates, U and V , with a final state $|\phi\rangle$, we can represent this as:

$$|\psi\rangle \text{ --- } \boxed{U} \text{ --- } \boxed{V} \text{ --- } |\phi\rangle$$

And calculate it as:

$$|\phi\rangle = VU |\psi\rangle$$

Note that the order is inverted because in a matrix product, the right-most matrix is the first one applied to the state $|\psi\rangle$.


One of the most common types of quantum gates is the one qubit gate, which operates on a single qubit. The X gate, for example, has a matrix representation of $X = \begin{bmatrix} 0 & 1 \\ 1 & 0 \end{bmatrix}$. When applied to a qubit state $|\psi\rangle = \begin{pmatrix} \alpha \\ \beta \end{pmatrix}$, it produces a new qubit state $|\phi\rangle = \begin{pmatrix} \beta \\ \alpha \end{pmatrix}$. This can also be written as:

$$|\phi\rangle = X |\psi\rangle = X \begin{pmatrix} \alpha \\ \beta \end{pmatrix} = \begin{pmatrix} \beta \\ \alpha \end{pmatrix}. \quad (2.4)$$

In other words, $X (\alpha |0\rangle + \beta |1\rangle) \rightarrow \alpha |1\rangle + \beta |0\rangle$.¹

In quantum circuit notation, this operation can be represented as:

$$|\psi\rangle \text{ --- } \boxed{X} \text{ --- } |\phi\rangle$$

Measurement in quantum circuits is denoted by . The classical bit m denotes the measurement result (either 0 or 1), and a double wire indicates that the classical bit m is being used elsewhere.

$$|\psi\rangle \text{ --- } \boxed{X} \text{ --- } \boxed{\text{Measurement}} = m$$

¹This X gate is also called “swap”, or π rotation.

The probability of the two possible measurement outcomes (0 or 1) must sum to 1 [68], and so we have:

$$|\alpha|^2 + |\beta|^2 = 1. \quad (2.5)$$

This means that the Bloch vector representing the state in (2.3) has unit length for pure quantum states, connecting the center of the sphere to any point on its surface. When the state is measured, the wave function collapses into one of the two states, $|0\rangle$ or $|1\rangle$.

Multi-qubit states and multi-qubit operations can be described using the tensor product. The ket $|00\rangle$ can be also written as $|0\rangle \otimes |0\rangle$, as the tensor product of two qubits, to describe such a state. In general, if we have two systems, A and B, with respective state vectors $|\psi\rangle$ and $|\phi\rangle$, then the tensor product of the two systems is denoted $|\psi\rangle \otimes |\phi\rangle$ and is a state vector in the combined space of A and B. For example, if we have two qubits at $|0\rangle$ state, then the tensor product of the two states is a four-dimensional vector

$$|00\rangle = |0\rangle |0\rangle = |0\rangle \otimes |0\rangle = \begin{pmatrix} 1 \\ 0 \end{pmatrix} \otimes \begin{pmatrix} 1 \\ 0 \end{pmatrix} = \begin{bmatrix} 1 \begin{pmatrix} 1 \\ 0 \end{pmatrix} \\ 0 \begin{pmatrix} 1 \\ 0 \end{pmatrix} \end{bmatrix} = \begin{bmatrix} 1 \\ 0 \\ 0 \\ 0 \end{bmatrix}$$

If we were to represent the ket $|00000\rangle$ in a column vector form, it would require $2^5 = 32$ entries. This is why the ket notation is preferred in quantum computing as it provides a concise and convenient representation of multi-qubit states.

It is important to understand the basics of quantum gates and how they operate in order to understand the capabilities and limitations of quantum computers. These gates are a key component of quantum algorithms and are used to perform calculations that are not possible with classical computers.

2.1.3 Describing Quantum States with the Density Matrix

In quantum computation, it is often necessary to consider ensembles of multiple quantum states, each with an associated probability of occurrence. This is where the density matrix representation comes in handy, as it allows us to describe both pure and mixed states using the same mathematical language [18].

The density matrix of a pure state is given by the outer product² of the state vector with itself:

$$\rho \equiv |\psi\rangle \langle\psi|. \quad (2.6)$$

The density matrix allows us to easily represent ensembles of pure states, such as when noise in a communication channel may cause a state to flip with some probability. To represent a pure state, we use the outer product of the state vector with itself, resulting in a matrix of the form [54]:

$$\rho = \begin{pmatrix} |\alpha|^2 & \alpha\beta^* \\ \alpha^*\beta & |\beta|^2 \end{pmatrix}, \quad (2.7)$$

where * denotes the complex conjugate. With these abstractions and conventions about the quantum information layer now clarified, we can move on to the question of how to engineer and manufacture qubits that can be controlled in a precise manner.

2.2 Quantum Physical Layer of a Quantum Computer

Superconducting quantum circuits serve as a widespread means of realizing quantum bits in quantum computers. They are pro-

²An outer product of two matrices \mathbf{u} and \mathbf{v} is calculated as the matrix multiplication $\mathbf{u}\mathbf{v}^\dagger$.

duced by developing nanoscale structures employing superconducting materials on a dielectric substrate, typically silicon. Different types of superconducting qubits exist, including the charge qubit[67], the transmon[53], the flux qubit[69], the phase qubit[61], and the fluxonium[60]. These qubits differ in the number of Josephson Junctions (JJ) and the relative energy scales of their capacitive and inductive elements. The Josephson junction forms the crux of these qubits, consisting of a thin insulator positioned between two superconductors that showcase a macroscopic quantum phenomenon called the Josephson effect. This effect's precise relationship between different physical quantities, like voltage and frequency, has practical applications.

2.2.1 Utilizing Superconducting Materials for Quantum Computing

In quantum computing, superconducting materials play a key role in the creation of qubits. These materials are particularly useful due to the presence of an energy gap in their excitation spectrum, making it easier to maintain the system in its ground state.

These materials exhibit the unique property of zero electrical resistance and the expulsion of magnetic flux fields below of the temperature known as the critical temperature [89]. In contrast to common conductors like copper and silver, which see a gradual decrease in resistance as the temperature drops, the resistance of a superconductor drops to zero at temperatures below its critical temperature (T_c), Fig. 2.2. Examples of superconducting metals and their T_c values include NbTi (10K), Nb (9.2K), Ta (4.4K), Hg (4.2K), and Al (1.19K).

In a superconductor, electrons pair up to form Cooper pairs, which behave as a single macroscopic quantum system. The energy spectrum of this Cooper pair fluid features an energy gap, requiring a minimum amount of energy (Δ_E) to excite the fluid. If Δ_E is greater than the thermal energy of the lattice (the lattice being the structure of atoms within the material), the fluid will remain in its

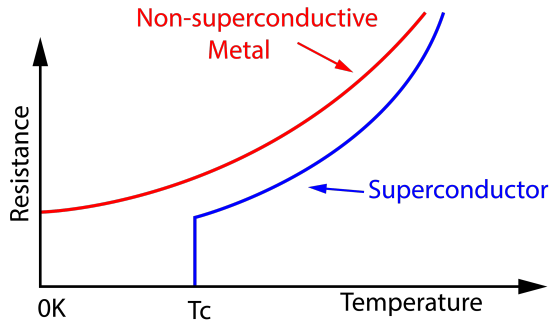


Figure 2.2: Critical temperature of superconductor material compared to non-superconductive metal drop in resistance vs. temperature.

ground state, resulting in zero energy dissipation and the ability to flow without resistance. The steady stream of incoming photons with energy greater than $2\Delta_E$ can break up Cooper pairs into unpaired excitations or quasiparticles, which alter their densities and affect the high frequency response of the superconductor. By applying an oscillating signal with energy far below $2\Delta_E$, the Cooper pairs can be "danced to the tune" (be accelerated and decelerated) by the electromagnetic fields, exhibiting an effective mass twice that of a single electron.

For more information on superconductors and the Bardeen-Cooper-Schrieffer theory, refer to [89].

2.2.2 The Josephson Junction

As previously mentioned, the Josephson Junction is a device composed of two superconductor islands separated by an insulating barrier (which may be only a few atoms thick). At first glance, it might seem that this gap would prevent current from flowing, unless a high enough voltage is applied to create a spark across the gap. However, it is important to note that the voltages and energies involved in the

JJ are significantly smaller, making the spark formation highly unlikely. Nonetheless, due to the behavior of wave functions of quantum systems, there is a small probability that Cooper pairs will tunnel through this barrier. When used appropriately, at close to absolute zero temperatures, this allows us to control supercurrent very precisely, giving us the states that we can use as our state variable in a quantum computer.

Each superconductor Cooper pair fluid can be described by a single wave function. When these two wave functions, $\Psi_1 = \sqrt{p_1}e^{j\varphi_1}$ and $\Psi_2 = \sqrt{p_2}e^{j\varphi_2}$, overlap, they give rise to a phase difference across the junction $\delta \equiv \varphi_1 - \varphi_2$. Here, p_1 and p_2 are the probabilities of finding a Cooper pair at a particular position, and φ_i denotes the superconducting phase at island i . This is the tunneling effect and has been depicted in Fig. 2.3a.

The flow of Cooper pairs constitutes a supercurrent, which is described by the following equations known as the Josephson equations:

$$I_J = I_c \sin(\delta), \quad (2.8)$$

and

$$V = \frac{\phi_0}{2\pi} \frac{d\delta}{dt}, \quad (2.9)$$

where V is the voltage across the superconducting junction, I_c is the critical current parameter across the junction, which is the maximum supercurrent, δ is the phase difference between the wave function of the superconducting state on the left and right superconducting materials, and $\phi_0 = \frac{h}{2e}$ is the flux quantum.

Figure 2.3b depicts the circuit symbol of the Josephson Junction, while Figure 2.3c presents a scanning electron microscope (SEM) image of a produced JJ. The JJ functions as a parallel plate capacitor with capacitance C_J , in addition to its inductive behavior, due to the parallel interface of the two superconducting electrodes.

The JJ acts like a lossless non-linear inductor. In an ideal inductor, the inductance is independent of the current magnitude. However, the JJ inductance, L_J , does depend on the magnitude of the

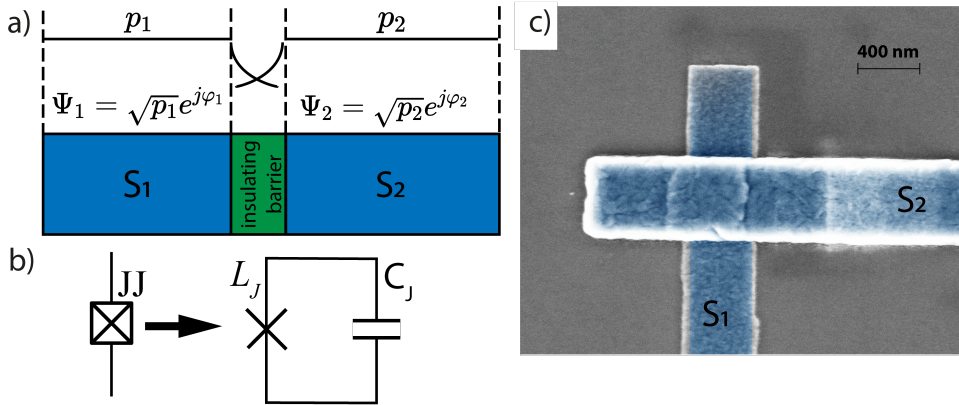


Figure 2.3: (a) Josephson Junction side cut showing the overlapping wavefunctions. (b) Josephson junction symbols for circuitual representation depending if adding the JJ capacitance, C_J , or not. (c) Scanning Electron Microscope (SEM) image of a Josephson Junction top view. Aluminum (false colored blue) on top of silicon (grey).

current [89]:

$$L_J = \frac{\phi_0}{2\pi I_c \cos(\delta)}. \quad (2.10)$$

This non-linear inductance makes a JJ behave as an anharmonic resonator when part of a circuit. This means that when a voltage is applied to the JJ, it emits a photon at the frequency corresponding to the tunneling process that occurs in the junction. This emission happens as a consequence of thermal losses in the superconductor, which is the only way to dissipate the excess energy.

To understand this behavior, it's essential to consider the energy levels of the system. In a harmonic resonator, energy levels are equally spaced, but in an anharmonic resonator like the JJ, the energy levels are not equally spaced. When a voltage is applied, the JJ can absorb or emit energy in discrete quanta, creating photons at specific frequencies corresponding to the energy differences between

these non-equally spaced levels.

This nonlinear relationship between current and voltage, controlled by the inductance L_J , can be utilized in the design of the junction. One of the notable characteristics of Josephson Junctions is their ability to significantly increase current flow in the presence of a magnetic field³. By altering the flux across the junction, the inductance can be adjusted and fine-tuned to the desired frequency for use in a qubit [89]. The JJ serves as a non-linear inductor for the qubit⁴, which can be implemented using a charge, magnetic flux, or plasmon state variable. The charge qubit utilizes the presence or absence of Cooper pairs in an isolated island as the binary states [82], while the flux qubit utilizes the direction of current flow around a loop of superconductor. The transmon qubit combines elements of both charge and flux to reduce noise [53]. Controlling the state variables of qubits is essential for quantum information processing.

2.2.3 The Transmon Qubit

The transmon circuit is made up of a JJ acting as a non-linear inductor, which is connected to a large capacitance C_S . As such, the transmon qubit can be thought of as an LC circuit with a non-linear inductance, as shown in Fig. 2.4a.

In quantum mechanics, several fundamental quantities exist only in discrete quanta, which means that properties are quantized, and energy levels are confined to specific values⁵. This is akin to the resonant modes of a microwave cavity, where only certain frequencies of light can exist within the cavity. Just as the microwave cavity allows only a discrete set of modes or frequencies, the particle in a box also

³When using two JJ as a SQUID loop [48].

⁴The JJ non-linearity is also used for TWPA [65] design, which stands for traveling wave parametric amplifier, a device that can amplify weak microwave signals with low noise and high bandwidth. Inside the TWPA, JJ are used to create a nonlinear transmission line that can achieve parametric gain through three-wave mixing.

⁵Such as angular momentum or spin in atoms.

has a limited number of allowable energy levels. Thus, the particle cannot possess arbitrary energy values, and only discrete energy levels are permitted. This is how energy becomes quantized in quantum mechanics, with the particle in a box serving as a hypothetical example to illustrate the differences between classical and quantum systems.

When studying microwave engineering circuits, it is often assumed that the energy accumulated in an LC resonator can take any positive value. However, if we were to measure the energy of a very high quality factor resonator, Q_L , we would find that the result is quantized into a set of allowed energies known as quantum energy levels. These levels are directly related to the mode frequency of the wave associated with a given particle, through the reduced Planck constant \hbar and the angular frequency ω_0 .

Each step of the ladder of allowed energies for an electron is exactly

$$E = \hbar\omega_0, \quad (2.11)$$

where $\omega_0 = 2\pi f_0$ is the frequency.

Microwave engineers don't often work with conditions where the energy of the electromagnetic quanta, $\hbar\omega$, is close to the scale of the thermal energy of the surroundings,

$$T_a \ll \frac{\hbar\omega_0}{k_B} \quad (2.12)$$

where T_a is the temperature and k_B is the Boltzmann's constant. In normal conditions, such as at room temperature, Johnson noise from the resonator resistance causes the resonator to have a random distribution of energy levels. However, when the temperature is close to 50-500 mK (and the resonator frequency is above 1-10 GHz), quantum effects start to dominate and thus be observable [7]. In a LC resonator under these circumstances, we could move between different energy levels by adding or removing an integer number of microwave photons at the resonant frequency of the circuit.

The energy required to transition from the ground state of the transmon qubit ($|0\rangle$) to the first excited state or first quantum energy level ($|1\rangle$) is denoted as $E_{01} = \hbar\omega_{01}$, Fig. 2.4b⁶. The frequency ω_{01} is commonly referred to as ω_q , as it is the frequency required to excite the qubit from its ground state. The transition energy from the first state to the second state of the qubit, denoted as E_{12} , is approximately determined by the charging energy E_C . We define the difference between these energies as the transmon anharmonicity, represented as $\alpha \equiv E_{12} - E_{01} \approx -E_C$. In quantum computing, the first two energy levels of the ladder, denoted as $|0\rangle$ and $|1\rangle$, are used for qubits. This is made possible by the anharmonicity α , which causes the third level of the ladder to have a higher energy and therefore higher frequency than the qubit frequency, ω_q , so the $0 \rightarrow 1$ hamiltonian can be uniquely addressed.

The frequency of the qubit can be engineered using the following equation [53, 92]⁷:

$$\omega_q = \frac{\sqrt{8E_C E_J} - E_C}{\hbar}. \quad (2.13)$$

Leaving then two degrees of freedom for designing the qubit frequency, E_J and E_C , which basically depend on the area of the JJ and the size of the capacitor C_S respectively. The charging energy of a

⁶The transmon qubit is designed for stable energy levels with respect to excess Cooper pairs (N_g). By adjusting an external gate voltage, the number of Cooper pairs on the island can be optimized, leading to improved coherence and reduced sensitivity to charge noise. This flatness in energy levels is achieved through a large shunting capacitance at the Josephson junction. This capacitance decreases the sensitivity of the qubit's energy levels to changes in N_g , enhancing performance and robustness.

⁷This equation comes from solving the effective Hamiltonian of the transmon [92], $H_{transmon} = 4E_C \left(\hat{N} - N_g \right)^2 - E_J \cos(\hat{\varphi})$, obtaining the eigenenergies [92], $E_m = -E_J + \sqrt{8E_C E_J} \left(m + \frac{1}{2} \right) - \frac{E_C}{12} (6m^2 + 6m + 3)$, then assuming $\frac{E_J}{E_C} \sim 50$ we can find the frequency of the qubit through [92] $\hbar\omega_q = E_{01} = E_1 - E_0 \approx \sqrt{8E_C E_J} - E_C$.

transmon, E_C , is typically given by

$$E_C = \frac{e^2}{2C_\Sigma}, \quad (2.14)$$

where e is the electron charge constant, and the total capacitance C_Σ is [92]

$$C_\Sigma = C_S + C_J + C_{gnd}, \quad (2.15)$$

with C_S being the capacitance of the planar capacitor containing the JJ as shown in Fig. 2.4c, C_J representing the junction capacitance as depicted in Fig. 2.3b and C_{gnd} the capacitance to ground. Since C_J and C_{gnd} are usually small in comparison to C_S , they can be neglected [64] and then $C_\Sigma \approx C_S$. Thus, the anharmonicity, α , can be primarily engineered through C_S .

The qubit capacitor pads, C_S , provide the charging (“capacitive”) energy E_C and the JJ provides the Josephson (“inductive”) energy

$$E_J = \frac{I_c \phi}{2\pi} \quad (2.16)$$

. The Hamiltonian, an operator corresponding to the total energy of a system in quantum mechanics, is given by [53]:

$$\hat{H} = 4E_C n^2 - E_J \cos(\hat{\phi}). \quad (2.17)$$

The difference in the number of Cooper pairs, denoted as n . Cooper pairs can tunnel across the junction. This tunneling phenomenon gives rise to fluctuations in the number of Cooper pairs n effectively influencing the junction’s behavior.

For transmon qubits, it is typical to have $\frac{E_J}{E_C} \approx 50$ and $-\alpha \approx E_C \approx \hbar \cdot 2\pi(160-400)$ MHz⁸, resulting in $E_J \approx \hbar \cdot 2\pi(10-25)$ GHz⁹. The inductive energy E_J can be engineered by adjusting the area of the JJ, and it also determines the critical current, I_c .

⁸Thus, from (2.14), C_S in the order of 65fF.

⁹Thus, from (2.16), I_c in the order of 3pA.

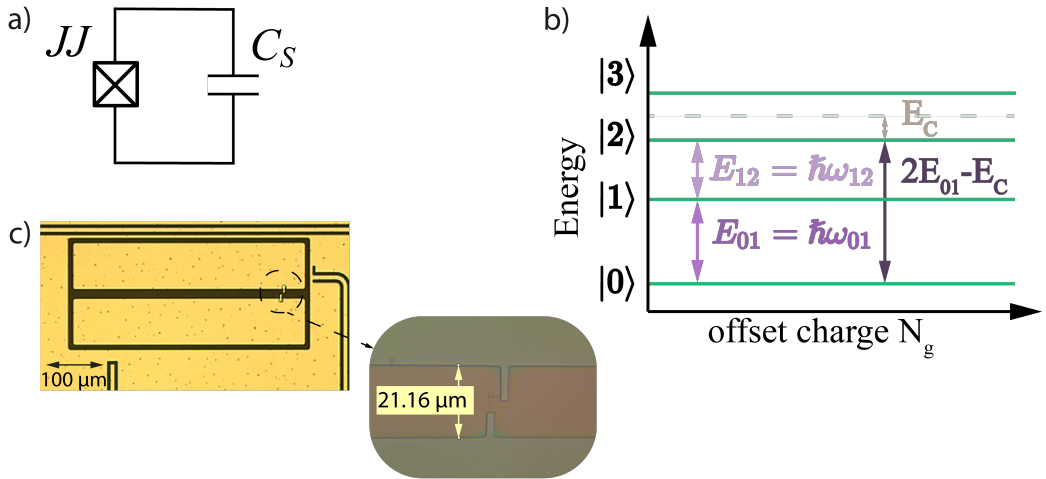


Figure 2.4: (a) LC-circuit representation of a transmon qubit with shunting capacitance C_S . (b) Energy level scheme of transmon qubit with a flat dispersion relation. (c) Microscope picture of a transmon qubit. The two rectangular “paddles” serve as the shunt capacitance C_S . The JJ is positioned on the bridge between the two capacitances forming a cross as seen in the zoom.

2.3 Noise and Decoherence in Quantum Computing

Random, uncontrollable physical processes in the equipment used to control and measure qubits or in the local environment surrounding the quantum processor can cause noise, leading to decoherence and reducing the operational fidelity of the qubits.

In a closed system, the evolution of a qubit state is deterministic, meaning that if we know the initial state of the qubit and its Hamiltonian, we can predict the state of the qubit at any future time. However, in open systems, the qubit interacts with uncontrolled degrees of freedom in its environment, which we refer to as noise or

fluctuations. In the presence of noise, the qubit state becomes less and less like the predicted state over time, and eventually the state is lost. There are many different sources of noise that affect quantum systems, which can be divided into two main categories: systematic noise and stochastic noise [54].

Systematic noise arises from systematic control errors. For example, if we apply a microwave pulse to the qubit that is intended to impart a 180-degree rotation, but the control field is not tuned correctly, the pulse may slightly over-rotate or under-rotate the qubit by a fixed amount. The error is systematic, so it will lead to the same rotation error each time it is applied. However, once systematic errors are identified, they can often be corrected through proper calibration.

Stochastic noise arises from random fluctuations of parameters that are coupled to the qubit [6]. Examples include thermal noise in the control lines leading to the qubit, which can cause voltage and current fluctuations, and fluctuations in the amplitude or phase of the oscillator that provides the carrier for a qubit control pulse. Additionally, randomly fluctuating electric and magnetic fields in the local environment of the qubit, such as on metal surfaces or inside the substrate, can couple to the qubit and cause uncontrolled fluctuations in one or more qubit parameters, leading to decoherence [54, 6].

The degree to which a qubit is affected by noise depends on the amount of noise present and the qubit's susceptibility to that noise. The former is often a matter of materials science and fabrication. It may also depend on the quality of the control electronics and cryogenic engineering, which can limit the levels of noise on the control lines that connect to the qubits. The latter – qubit susceptibility – is a question of qubit design. Qubits can be designed to trade off sensitivity to one type of noise for increased sensitivity to other types of noise. Therefore, materials science, fabrication engineering, electronics design, cryogenic engineering, and qubit design all play a role in creating devices with high coherence [54].

Decoherence processes are characterized by two rates:

Longitudinal relaxation rate (along the z -axis, from north pole of the Bloch sphere, $|0\rangle$ to the south pole $|1\rangle$), which is the inverse time it takes for a qubit to relax to its lowest energy state (usually $|0\rangle$) and is denoted as [54]:

$$\Gamma_1 \equiv \frac{1}{T_1} \quad (2.18)$$

Transverse relaxation rate (along either the x or y axes of the Bloch sphere), which is the inverse time constant by which the relative phase of a superposition state becomes random and is denoted as [54]:

$$\Gamma_2 \equiv \frac{1}{T_2} = \frac{\Gamma_1}{2} + \Gamma_\varphi \quad (2.19)$$

The transverse relaxation rate also includes the pure dephasing rate Γ_φ .

In reality, the quantum state of a qubit is not a pure state (located on the surface of the Bloch sphere with a Bloch vector of amplitude 1), but rather a mixed state with a Bloch vector that terminates at points within the unit sphere. This mixed state has a longitudinal decay function term $e^{-\Gamma_1 t}$ and a transverse decay function term $e^{-\Gamma_2 t}$, both time-dependent.

The density matrix of a pure quantum state looks like (2.7), while the mixed state density matrix, which takes into account the impact of noise on the qubit with the same initial state ($t=0$), would be [54]:

$$\rho = \begin{pmatrix} 1 + (|\alpha|^2 - 1) e^{-\Gamma_1 t} & \alpha\beta^* e^{i\delta\omega t} e^{-\Gamma_2 t} \\ \alpha^*\beta e^{-i\delta\omega t} e^{-\Gamma_2 t} & |\beta|^2 e^{-\Gamma_1 t} \end{pmatrix}. \quad (2.20)$$

Here, $\delta\omega = \omega_q - \omega_d$, represents the difference between the qubit frequency, ω_q , and the rotating-frame frequency, ω_d ¹⁰ [54].

¹⁰For a driven system with a drive at ω_d .

The density matrix (2.20) is constructed such that for $t \gg T_1, T_2$, the upper-left matrix element will approach unit value, indicating that all population relaxes to the ground state, while the other three matrix elements decay to zero, $\rho = \begin{pmatrix} 1 & 0 \\ 0 & 0 \end{pmatrix}$, indicating the $|0\rangle$ state. This is related to the assumption that the environmental temperature is low enough that thermal excitations of the qubit from the ground to excited state rarely occur.

2.3.1 Understanding Qubit Decay time T_1

The decay time, T_1 , is a measure of how long it takes for a qubit to relax to its steady state value, which is typically the ground state due to Boltzmann statistics and typical operating conditions. The longitudinal relaxation rate, Γ_1 , describes depolarization along the qubit's quantization axis (z-axis), also known as "energy decay" or "energy relaxation." This occurs due to energy exchange with the environment, and involves both an "up transition rate", $\Gamma_{1\uparrow}$, which represents excitation from $|0\rangle$ to $|1\rangle$, and a "down transition rate," $\Gamma_{1\downarrow}$, which represents relaxation from $|1\rangle$ to $|0\rangle$. The T_1 decay time is represented in the exponential decay function of the mixed state density matrix (2.20), and is affected by the temperature, with a lower temperature leading to a longer decay time. In the case of superconducting qubits, which are typically designed at a frequency of $\omega_q/2\pi \approx 5$ GHz and operated at temperatures of $T \approx 20$ mK, the up transition rate is exponentially suppressed by the Boltzmann factor, meaning that only the down transition rate significantly contributes to relaxing the population to the ground state. This means that qubits generally lose energy to their environment, but the environment rarely introduces qubit excitations [54]. In simpler terms, while a classical bit state is time-independent, the state of a qubit will only remain for a certain time, T_1 , before it decays to the ground state, as illustrated in Fig. 2.5.

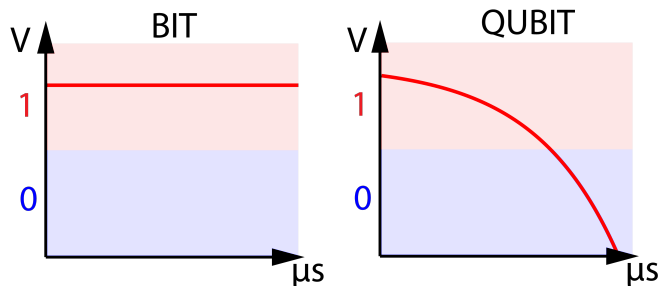


Figure 2.5: Bit vs. Qubit state over time. Bit state is maintained over time while the Qubit state decays exponentially over time and is only maintained for a decay time T_1 that for transmon qubits is usually around the tens of μs .

2.4 Microwave Resonators for Quantum Bits: Dispersive Readout Technique

Microwave resonators play a crucial role in the measurement of qubits, which are the building blocks of quantum computers. In order to accurately measure qubits, the measurement apparatus must not extract information from the qubits or cause any parasitic losses during the implementation of logic gates. To achieve this, we need to design a passive network whose admittance, $Y(\omega)$, allows for the robust distinction between the two states of a qubit, $|0\rangle$ and $|1\rangle$, while preserving the internal Q -factor of the qubit at ω_q .

One approach to read the state of the qubit could hypothetically be to connect the qubit to a transmission line through a capacitor and use a microwave probe pulse to scatter off the qubit [7]. The admittance difference between the two quantum states could then be detected as a shift in the resonance peak of the transmitted signal. However, this hypothetical method has a fundamental limitation: the time it takes for the probe pulse to interact with the qubit and acquire an amplitude and phase shift is equal to the qubit's own decay time, known as the ring-down time, [7]

$$T_{1_{non-dispersive}} \approx \kappa^{-1}. \quad (2.21)$$

This means that the measurement time and the qubit's lifetime must be necessarily equal to have enough SNR, which limits the accuracy of the readout.

In other words, the measurement ring-up time, κ , is also the ring-down time of the qubit itself [7]

$$T_{1_{non-dispersive}}^{-1} \approx \gamma_q = \frac{\omega_q}{Q_m}, \quad (2.22)$$

where Q_m is the loaded quality factor of the qubit.

To solve this issue and allow for fast, accurate measurement while preserving the coherence of the qubit, a common approach is to use a linear readout resonator, as shown in Fig. 2.6a. This readout resonator is coupled to the readout line through a capacitor, C_k , and to the qubit through C_g . This method, known as dispersive readout, allows the probe signal to acquire a state-dependent phase shift while isolating the qubit from external damping. The readout resonator and qubit are typically separated in frequency by a detuning

$$\Delta \equiv \omega_r - \omega_q. \quad (2.23)$$

This detuning is usually around 500 MHz to 1.5 GHz for transmon qubits. At the qubit frequency, the resonator acts as a short to ground, blocking radiation from the qubit and preserving its coherence. As the qubit has different impedance in its two states, the loading it imparts on the resonator is state-dependent, allowing for the detection of the qubit's state through measurement of the resonator frequency.

The use of a resonator between the qubit and the measuring device, known as dispersive readout, allows for an improved ring-up time, or bandwidth, of the resonator. This bandwidth, denoted as κ , is determined by the resonator's resonance frequency, f_r , and its loaded quality factor, Q_L

$$\kappa = \frac{f_r}{Q_L}. \quad (2.24)$$

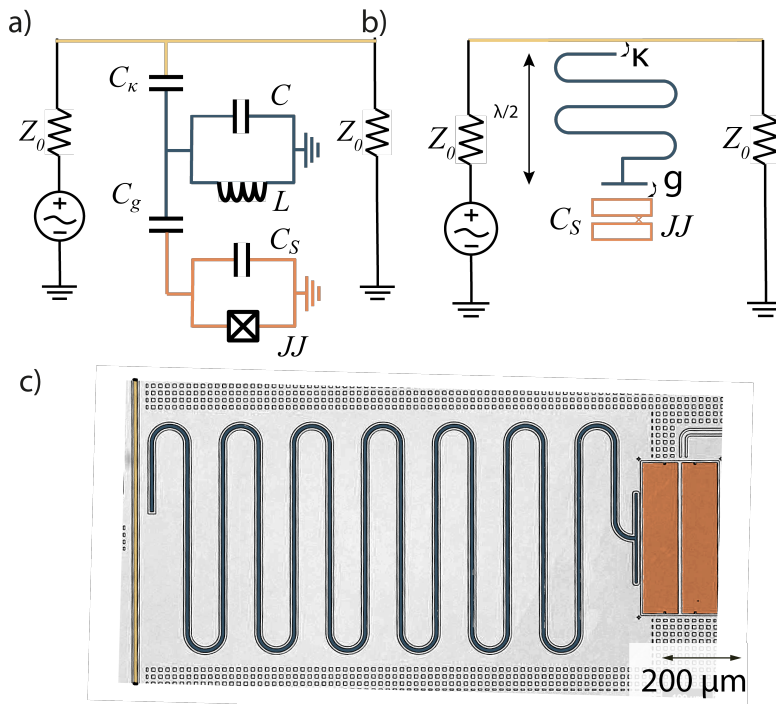


Figure 2.6: (a) Circuit representation of the regular dispersive read-out case of qubit (orange) coupled to a resonator (blue) through C_g capacitance and the resonator coupled to the feedline (yellow transmission line) through C_κ . This way, the resonator (~ 1 GHz detuned from the qubit) acting as a short at the qubit frequency, protects the qubit from the 50Ω environment, Z_0 . The qubit state is read in a transmission measurement through the feedline. (b) Cartoon of the implementation of the circuit in (a) with a planar plate capacitor to implement C_S (JJ represented with an x) and a $\lambda/2$ transmission line resonator. (c) False colored microscope picture of the manufactured circuit shown in (b) with the same corresponding colors for each element.

The ring-up time, or coupling strength to the feedline, also sets the characteristic time scale for energy to leak into or out of the resonator. In the dispersive regime, where the qubit frequency is significantly detuned from the readout resonator, the decay time of the qubit, T_1 , can be greatly improved compared to the non-dispersive case (2.21). This is because the readout resonator effectively shorts the resistive load presented by the readout line, allowing T_1 to remain much larger in the dispersive case [23]

$$T_1 \approx \kappa^{-1} \left(\frac{\Delta}{g} \right)^2. \quad (2.25)$$

Where g is the strength of the coupling between resonator and qubit, and can be tuned with C_g . It is worth noting that the higher the quality factor, Q_L , of the resonator, the higher T_1 can be achieved (2.25) and (2.24), but the readout will be slower.

The readout resonator can now be coupled relatively strongly to the measurement line through C_κ for fast ring-up and measurement times. In the dispersive regime the qubit frequency is detuned from the readout resonator by many linewidths [70, 10],

$$\Delta \gg \kappa, g. \quad (2.26)$$

2.4.1 Measuring Quantum Information in the Strong Coupling Regime

Dispersive readout involves the interaction between a qubit and a readout resonator, resulting in a frequency shift of the resonator known as the dispersive shift, 2χ . For the transmon qubit, this shift depends on the strength of the coupling between the qubit and resonator, g , the detuning, Δ , between the qubit and resonator frequencies, and the frequency of the resonator, ω_r ,

$$\chi = \frac{g^2}{\Delta} \left(\frac{\alpha}{\Delta + \alpha} \right) \left(\frac{\omega_r}{\omega_q} \right). \quad (2.27)$$

The shift results in a different frequency for the resonator in the two states of the qubit, $|0\rangle$ and $|1\rangle$, allowing for the detection of the qubit's state through the resonator's frequency [92]

$$\tilde{\omega}_r = \omega_r + \chi \langle \hat{\sigma}_z \rangle, \quad (2.28)$$

where ω_r is known as the bare resonator frequency and is the one that we would measure classically without any effects of the qubit, $\tilde{\omega}_r$ is known as the dressed resonator frequency and $\hat{\sigma}_z$ is the Pauli z spin operator ¹¹ and describes the z energy states of the qubit.

This resonator dressing will happen in the strong coupling regime, where g is significantly larger than the resonator's bandwidth and qubit relaxation time [82]

$$g \gg \kappa, T_1^{-1}. \quad (2.29)$$

In the strong coupling regime the energy can be exchanged coherently between the resonator and qubit before being lost to the environment. However, an upper limit on g is that it must be small compared to the eigenfrequencies of the qubit and resonator, ω_q and ω_r , respectively [92] to preserve the dynamics of qubit-resonator as two independent entities.

In the dispersive readout circuit, Fig. 2.6a, the ring-up rate, κ , and the qubit lifetime, T_1 , are constrained by [23]

$$\kappa T_1 \lesssim \frac{\Delta}{\chi}. \quad (2.30)$$

This formula highlights an inherent trade-off between the fast response time of the resonator κ and the long coherence time of the qubit T_1 . When considering a specific detuning Δ between the resonator and qubit, as well as the coupling strength g between them, optimizing for a faster κ to expedite measurements comes at the cost of reducing the coherence time T_1 of the qubit.

¹¹ $\sigma_z = \begin{pmatrix} 1 & 0 \\ 0 & -1 \end{pmatrix}$.

The measurement outcome relies on the contrast in transmission magnitude between the two qubit states, as illustrated in Fig. 2.7. If $\kappa \gg 2\chi$, photons exit the resonator rapidly, but they carry minimal information. When $\kappa \ll 2\chi$, each photon contains a full bit of information, yet due to the small κ , they do not exit the resonator fast enough to acquire that information within a time T_1 .

To strike a balance, it becomes essential to increase κ to obtain faster photons, until the optimum point is reached at $\kappa = 2\chi$. At this point, the two state resonances are significantly separated while having enough κ as to extract fast information. This choice significantly enhances the contrast in transmission magnitude, ensuring proper separation of the resonances, preventing overlap, and facilitating easy distinction between states [81].

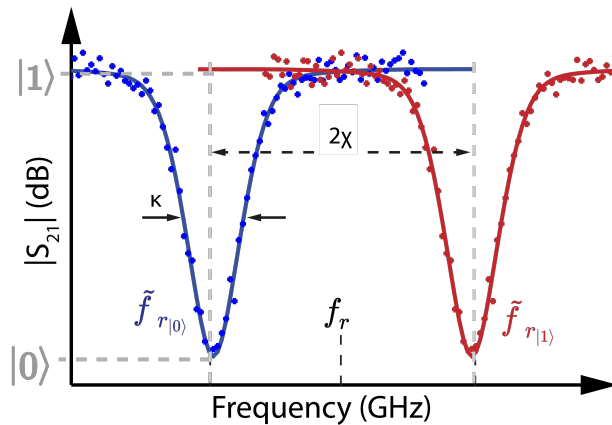


Figure 2.7: Concept measurement in transmission of the device at (2.6). The qubit states cause the resonator frequency to shift, leading to large measurable shift. κ is the bandwidth of the resonator and when measuring $|S_{21}|$ at frequency $\tilde{f}_{r(0)}$, full transmission is observed when the qubit is at state $|1\rangle$ and low transmission is observed when the qubit is at state $|0\rangle$.

To improve the signal to noise ratio (SNR) of the measurement,

the readout resonator could be driven with higher power. However, the average number of microwave photons \bar{n} “stored” in the resonator, \bar{n}_r , affects the qubit frequency as well. This frequency pull on the qubit frequency due to the field intensity in the resonator, number of photons, is known as the ac-Stark shift [81]

$$\Delta_{ac-stark} = 2\chi\bar{n}_r. \quad (2.31)$$

When the ac-Stark shift, $\Delta_{ac-stark}$, becomes comparable to the qubit’s anharmonicity, α , we start breaking down the distinct energy-level structure that defines the qubit, and the qubit becomes harder to control in the dispersive readout regime that we work. For typical transmon parameters, this can already happen when the resonator stores just $\bar{n} \sim 25$ photons. The critical photon number, above which the resonator and qubit start exchanging energy and lose the “projective” character, is given by [54]

$$n_c = \frac{\Delta^2}{4g^2}. \quad (2.32)$$

To ensure accurate measurement results, it is important to carefully balance the readout resonator drive power and detuning. Too much drive power can cause the ac-Stark shift to become significant relative to the qubit’s nonlinearity, leading to measurement errors. To avoid this issue, the readout resonator drive power is typically kept at a level where the resonator is only populated with a few photons ($\bar{n} \lesssim 10$). On the other hand, decreasing the resonator’s photon rate (by decreasing the parameter κ in design) can improve the qubit relaxation time (higher T_1), but can also lead to poor SNR.

Furthermore, detuning the readout resonator from the qubit frequency can reduce the ac-Stark shift and improve the signal-to-noise ratio. However, a larger detuning Δ results in a smaller dispersive shift 2χ (2.27), Fig. 2.7, and lower contrast in transmission magnitude between the qubit states, so finding the optimal balance between these competing factors is crucial for optimal measurement performance.

2.5 Enhancing Superconducting Qubit Measurements with the Purcell Filter

The dispersive measurement strategy has a notable limitation: while the resonator effectively reduces the qubit's sensitivity to the dissipation of the external circuitry, it does so only to a certain extent. Even when operating far off resonance, the resonator's finite quality factor prevents complete isolation of the qubit. As a consequence, the qubit "sees" the tail of the resonator's Lorentzian profile, resulting in some degree of damping. This effect can be quantified by a relation involving four parameters described by (2.25). As the resonator becomes more connected to the external environment, the qubit state can be read out more quickly with a higher signal-to-noise ratio (SNR) due to enhanced emission increasing κ and g . A higher κ enhances the flux of photons probing the readout resonator, while a higher g increases χ and the separation between the resonator's dressed frequencies. However, the qubit also becomes more susceptible to relaxation events and has a shorter relaxation or decay time T_1 due to the increased connection to the outer world. This increased probability of a qubit excitation decaying due to the presence of the readout resonator is called the Purcell effect [34].

The Purcell relaxation time T_1^{Purcell} places an upper limit on the total relaxation time T_1 of a qubit since

$$\frac{1}{T_1} = \frac{1}{T_1^{\text{Purcell}}} + \frac{1}{T_1^{\text{dielectric}}} + \frac{1}{T_1^{\text{metal-dielectric}}} \dots \text{ (other losses in the circuit).} \quad (2.33)$$

If the qubit's decay rate $\frac{1}{T_1}$ is close to the Purcell decay rate $\frac{1}{T_1^{\text{Purcell}}}$, the qubit is said to be Purcell limited [4].

The architecture of Fig. 2.6a was the standard for transmon qubits between 2005 and 2010. However, as superconducting qubit coherence times improved and gate error rates decreased, the readout accuracy needed to keep up. To reduce the number of errors caused by the Purcell effect and enable the readout of multiple qubits through

frequency domain multiplexing, it is now common to further shape the admittance function of the qubit's readout circuit. This can be done by adding additional transmission zeros at the qubit frequency, incorporating secondary readout resonators, or including a bandpass filter near the readout resonator frequency with strong rejection at the qubit frequency, as shown in Fig. 2.8. These type of filters are known as Purcell Filters (PF) in the superconducting qubit literature.

The Purcell filter mitigates Purcell decay by modifying the impedance seen by the qubit through the readout resonator, thereby protecting the qubit from relaxation into its environment [76, 49] while keeping high SNR. The bare Purcell limit in (2.25), which predicts decay without the effect of any filter, is multiplied by a factor when the Purcell filter is added between the readout resonator and the 50 Ω environment, Fig. 2.8a. This can lead to an increase in $T_{1_{Purcell}}$ by several orders of magnitude. The expression for $T_{1_{Purcell}}$ becomes [76]

$$T_{1_{Purcell}} = \underbrace{\kappa^{-1} \left(\frac{\Delta}{g} \right)^2}_{\text{Bare Purcell limit}} \underbrace{\left(\frac{\omega_r}{\omega_q} \right) \left(\frac{2Q_F \Delta}{\omega_r} \right)^2}_{\text{Purcell filter}}. \quad (2.34)$$

The expression for T_1 is the same as in (2.25) with an additional multiplying term due to the isolation provided by the Purcell filter, where Q_F is the quality factor of the Purcell filter. There is also a tradeoff with Q_F , as a lower value allows for a higher bandwidth and the ability to place more qubit readout resonators inside the bandpass in a multiplexed readout scheme, but it also leads to a lower T_1 .

Depending on the design of the readout for the quantum processor to which the filter should be coupled to, there are various ways to design a Purcell filter, including; quarter-wave stubs [76], low-Q bandpass filters [49, 52], and stepped-impedance filters [11]. The optimal choice depends on system properties such as qubit-resonator detunings, required bandwidth, and allowed insertion loss [54].

Purcell filter implementations found in literature are:

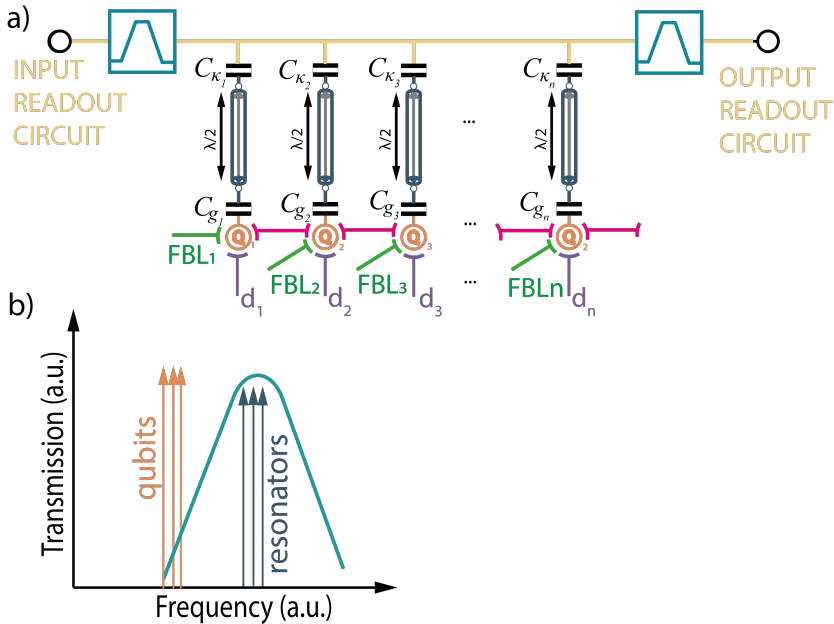


Figure 2.8: (a) Dispersive readout circuit with several qubits with resonators coupled to the same feedline. This circuit also shows the concept of qubit drive line (purple), flux bias line (light green) and resonator bus (pink). These lines are used to control de qubit at qubit's frequency f_q , tune the qubit by using current to induce a magnetic field and communicate qubits between them respectively. A Purcell-filter (greenish) is added to the circuit, providing protection for the qubit, while allowing the resonator field to decay fast to the environment. (b) Transmission spectrum of a Purcell filter (greenish), centered around the frequencies of the resonators (blue arrows), whereas the frequencies of the qubits (orange arrows) are far detuned. The measurement resonators, which produce dips in the transmission spectrum, are all placed within the filter pass band. The qubits sit out of the pass band and are protected from emission. Each resonator's amplitude and phase contains the information of only one qubit.

1. Notch Purcell filter To protect the qubit from emitting energy, a notch filter is implemented in this system by creating a $\lambda/4$ transmission line inverter loaded with an open circuit connected in parallel to the feedline (the transmission line where the readout resonators are capacitively coupled to) [23, 16]. However, this system is not scalable as it requires a separate filter for each qubit¹². Additionally, the narrow protected band of the filter prevents the use of high-fidelity logic gates based on dynamic tuning of the qubit frequency, as changing a qubit's frequency would bring it out of the protected notch which would decrease coherence time [23]. Moreover qubit frequencies may change due to manufacturing uncertainties while readout resonators remain fixed. State-of-the-art quantum processor chips have resonators with uncertainties around 30 MHz due to manufacturing uncertainties, while qubit frequency uncertainties are typically around 150 MHz although improving down to 5 MHz in advanced cleanrooms [23, 43].

2. Dedicated Purcell filters Connecting each readout resonator to its own PF can improve the accuracy of measurements by creating a sharper transition from bandpass to stopband. A capacitor is often placed at the input port of the feedline to improve the efficiency of qubit state measurement [42]. The small detunings between resonators can lead to overlap in the filter functions between the readout resonators, making it difficult to accurately read out the qubits without partially measuring their neighbors (i.e. cross-dephasing) [12, 42]. This can cause additional dephasing of untargeted qubits.

3. Bandpass Purcell filter The bandpass Purcell filter allows for strong reduction of the Purcell rate for qubits outside the filter bandpass, enabling quantum gates based on qubit frequency tuning

¹²Each TL resonator at typical frequencies (~ 7 GHz) takes approximately 0.5 to 1 mm^2 area on the chip. This would mean that for a QPU of hundreds of qubits, hundreds of extra mm^2 would be needed.

and multiplexed readout of multiple qubits using readout resonators with different frequencies within the filter bandwidth [84].

3.1. Feedline modifications as Bandpass Purcell filter

The bandpass Purcell filter can be implemented by transforming the feedline into a lossy resonator at the readout resonator frequency. This can be done by using a feedline of length $\lambda/2$ at a frequency near the readout frequency, loaded in both ends with a short circuit [12] or by directly coupling the $\lambda/2$ feedline to the ends with a capacitor [59]. Another approach is to use a standing wave mode as a filter resonance by interrupting the feedline at $\lambda/4$ length with a capacitor on one side and shorting it to ground on the other side [23]. These implementations allow for the multiplexed readout of several qubits with reduced Purcell rate.

3.2. Out-of-chip filters as Bandpass Purcell filter In some cases, multipole implementations of Purcell filters may provide higher and flatter bandwidths, higher rejection in the stopband, or more steeped transitions from bandpass to stopband (higher rolloff rate), allowing for the placement of qubits closer to resonators. Such filters utilize poles and zeros to affect the slope of the system's magnitude response. The order of a filter, or the minimum number of reactive components it requires, determines the rate at which the filter's response falls in the transition band. Higher-order filters have faster rolloff rates.

One example of a fifth-order stepped impedance dual-band filter used as a Purcell filter is found in [11], both on-chip and off-chip of a single-qubit chip. This filter has a wide stopband from 2-6 GHz, a passband around 6.5 GHz, and a DC passband, allowing for fast flux biasing with a single filter and single line for both measurement and control lines. However, stepped impedance Purcell filters (SIPFs) are too large to be integrated on-chip with multiple qubits while avoiding chip spurious modes.

An alternative solution using ultra-compact, high-order microwave acoustic filters as Purcell filters is proposed in [17].

Purcell filters are used to protect qubits from external noise, allowing for longer coherence times and more accurate quantum computations. In this short literature review, we compare four types of Purcell filters: notch filters [16], dedicated Purcell filters [42] and feedline modifications [59, 23] and plot the Purcell Factor,

$$\text{Purcell Factor} = \frac{\text{Measured } T_1}{\text{Bare Purcell limit}}, \quad (2.35)$$

where the bare Purcell has been defined in (2.25), versus the extra area needed in the chip to implement the filter in the analysis grid of Fig. 2.9. The Purcell Factor is defined as the improvement of T_1 due to the Purcell filter. By analyzing their strengths and limitations, we aim to help researchers decide which Purcell filter is best suited for their specific quantum computing needs. We find that, while all types have their own benefits, the acoustic filters show promising potential due to their high order and compact size, since [17] show size of 1 mm^2 and calculated improvements of two orders of magnitude in $T_{1_{\text{Purcell}}}$. However, further research is needed to fully understand the capabilities of acoustic wave filters used as Purcell filters. Some calculations and measurements to study the possibility of using acoustic wave filters as Purcell filters are shown in *Chapter 5*.

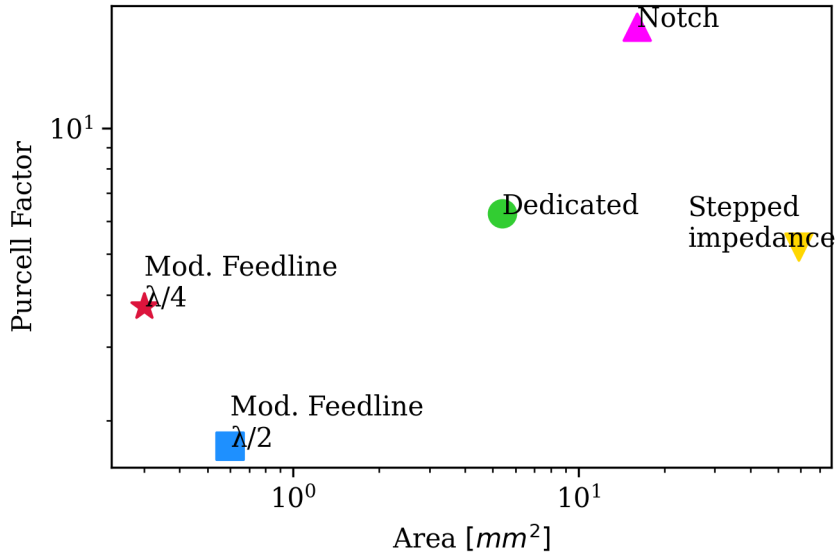


Figure 2.9: Purcell filter competitive matrix comparing Purcell Factor vs extra area needed on chip to implement the filter. Mod. Feedline $\lambda/4$ [49], Mod. Feedline $\lambda/2$ [59], Dedicated [42], Stepped impedance [11] and Notch [16].

Chapter 3

Effective Control and Measurement Strategies for Superconducting Qubits in Quantum Computing

This chapter presents a comprehensive overview of the proposed architecture for the control electronics system and signal processing using IQ modulation, focusing on precise quantum state control and measurement. We explore the utilization of IQ mixers to achieve accurate control and discuss the role of digital signal processing in uncovering qubit states. Additionally, we introduce “Qilimanjaro’s Quantum Operating System”, the full-stack software framework developed for benchmarking QPU performance in quantum computers and executing quantum algorithms. Furthermore, we delve into enhancing quantum computing performance through advanced microwave packaging techniques, including the design and validation of a 12-port PCB housing optimized for quantum computing applications. These strategies and methodologies contribute to advancing the field of quantum computing and provide valuable insights into quantum information processing.

3.1 Effective Control and Measurement Strategies for Qubits in Quantum Computing

To control and measure qubits, we use a combination of electronic components at room temperature and microwave pulse sequences. The control signals, which typically operate between 4 to 10 GHz. The frequency of the qubit, ω_q , which for transmon qubits is usually around 4-6 GHz, are used to manipulate the quantum state of the qubit. The state of the qubit is then inferred through measurement of the readout resonator, which is performed by digitizing the down-converted signal coming from the readout resonator at its resonance frequency of typically 6-8 GHz.

The main control electronics components and their connections are shown in Fig. 3.1 for a single qubit QPU 3D transmon. For the 3D transmon, only one input and one output lines are needed, as the control and readout signals are combined in the same line. However, for more complex quantum processing units (QPUs), additional lines are required for control and readout. An example of a five-qubit chip may require one input and one output lines for readout, five independent qubit control lines, and potentially four lines for coupler control (DC to 1 GHz) (depending on the chosen topology interconnecting the qubits) and five lines for flux bias control (DC) to tune the qubit's frequency.

Waveforms are generated using an arbitrary waveform generator (AWG) with I and Q outputs and are modulated using an IQ mixer and a local oscillator (LO). They are then combined using a high-frequency combiner. In the case of a chip circuit like the one shown in Fig. 2.8a, the combiner at the input port (P1) is not used and instead separate drive lines (orange) with separate AWG for each qubit are used. The readout part (light and dark blue) would remain the same since all qubits' readout resonators are coupled to a shared feedline.

To control these instruments and manage the various operations, we have developed an open-source middleware platform in Python. Our software converts the specified circuit into microwave pulse sequences, operates multiple remote field-programmable gate array (FPGA) boards and instruments, performs system calibration periodically, schedules all operations, reconstructs measurements, and stores results. Our software for qubit characterization and calibration, called Qililab, allows for seamless control of the instruments, mainly arbitrary waveform generators and digitizers, from the perspective of the user.

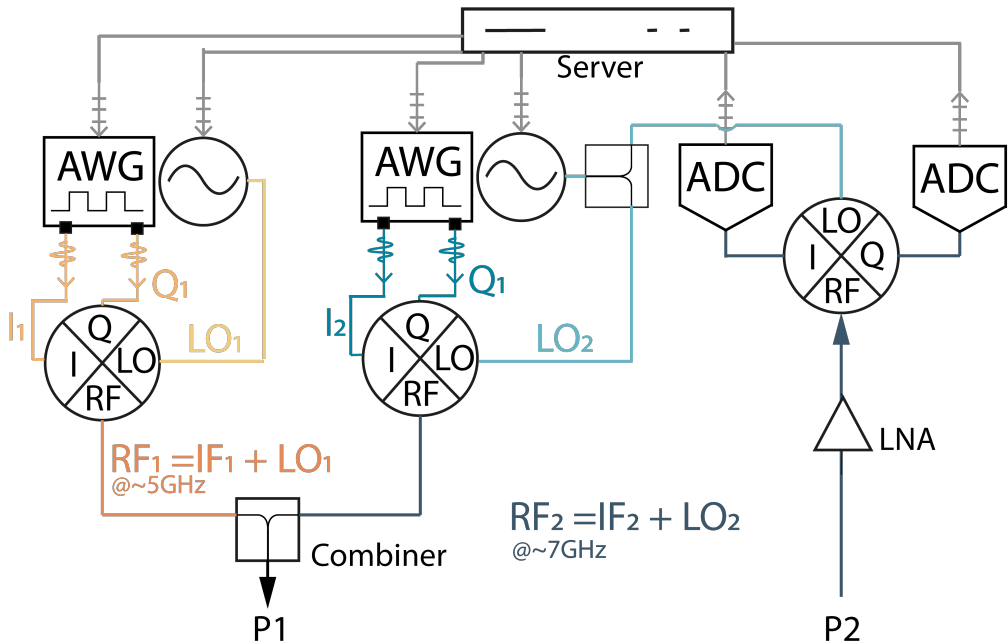


Figure 3.1: Diagram of the components of the control electronics system in the rack. This is the simplest possible scenario for a 3D transmon with combined readout and drive input. The readout signal coming from the qubit is demodulated and I and Q signals are digitally processed.

In order to control the quantum state of a qubit through the use of quantum gates, we must apply an external electromagnetic field at a specific frequency (f_q) to the qubit. This is typically performed through a drive line. When viewed on the Bloch sphere, the application of a pulse at f_q appears as a rotation axis at a constant speed on the x-y plane. The first pulse sets rotation axis, all other pulses are relative to that. The direction of this rotation can be controlled by altering the phase (θ) of the applied field. A sine wave will induce a rotation around the x-axis, while a cosine wave (with a 90 degree phase offset) will cause a rotation around the y-axis. The speed of the rotation is proportional to the amplitude (E_0) of the electric field, which is expressed as

$$E(t) = E_0 \sin(2\pi f_q t + \theta). \quad (3.1)$$

To apply a specific quantum gate, we must send a pulse with the correct amplitude, phase, frequency and length. The rotation angle is determined by the product of the length and amplitude, or the area under the pulse envelope. If we wish to rotate around an axis that does not lie in the x-y plane, we must decompose it into a combination of x and y rotations. It is also worth noting that the time evolution of a quantum mechanical system is governed by the time-dependent Schrödinger equation and the Hamiltonian, which describes the total energy of the system. The Hamiltonian is of the form

$$\hat{H} = \hat{H}_0 + \hat{H}_d, \quad (3.2)$$

where \hat{H}_d is the driving Hamiltonian and is responsible for inducing rotations in the qubit state on the x or y-axis of the Bloch sphere through the use of IQ modulated pulses with specific envelopes for the I and Q components.

To further elaborate, the driving Hamiltonian (\hat{H}_d) can be expressed as [54, 23]

$$\hat{H}_d = -\frac{\Omega}{2} V_0 s(t) (I \hat{\sigma}_x + Q \hat{\sigma}_y), \quad (3.3)$$

where $s(t)$ is a dimensionless envelope function and $V_0s(t)$ sets the amplitude of the drive. The $\frac{\Omega}{2}V_0s(t)$ term represents the Rabi frequency, which determines the speed of the qubit state rotation. The I and Q components refer to in-phase and quadrature components of the IQ modulated pulse, which allow for the control of the rotation axis on the Bloch sphere.

To perform quantum circuits, we use a series of MW pulses, as shown in Fig. 3.2. For example, in the circuit shown below, we apply the MW pulse sequence to implement the X gate and measurement and obtain a bit of information, m :

$$|\psi\rangle \text{ --- } \boxed{X} \text{ --- } \boxed{\text{Measurement}} = m$$

Initially, the qubit could be in the ground state, $|\psi\rangle = |0\rangle$. The X-pulse excites it to the $|1\rangle$ state, and the measurement pulse reads the state of the qubit through the resonator.

In the context of quantum computing, the qubit readout process involves applying MW pulses to the qubit and measuring the state of the resonator to determine the state of the qubit, which can be either "0" or "1". One way to modulate the MW pulses is through Binary Phase Shift Keying (BPSK), in which the phase of the pulse is changed to represent the "1" or "0" state [7]. The received signal is then amplified and demodulated to recover the original message, which corresponds to the initial state of the qubit. In telecommunications engineering, this process can be thought of as similar to sending and receiving a digital BPSK modulated signal over a communication channel.

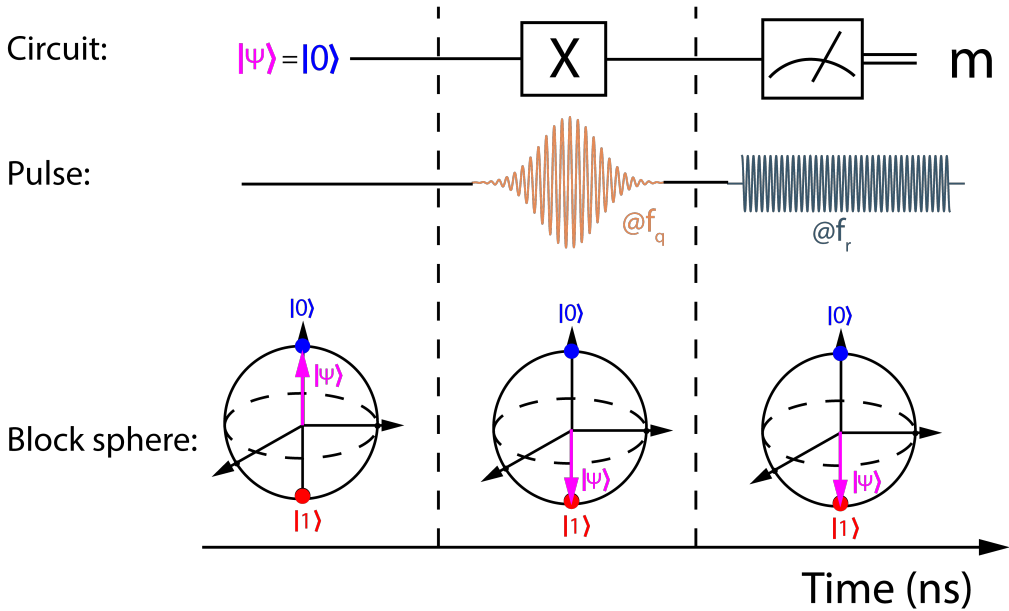


Figure 3.2: (a) Quantum circuit for an X-gate with measurement. (b) Pulse sequence needed to implement the quantum circuit. First a control pulse implemented with a modulated gaussian pulse at qubit's frequency (orange) followed by a readout pulse at resonator's frequency (blue). (c) Bloch sphere representation of the ideal quantum state of the qubit at each time slot. The quantum state finally collapses into one of the two states when measured.

3.1.1 Utilizing IQ Mixers for Precise Quantum State Control and Measurement

To control and measure qubits, we use a combination of electronic components at room temperature and microwave pulse sequences. One such component is the IQ mixer, which allows for precise control of the amplitude and phase of an output signal. By modulating with both in-phase (I) and quadrature (Q) inputs, any desired output

signal can be generated.

The IQ mixer has four ports: RF, LO, I, and Q, Fig. 3.3a. The RadioFrequency (RF) port is the output port when the mixer is used for modulation and the input port when it is used for demodulation. The LO port is the Local Oscillator signal at a higher frequency than the I and Q ports. The I port is the in-phase signal at intermediate frequency (f_{IF}), and the Q port is the quadrature or out-of-phase signal at f_{IF} .

The internal structure of the IQ mixer consists of two mixers and a 90-degree phase shifter. Mixing the input signals produces new frequencies called heterodynes, Fig. 3.3b, and typically only one of these is required in the output signal, with the other being filtered out.

$$f_{RF} = f_{LO} \pm f_{IF}. \quad (3.4)$$

By carefully manipulating the I and Q inputs, the desired output signal can be generated at the RF port.

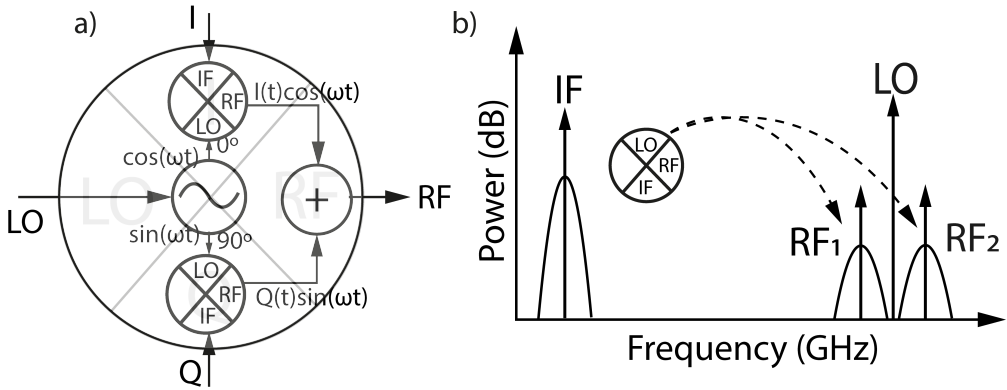


Figure 3.3: (a) A quadrature mixer, or IQ mixer, has 4 ports where I is the in-phase component and Q is the quadrature (or out-of-phase) component and internally consists of two separate mixers and a 90 degree phase shifter. (b) Example of upconverting mixer taking as input an IF and LO signals and giving the two heterodynes as the sum and subtraction as in (3.4).

The IQ mixer is a versatile electronic circuit that is commonly used in communication systems for modulating and demodulating signals. When demodulating, the IQ mixer splits the input signal,

$$s(t) = s_I(t) + js_Q(t), \quad (3.5)$$

and LO into two branches, Fig. 3.4, which are then multiplied to reconstruct the original signal: in the I-branch, the signal $s_I(t) = \frac{s(t)}{2}$ is multiplied by the local oscillator $y_I(t) = \left(\frac{A_{LO}}{2}\right) \cos(2\pi f_{LO}t)$, and in the Q-branch, the signal $s_Q(t) = \frac{s(t)}{2}$ is multiplied by a $\pi/2$ -phase-shifted version of the local oscillator, $y_Q(t) = -\left(\frac{A_{LO}}{2}\right) \sin(2\pi f_{LO}t)$. So, finally we can reconstruct the received signal as

$$s(t) \cdot y(t) = \text{Re} \left\{ s(t) e^{j2\pi f_{LO}t} \right\} = s_I(t) \cos(2\pi f_{LO}t) - s_Q(t) \sin(2\pi f_{LO}t). \quad (3.6)$$

This process allows for the mitigation of phase noise (because the carrier phase can be accurately tracked and compensated for at the receiver), improved power efficiency compared to other modulation techniques, and the ability to capture wideband analog signals using a fixed sampling frequency. Additionally, quadrature sampling can be used to measure the instantaneous magnitude and phase of a signal during demodulation.

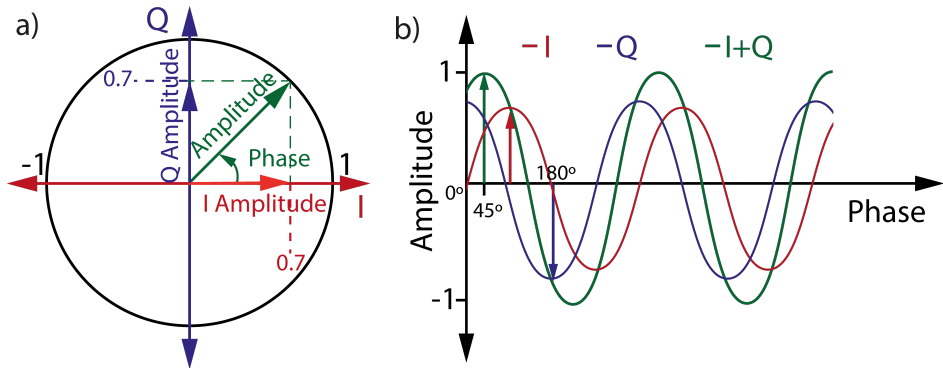


Figure 3.4: (a) Quadrature plot of IQ modulation phasor at 45° configuration. Assuming unity gain in the modulator, to produce a carrier of unity amplitude at 45 degrees, the I and Q inputs must both be DC values of 0.707V. (b) Cartesian plot including other phases. Marked with green arrow, an example if the resulting I+Q signal at 45° .

To read the state of the qubit, we measure the qubit-state-dependent amplitude and phase of a microwave signal reflected (or transmitted) by one of the readout resonators. This is done by sending a short microwave pulse at the readout resonator probe frequency, f_r , to the resonator and then measuring the resulting signal, $s(t)$. The signal can be written as [54]

$$s(t) = A_{RO} \cos(2\pi f_r t + \theta_{RO}), \quad (3.7)$$

where A_{RO} and θ_{RO} are the amplitude and phase that we want to measure, and f_{RO} is the carrier frequency used to probe the resonator. We typically probe the resonator in the dispersive readout context with a frequency $f_{RO} = \tilde{\omega}_r/2\pi$ (2.28), corresponding to ~ 7 GHz.

Alternatively, we can represent the signal using a complex phasor notation that separates the time dependence. This allows us to write the signal as [54]

$$s(t) = \text{Re} \left\{ \underbrace{A_{RO} e^{j\theta_{RO}}}_{\text{phasor}} e^{j2\pi f_{RO} t} \right\}. \quad (3.8)$$

The phasor $A_{RO} e^{j\theta_{RO}} \equiv A_{RO} \angle \theta_{RO}$ is a short-hand notation that fully specifies a harmonic signal $s(t)$ at a known frequency f_{RO} . To perform a qubit readout, we want to measure the “in-phase” component I and the “quadrature component” Q of the complex number represented by the phasor. These can be obtained from [54]

$$A_{RO} e^{j\theta_{RO}} = A_{RO} \cos \theta_{RO} + j A_{RO} \sin \theta_{RO} \equiv I + jQ. \quad (3.9)$$

We then use digital signal processing to calculate the static I and Q components, from which we can determine the amplitude A_{RO} and phase θ_{RO} . To do this, we mix the LO(t) and RO(t) signals to obtain I(t) and Q(t), which contain terms at both sum and difference frequencies.

One specific application of the IQ mixer is in Binary Phase Shift Keying (BPSK), a form of Phase Modulation (PM), Fig. 3.5. Data is transmitted via the two (and only two) possible phase states for the carrier (binary phase). The phase of the carrier is changed to represent the "1" or "0" state of the transmitted data.

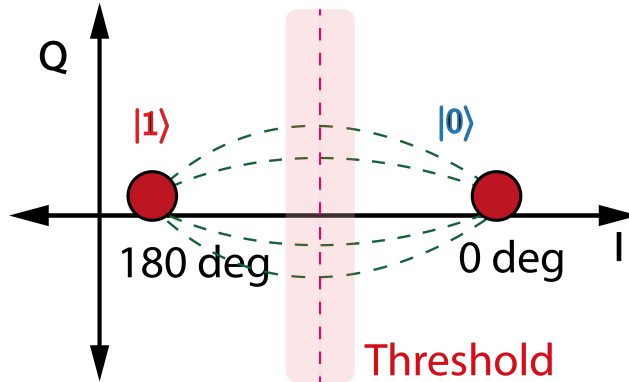


Figure 3.5: Qubit measurement constellation.

In the context of quantum computing, the IQ mixer is used to generate microwave pulse sequences that are applied to the qubit to control its quantum state. These pulse sequences are modulated using the IQ mixer and a local oscillator, and their precise amplitude and phase are important for accurately manipulating the quantum state of the qubit. By carefully calibrating the pulses, it is possible to improve the Signal-to-Noise Ratio (SNR) and distinguish between the ground and excited states of the qubit, which are used for computation.

Overall, the IQ mixer plays a key role in the control and measurement of qubits in quantum computing, allowing for precise manipulation of the qubits through the use of microwave pulse sequences. Its versatility and ability to modulate and demodulate signals make it an essential component in this field.

There are potential issues in the use of IQ mixers, such as LO signal leakage and spurious sidebands. To address these challenges, we employ automatic calibrations using a spectrum analyzer, adjusting both in-phase (I) and quadrature (Q) components to eliminate leakage tones effectively [8, 4].

Real IQ mixers have inherent imperfections, such as skewness and amplitude imbalance between I and Q inputs. To suppress spurious sidebands, we must systematically address these imperfections.

When the IQ mixer is ideal, the IQ output traces a circle in the IQ plane, centered at the origin. However, in non-ideal cases, the output traces an off-origin ellipse. Correcting a 10-degree phase imbalance is crucial as it can cause significant I to Q crosstalk up to 15 dB [8], affecting performance.

Furthermore, the quadrature mixer can have a mediocre matching and LO to RF isolation, leading to undesired signals exiting the RF input port with nearly equal strength as the desired RF signal [8]. Our primary goal is to minimize intermodulation and LO leakage effects by over 40 dB while preserving signal integrity through a rigorous calibration procedure consisting of IQ signal predistortion. This ensures optimal mixer performance, high fidelity, and minimal interference, ultimately enhancing qubit stability.

3.1.2 Uncovering Qubit State through Digital Signal Processing

To calculate the final values of A_{RO} and θ_{RO} , we sample I and Q and then use the following formulas

$$A_{RO} = \sqrt{I^2 + Q^2}, \quad (3.10)$$

$$\theta_{RO} = \arctan\left(\frac{Q}{I}\right) \quad (3.11)$$

To summarize, we perform a measurement on the qubit by sending a microwave pulse to a resonator and measuring the resulting signal. We then use digital signal processing to extract the in-phase and quadrature components of the signal and use these to calculate the amplitude and phase of the signal. By comparing the amplitude and phase for the $|0\rangle$ and $|1\rangle$ states of the qubit, we can determine the state of the qubit.

The analog-demodulated $I_{IF}(t)$ and $Q_{IF}(t)$ signals are converted to digital form and written as

$$I_{IF}[n] = \frac{A_{RO}A_{LO}}{8} \cos(\omega_{IF}n + \theta_{RO}) \quad (3.12)$$

and

$$Q_{IF}[n] = \frac{A_{RO}A_{LO}}{8} \sin(\omega_{IF}n + \theta_{RO}), \quad (3.13)$$

where $n = \frac{t}{\Delta t}$ is the sample number and Δt is the sampling period. The digital demodulation process involves multiplying $I_{IF}[n]$ and $Q_{IF}[n]$ by $\cos(\omega_{IF}n)$ and $\sin(\omega_{IF}n)$ respectively, and averaging the resulting time series to eliminate the $2\omega_{IF}$ component while retaining the IF component. This allows us to calculate the amplitude A_{RO} and phase θ_{RO} of the signal.

The same process can be visualized in the complex I-Q plane, Fig. 3.6a, using the analytic function [54]

$$\begin{aligned} z_{IF}[n] &= I_{IF}[n] + jQ_{IF}[n] \equiv V_I[n] + jV_Q[n] = \\ &= \frac{A_{RO}A_{LO}}{8} [\cos(\omega_{IF}n + \theta_{RO}) + j \sin(\omega_{IF}n + \theta_{RO})] = \\ &= \underbrace{\frac{A_{RO}A_{LO}}{8} e^{j\theta_{RO}}}_{\text{static phasor}} \underbrace{e^{j\omega_{IF}n}}_{\text{rotating term}} \end{aligned} \quad (3.14)$$

where $V_I[n]$ and $V_Q[n]$ are the in-phase and quadrature voltages sampled by the ADC. We can digitally demodulate the time series $z_{IF}[n]$ by multiplying it by the complex conjugate of the oscillatory exponential, resulting in a vector of nominally identical values of the phasor, Fig. 3.6b, [54]

$$z[n] = z_{IF}[n] \cdot *e^{-j\omega_{IF}n}, \quad (3.15)$$

where $\cdot *$ indicates a point-by-point multiplication. This vector can then be averaged to obtain the final value of the phasor, which fully specifies the amplitude and phase of the signal, Fig. 3.6c, [54]

$$\bar{z}[n] = \frac{1}{M} \sum z[n] = \frac{A_{RO}A_{LO}}{8} e^{j\theta_{RO}}. \quad (3.16)$$

Where M is the length of the vector, which is at the end the number averages or “shots” on this vector also usually referred to as Hardware average. Such “single-shot measurement” vector, $\bar{z}[n]$, may then be repeated a large number of times, also referred to as Software average, to obtain an ensemble average $\langle \bar{z}[n] \rangle$, Fig. 3.6d.

The final step in the qubit readout process is to convert the amplitude and phase of the signal into a binary measurement result, $|0\rangle$ or $|1\rangle$ like in Fig. 3.5. It’s important to note that the global value of A_{RO} or θ_{RO} is not what matters; what matters is the change in A_{RO} and θ_{RO} between the $|0\rangle$ and $|1\rangle$ states of the qubit. This allows us to determine the state of the qubit based on the difference in A_{RO} and θ_{RO} , $\langle \bar{z}[n] \rangle$, between the two states. This is typically done using a threshold that separates the two regions of the I-Q plane corresponding to the $|0\rangle$ and $|1\rangle$ states, Fig. 3.5. The threshold can be determined by performing a calibration measurement on the qubit, in which the qubit is repeatedly prepared in both the $|0\rangle$ and $|1\rangle$ states and the resulting I and Q values are recorded. The threshold can then be chosen to maximize the separation between the two sets of points in the I-Q plane.

After determining the threshold, the qubit readout process concludes. As a summary, the whole process for readout of the qubit state involves measuring the qubit’s state-dependent amplitude and phase of a microwave signal reflected (or transmitted) by a resonator. This signal is then converted to digital form and demodulated to extract amplitude and phase information. The binary measurement result is obtained using the threshold, allowing us to determine the qubit’s state.

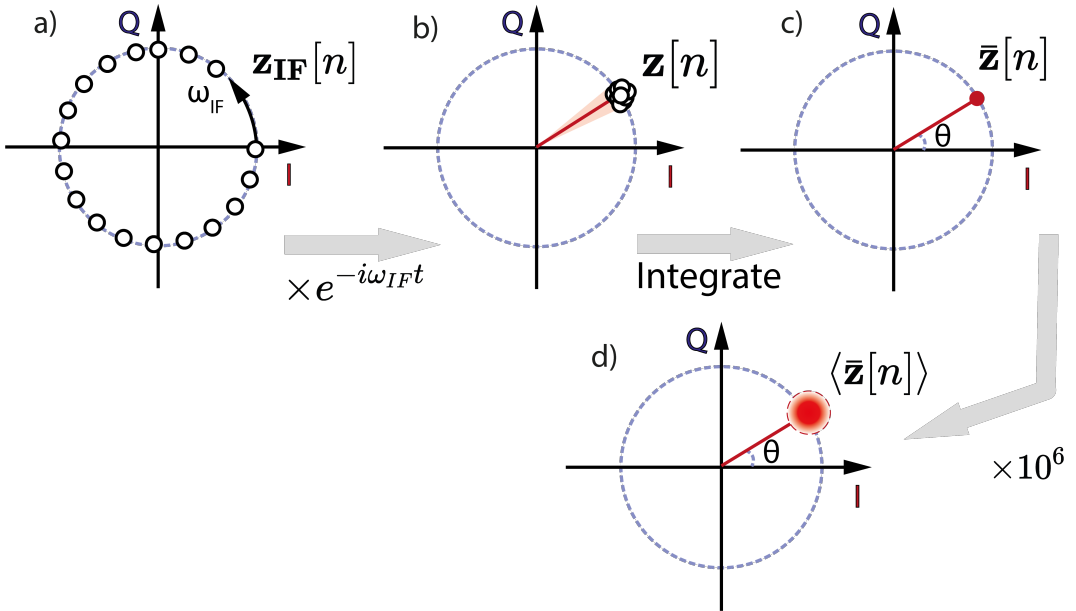


Figure 3.6: Schematic of heterodyne detection technique for digitized I and Q signals coming from the resonator. (a) The white dots represent the sampled points. (b) The sampled traces are post-processed and demodulated by multiplying it by the complex conjugate of the oscillatory exponential. (c) The sampled data points are averaged into a single point in the (I, Q)-plane. (d) To extract statistics of the readout performance, i.e. single-shot readout fidelity, a large number of (I, Q)-records are acquired, yielding a 2D-histogram, with a Gaussian distributed spread given by the noise acting on the signal.

3.2 Elevating Quantum Computing: Qilimanjaro's OS Innovation

Quantum computing is a groundbreaking technology that demands a significant shift in thinking for software developers. Although users may wish to define a circuit or algorithm and get results from the quantum processing unit (QPU), achieving this requires careful consideration of various hardware aspects. These include: converting the specified circuit into a set of microwave pulse sequences, operating multiple remote FPGA boards, periodically performing system calibration, scheduling all operations, reconstructing measurements, storing results, and performing hybrid calculations.

To help streamline this process, Qilimanjaro has created a full-stack software framework that acts as a quantum operating system. With this system, users can create a quantum algorithm using the Qibo language and send it to be executed on various backends, including actual quantum machines or simulated ones [2, 26]. The algorithm is transformed into a program that is loaded onto the FPGAs, which then send pulses to the QPU. The resulting qubit states are digitized, postprocessed with the FPGAs, following the sampling and demodulating procedures explained in section 3.1.2, and stored by the Quantum as a Service (QaaS) part of this Quantum Operating System (QOS) before being sent back to the user.

From a software perspective, the QOS can be divided into several layers [40], as shown in Fig. 3.7a:

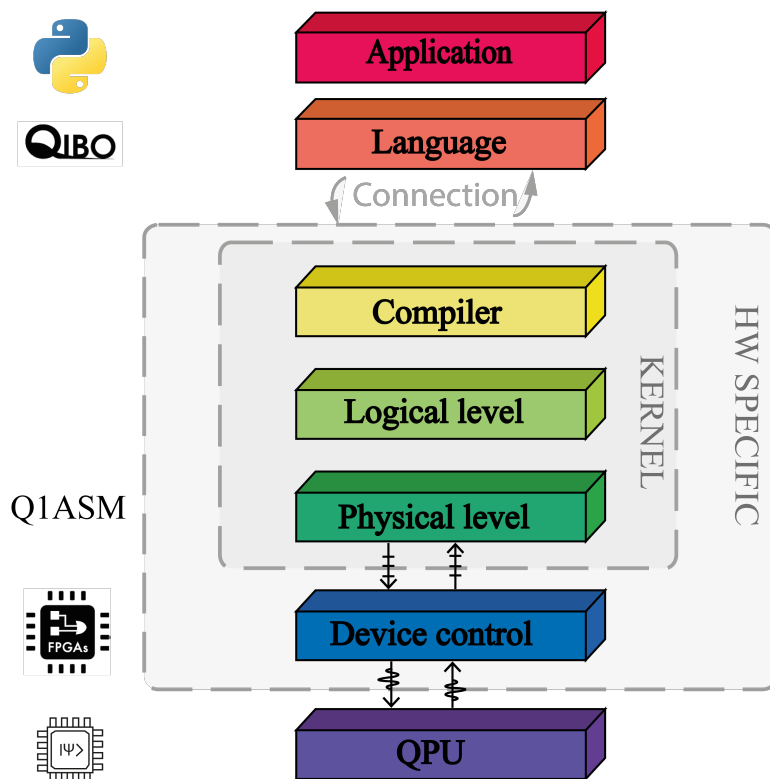


Figure 3.7: Quantum operating system structure. A quantum program is implemented making use of Qibo language by the user. Qibo transforms the algorithm into quantum circuits that the compiler link in low-level libraries like Qilib transforming the logical qubit operations to physical operations by mapping the physical locations of qubits making use of a database. The physical level finally generates a Q1ASM program that can be sent via ethernet to Qblox machines and this is interpreted by the FPGAs inside that send the analog pulses to the QPU and digitize its analog response. Thanks to all these layers, the user can send its program to different quantum computers or simulators without having to worry about the HW specific block.

1. Application: Allows programmers to use a domain-specific language (DSL) or access libraries of useful routines.
2. Language: Converts the program into a quantum intermediate representation (QIR) that is easier for the compiler to analyze and manipulate. This QIR is in the form of quantum circuits.
3. Compiler: Optimizes the QIR and maps the qubits to physical locations on the quantum data plane and uses calibration data specific to each line and qubit.
4. Logical layer: This layer generates the sequence of operations that execute the desired quantum circuit. It converts gates to pulses and uses calibrations, tuning, and microinstructions to do so.
5. Physical layer: translates these operations into pulse sequences that can be executed on the hardware backend. In our specific case, this layer generates Q1ASM code, a pseudo-assembly language that contains the program and waveforms to be executed in the FPGA. This language follows OpenQASM [22, 21] directives and is used in equipment produced by Qblox.

In summary, Qilimanjaro’s QaaS is a full-stack software framework that makes it easy for users to create and execute quantum algorithms, while also handling the complexities of quantum hardware and software integration. It provides a high-level interface for users and abstractions that allow for flexibility and scalability as quantum computing technology continues to evolve.

Debugging and verifying quantum programs are crucial challenges in the field of quantum computing. While classical computers allow programmers to stop execution at any point and examine the current state of the program, quantum computers have an exponentially large state space that is collapsed by physical qubit measurements and cannot be restarted once a measurement has been made [40]. This makes the design of debugging and verification techniques for

quantum programs a fundamental and challenging requirement for progress in quantum computing development. The QaaS software framework offers a solution to these challenges by providing a full-stack software framework that acts as a quantum operating system and enables the user to mix gate- and pulse-level descriptions as needed for various experiments.

3.3 Enhancing Quantum Computing Performance through Advanced Microwave Packaging Techniques

Microwave packaging is a critical aspect of building scalable quantum processors using superconducting qubits. In this section, we present an approach to microwave package design that focuses on material choices, signal line engineering, and spurious mode suppression. We follow guidelines from [46] and use simulations and measurements to develop a 12-port microwave package for use in a dilution refrigerator.

The microwave package serves several important purposes: it suppresses the coupling of the qubits to external decoherence channels, such as environmental electromagnetic noise; it accommodates qubit control channels to and from the quantum processor; and it sinks excess and latent thermal energy due to qubit control and readout operations. Our design consists on a superconducting qubit package inside a dilution refrigerator, Fig. 3.8a, consisting of a copper housing, Fig. 3.8b, a two layer PCB to perform signal fan out, Fig. 3.8c, and a set of microwave non-magnetic connectors and superconducting coaxial cable assemblies (*Appendix A*). By carefully designing and optimizing the microwave package, we can help ensure the reliable operation and scalability of the quantum processor.

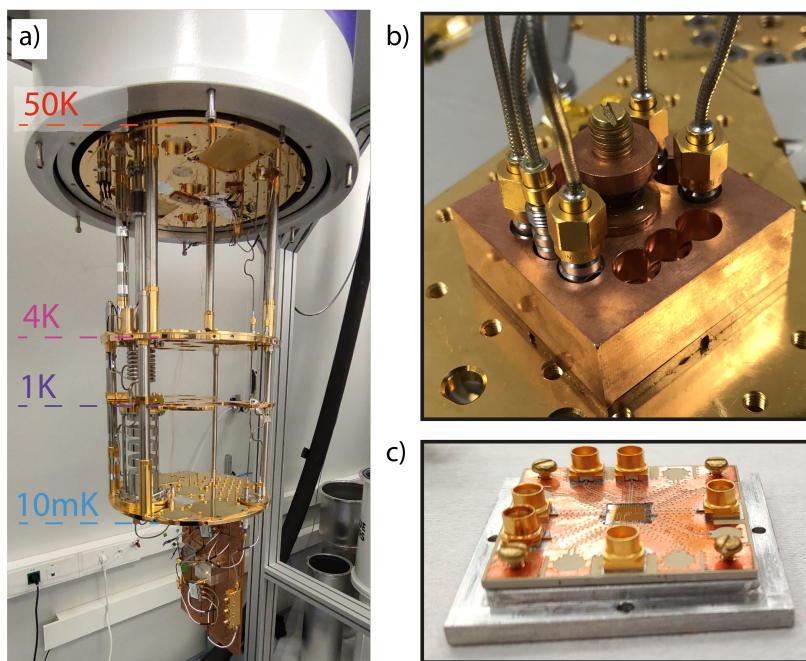


Figure 3.8: (a) Dilution refrigerator with multiple temperature stages holding the qubit chip enclosed in a microwave package. The microwave package interfaced with microwave lines is mounted on a cold finger in the mixing chamber reaching a base temperature of approximately 10 mK. (b) MW package with connected non-magnetic cables and superconducting coil. (c) PCB for signal fan out with SMP connectors mounted on top of the housing base. Chip wirebonded in the middle.

The goal of our system is to cool the qubit to a temperature of 10 mK, at which point the ground state, $|0\rangle$, has an occupancy of around 99.999% due to the Boltzmann distribution [7]. To ensure reliable signal transmission, we use custom-assembled CuBe SMA to SMA coaxial cables from the room temperature flange to the 4K flange, and NbTi coaxial cables from the 4K flange to the mixing chamber at 10 mK. NbTi is a costly material due to its low thermal conductivity

and electrical superconductivity at low temperatures, and requires special ultrasonic soldering. All cables are carefully assembled and soldered to meet our specific requirements, and all cables installed in the fridge show return losses (RL) higher than 20 dB, *Appendix A*. We use attenuators on the input lines to prevent thermal noise from reaching the qubit. The configuration of the transmission lines connecting the quantum processor unit inside the mixing chamber of the dilution refrigerator to the room temperature electronics is shown in Fig. 3.9.

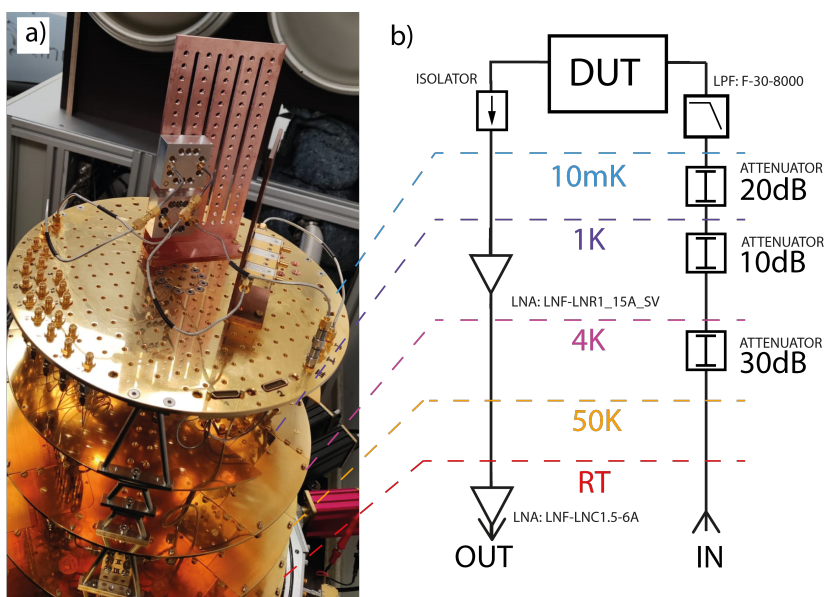


Figure 3.9: (a) Samples inside the Qinu Sinludi XL dilution refrigerator. (b) Setup schematic of cryogenic components. IN and OUT ports as P1 and P2 of Fig. 1.1. Attenuation is distributed at different flanges associated with different temperatures to avoid thermal noise to affect the qubit. A filter is added to suppress unwanted transitions or couplings. The signal goes through the QPU feedline and is amplified with the chain of amplification. An isolator is placed before the first amplifier to avoid any backaction to the qubits.

We use isolators on the output line to effectively suppress thermal noise traveling from the higher temperature stages avoiding any backaction to the qubits while still allowing the signal to pass through without significant attenuation. We also employ a cryogenic low pass filter (LPF) at the mixing chamber input line to filter out any spurious frequency components that may cause unwanted transitions or couplings. Finally, we enhance the weak outgoing signal carrying information from the devices using a cryogenic high-electron mobility transistor (HEMT) low noise amplifier (LNA) with minimal attenuation between the QPU and the LNA, as any attenuation before the first LNA significantly contributes to the total amplification chain, according to Friis' equation

$$NF_{total} = 10 \log_{10} \left(n_1 + \sum_{i=2}^M \frac{n_i - 1}{\prod_{j=1}^{i-1} g_j} \right), \quad (3.17)$$

where $n_i = 10^{\frac{NF_i}{10}}$ and $g_i = 10^{\frac{G_i}{10}}$ are the noise and gain at each stage of the amplification chain. Our total noise figure (NF) is approximately 0.022 dB, with a total chain gain of 78 dB including an extra amplifier at room temperature to further boost the signal before it is acquired.

To further improve SNR, a Travelling Wave Parametric Amplifier (TWPA) [72] can be used as the first stage of amplification before the HEMT LNA. That will improve the NF_{total} almost an order of magnitude, down to around 0.004 dB¹ also improving the total chain gain to up to around 98dB [72].

¹In Quantum Computing context, noise temperature is more common than Noise Figure. They are easily related with this formula:

$NF = 10 \cdot \log_{10} \left(\frac{T_N}{T_{ref}} + 1 \right)$. Where T_N is the noise temperature and T_{ref} is the reference temperature (300K).

3.3.1 Optimizing a 12 Port PCB Housing for Quantum Computing

The design of the 12-port device presented in this work was inspired by the exploration of various 8-port PCB housings in previous studies [5, 15, 71]. The device consists of a base, a PCB lid, and a lid, as shown in Fig. 3.10. This configuration allows to reuse the base and lid for other PCB and PCB lid configurations. In order to optimize the device for both thermalization and the application of a global constant magnetic field, we chose to use Oxygen-Free High Thermal Conductivity Copper (OFHC) for the housing material. OFHC allows for the penetration of magnetic fields from the coil mounted on top of the housing, while also providing high thermal conductivity to keep the sample as cool as possible.

The package without the PCB lid would have the potential to act as a microwave cavity when excited by the fields radiated from the PCB. When the qubit frequency and the package mode frequency are close in frequency, the energy levels of the two systems can hybridize, allowing for the coherent exchange of excitations between the qubit and the mode. However, the lossy nature of many package modes can lead to a reduction in the qubit lifetime (T_1) due to the Purcell effect (the qubit losing its energy via relaxation to cavity modes). To address this issue, the PCB lid is designed to divide the potential cavity created by the housing into smaller sub-cavities (Fig. 3.10). This increases the fundamental mode frequency of the package, moving it further away from the qubit control and readout frequencies, thereby reducing the coupling to cavity modes.

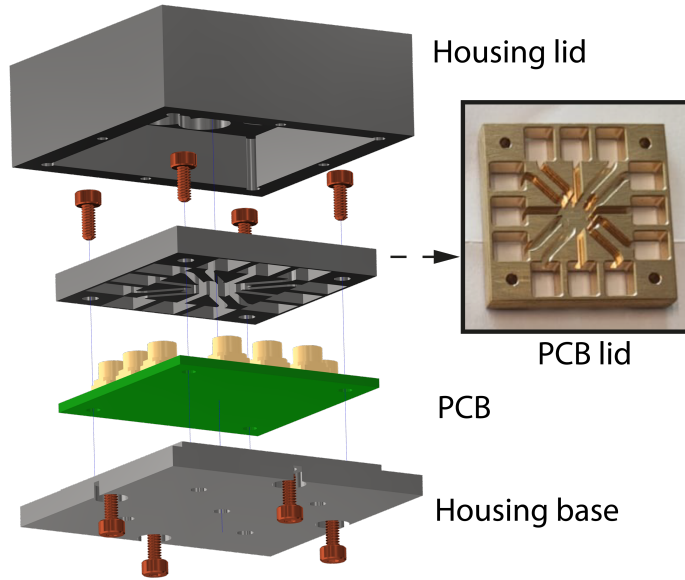


Figure 3.10: Housing design 3D assembly view showing: Housing lid, housing base and PCB lid with picture of the inner face.

The lowest resonance frequency mode of a rectangular cavity, known as the TE_{101} mode, can be calculated using [74]

$$f_{mnl} = \frac{c}{2\pi\sqrt{\mu_r\epsilon_r}} \sqrt{\left(\frac{m\pi}{a}\right)^2 + \left(\frac{n\pi}{b}\right)^2 + \left(\frac{l\pi}{d}\right)^2}. \quad (3.18)$$

Here, μ_r represents the relative magnetic permeability of the material (vacuum), ϵ_r represents the relative permittivity of the material (vacuum), c is the speed of light, a , b and d are the three dimensions of the cavity (width, height and length). m , n , and l represent the mode number in the different axes, being the first mode at $mnl = 101$. However, the presence of openings at the edges of these subcavities increases the effective volume of the cavity, resulting in a lower resonance frequency than expected. The housing lid has dimensions of approximately $33 \times 35 \times 7.5$ mm, creating an unwanted

cavity with a first resonant mode at 6.24 GHz, which is within the frequency band of operation of the qubits (typically 4-7 GHz). By adding the PCB lid, the largest sub-cavity has dimensions of approximately $6.42 \times 6.42 \times 3$ mm and a first resonant mode of around 31.5 GHz, as shown in the ANSYS HFSS eigenmode simulation in Fig. 3.11b.

To identify package modes through measurement, we use a Vector Network Analyzer (VNA) to measure the transmission parameters for opposing ports of the PCB at room temperature in the absence of a chip. This method relies on the coupling between the launch of a signal in an unpopulated chip cavity and the resonances to identify spurious modes in the system. The protective effect of the PCB lid is clearly visible in the response, with a resonance at the operation frequency being observed and attenuated up to 30 dB by the presence of the PCB lid (Fig. 3.11a).

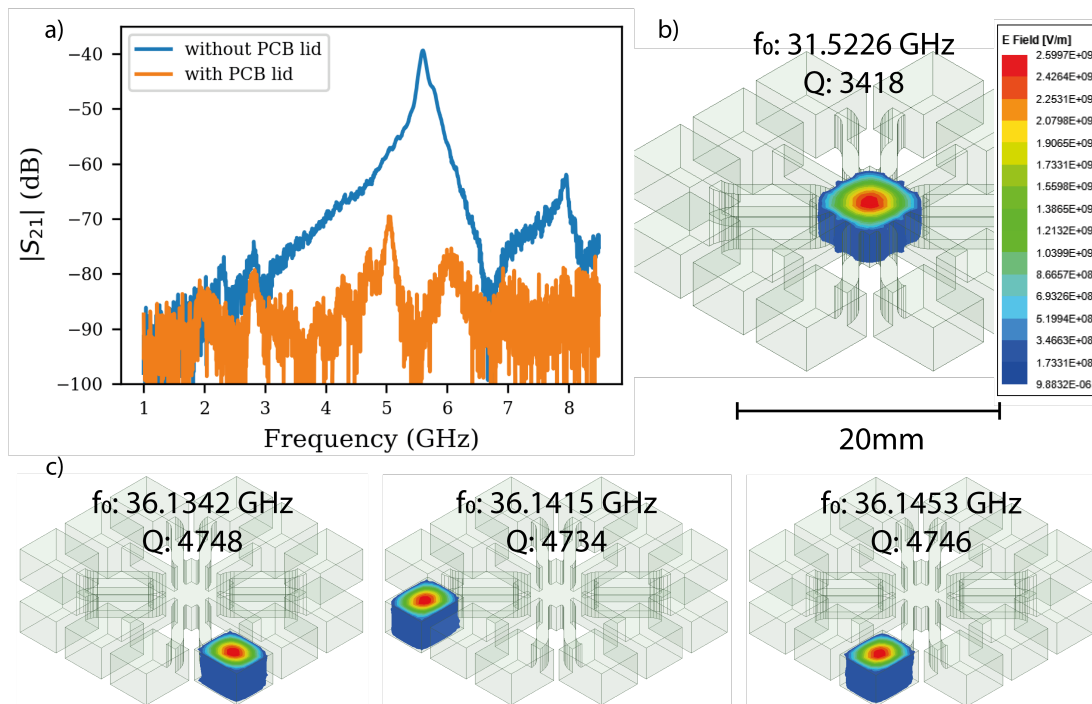


Figure 3.11: (a) Measured spectrum with and without the PCB lid showing the appearance of an unwanted resonance at frequency band of operation when PCB housing is lacking the PCB lid (blue) and suppressing the mode with the PCB lid included (orange). (b) Eigenmode simulation of the first resonant mode inside the PCB housing with the PCB lid at the chip sub-cavity is found to be 31.5 GHz with field distribution as shown. (c) Eigenmode simulation of the second, third and fourth (left to right) resonant mode inside the PCB housing with the PCB lid. Being resonances of the subcavities where the connectors will be placed.

3.3.2 Design and Characterization of a 12 Port PCB for Quantum Computing Applications

The PCB to hold the chip, Fig. 3.8c and Fig. 3.10, is designed for reuse in a variety of experiments, with all lines treated as microwave lines to allow for flexibility in choosing launcher positions on the chip. To ensure high return losses and compatibility with SMP connectors, the lines are grounded coplanar transmission lines with a 50 ohm impedance. Push-in connectors were chosen for their non-bulky, non-magnetic design and ease of mounting and soldering compared to through hole or edge connectors [58]. These connectors have a frequency range of DC-40 GHz for SMP and DC-18 GHz for SMA-type, covering the operating range of most superconducting qubits.

The PCB layer stackup consists of 35 μm of copper top and bottom layers and Thermoset Microwave Material (TMM)10i dielectric from Rogers Corp. in the middle layer. This dielectric has a high dielectric constant, $\epsilon_r=9.8$, a low dissipation factor of 0.002 at 10 GHz and a low thermal coefficient.

To secure the chip in place, a $5.1 \times 5.1 \times 0.5$ mm pocket is drilled in the middle of the PCB. This pocket, along with 25 μm diameter aluminum thermosonically bonded wirebonds, will hold the chip in place using wedge bonding.

Good impedance matching is crucial for minimizing insertion losses and improving signal integrity, both of which are essential for high-fidelity control and readout of qubits. In one-qubit gates, distortions such as rise time and settling time can lead to under and over rotations and reduce gate fidelity. In two-qubit gates, like the controlled-phase gate [68], deviations from carefully shaped flux pulses can result in leakage away from the computational subspace [24, 46], leading to reduced computational performance. Adjacent lines can couple through their mutual capacitance and inductance, so the lateral walls formed by the vias on either side of the coplanar transmission line serve to prevent the excitation of additional waveguide modes and

suppress potential crosstalk, creating a "channelized coplanar waveguide" structure [62]. Other solutions also use stripline to further shield PCB lines from the environment [3].

Several 3D electromagnetic simulations were conducted using ANSYS HFSS to optimize the layout and minimize losses while maintaining good matching at the operating frequencies. Testbench models were used to test various parameters and observe their effects on the system in a controlled environment with lower computational cost than simulating the entire PCB with 12 launchers and connectors. Some of the most relevant testbenches are shown in Fig. 3.12.

The first conclusion, based on the comparison of Fig. 3.12 traces for testbenches A and B, is that vias are necessary to connect the ground planes [77, 88, 79]. The absence of vias resulted in spurious resonances between 4 and 8 GHz, while adding stitching vias with a separation of less than $\lambda/4$ improved the return loss (RL) and matching. The final design includes shielding vias in a double fence configuration with a 0.8 mm distance between them, corresponding to $\lambda/20$ at 8 GHz with the current stackup.

The second conclusion, based on the comparison of Fig. 3.12 traces for testbenches B, C, and D, is that the footprint provided by the manufacturer was sufficient for this stackup and frequency range, although a slight improvement was observed by adding vias in the ground plane surrounding the footprint.

The third conclusion is that the thermal relief can produce spurious resonances similar to those of slot antennas. The thermal relief is added to facilitate the non-dissipation of heat during soldering, but it can also act as an antenna if not properly designed. By optimizing the size and shape of the thermal relief and adding vias to connect the ground planes, the resonance was suppressed.

Overall, the design of the PCB and its various components, including the transmission lines, connectors, and thermal relief, was optimized through simulation and testing to ensure high performance and compatibility with quantum computing applications. A microwave package able to host quantum processors up to 12 ports,

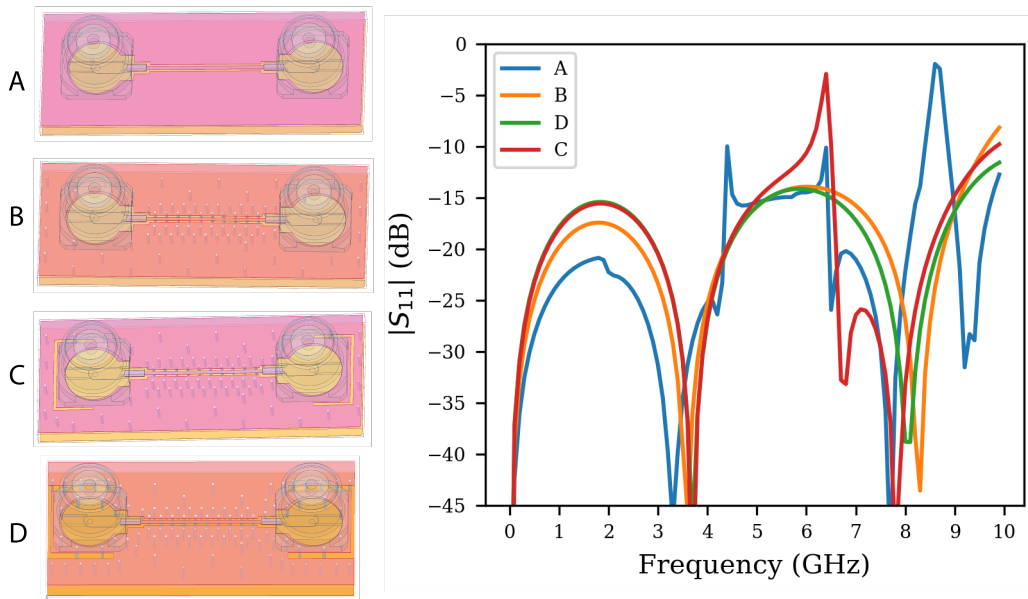


Figure 3.12: Different testbenches $|S_{11}|$ simulation results. The testbenches showed in the top part correspond to; A: no vias, B: shielding vias with 0.8mm separation, C: B with thermal relief for connectors with 0.2mm width, D: B with thermal relief for connectors with 0.5mm width. Showing that D configuration is what better results gave without spurious and that's the configuration that was used for the final PCB design.

around 5 qubits including flux bias lines and drive lines, has been designed, built and characterized. Optimal point between vias spacing and position has been found with simulation. Thermal relief and vias have been added to the footprint and optimized for better impedance matching with simulation. No undesired modes are generated below 10 GHz, thus, not affecting the operating frequencies in the 4 to 8 GHz range.

Chapter 4

Resonator Design for Quantum Computing: 3D Transmon in a Rectangular Cavity Resonator and Transmission Line Resonators

This chapter presents the design of our quantum processing unit (QPU) chips, featuring a single qubit prototype with a 3D transmon in a rectangular cavity resonator for enhanced qubit coherence. We also explore the capabilities of transmission line resonators for quantum computing and optimize their functionality through reflection measurements and data fitting. Through detailed simulations and design considerations, this chapter highlights the significance of resonator design in quantum computing, contributing to the advancement of more robust and scalable quantum information processing.

4.1 Enhancing Qubit Coherence with a 3D Transmon in a Rectangular Cavity Resonator: Design and Simulation

The 3D transmon qubit [51] consists on a single transmon qubit chip placed in the center of a rectangular cavity resonator, Fig. 4.1a. The usage of a three-, rather than a two-dimensional cavity (the meandered TL resonator), leads to longer coherence times by enabling increased control over the interaction of the transmon with its environment which constitutes a major source of decoherence for the transmon states [78, 70].

The rectangular resonator cavity is used to isolate, couple and measure the transmon qubit, maximizing the coupling to the lowest frequency TE_{101} mode at $\omega_c/2\pi \approx 7.5$ GHz and second mode, TE_{102} , at 10 GHz, Fig. 4.1b, as seen in simulation and analytical calculation (3.18). We choose d (cavity's length) to be a wavelength long at the resonant frequency [74] and $b < a < d$, Fig. 4.1a, which makes the dominant resonant mode (lowest resonant frequency) to be the TE_{101} mode [74]. After choosing the coarse values we adjust a fine value using eigenmode simulation with ANSYS HFSS. We draw a rectangular cavity with rounded edges of radius $b/2$ to avoid peak effects at sharp corners [31].

Due to the Purcell effect (section (2.5)), the qubit finds an easier way to loose its energy via relaxation to cavity modes, thus decreasing relaxation time T_1 the higher it is coupled to the outer world [34]. So, we want the cavity decoupled from the external world, which in practice means to have a very high coupling coefficient,

$$g_c = \frac{Q_i}{Q_e}, \quad (4.1)$$

where Q_i is the internal quality factor, dependent on design, material and polishment, and Q_e is the external quality factor that de-

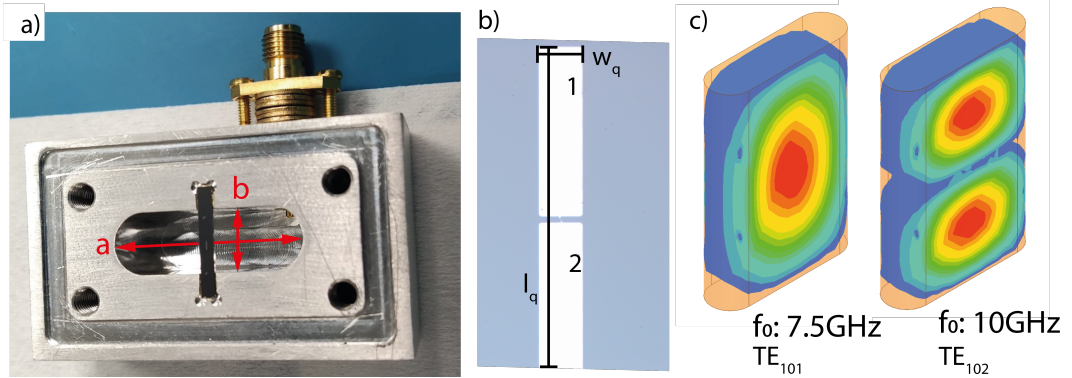


Figure 4.1: 3D transmon design. This design implements the circuit of Fig. 4.2. (a) Picture of half bottom cavity part with SMA connector as output port and 3D transmon chip in the center of the cavity. The aluminum pads can be seen in the middle of the chip. a and b showing cavity's width and height. (b) Microscope picture of the 3D transmon showing aluminum pads 1 and 2 and the Josephson Junction on top of silicon (blueish). Total length and width of the capacitor paddles are noted with l_q and w_q respectively. (c) Eigenmode simulation of the cavity first two cavity modes electric field distribution with ANSYS HFSS.

depends on the position of the ports, the further from the center of the cavity the tip of the port is placed, the lower Q_e is obtained.

The insertion loss of a resonator, or the deviation of peak transmission from unity,

$$L_0 = -20 \log \left(\frac{g_c}{g_c + 1} \right), \quad (4.2)$$

is dependent on the coupling coefficient g_c (4.1) and can be controlled by the choice of the coupling capacitance. In the overcoupled regime, the resonator will show near unity transmission but will have a low loaded quality factor [39].

We want to operate the system in the strong dispersive limit, where the qubit introduces a state-dependent shift on the cavity, which is the basis of the qubit's readout mechanism (2.4)[70, 10]. To be in the strong dispersive limit we choose $|\Delta| \gg g/2\pi$, where g is the coupling of the qubit to the cavity and $|\Delta| = |f_r - f_q|$ is the detuning between the cavity and the qubit frequency. We choose $g/2\pi=100$ MHz and $f_q=5$ GHz.

The total capacitance accounts to (2.15) where C_S is designed to obtain a certain E_C (2.14)(typically of ~ 300 MHz) and C_{gnd} is the capacitance to ground of the aluminum pads, Fig. 4.2. It is difficult to analytically calculate the total capacitance of the transmon qubit inside the cavity, because the capacitance to ground, C_{gnd} , is defined by the geometrical distance of the capacitor pads to the cavity walls. Using ANSYS Maxwell 3D electrostatic simulations, we are able to extract the resultant capacitance matrix.

The total capacitance, C_Σ , tunes the frequency of the qubit as [92]¹

$$\omega_q = 9.5 \frac{e^2}{\hbar C_\Sigma}. \quad (4.3)$$

¹ Assuming $\frac{E_J}{E_C} = 50$, then 2.13 $\omega_q = \frac{\sqrt{8E_C(50E_C)}}{\hbar} = 19 \frac{E_C}{\hbar}$ and finally combining with 2.14.

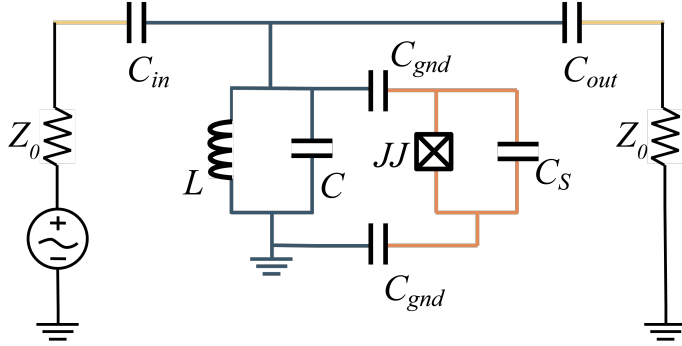


Figure 4.2: Circuitual equivalent of a 3D transmon like the one shown in Fig. 4.1. The cavity acts as a readout resonator (blue) that is capacitively coupled to the qubit (orange). The SMA ports couple capacitively to the mode of the cavity to the external readout circuitry (yellow).

The geometry of the transmon circuit with its relatively long shunt capacitors offers an elegant way for coupling the transmon qubit to the cavity. The paddles serve as an electric dipole antenna of length l_q . For a rectangular cavity with the qubit placed in the center [92]:

$$g = -el_q \sqrt{\frac{2\omega_r}{\hbar\epsilon_0 V}}, \quad (4.4)$$

where V is the volume of the cavity [92]

$$V = (a - b)bd + \frac{\pi}{4}b^2d. \quad (4.5)$$

Combining (4.3) and (4.4) we find the geometry of the aluminum pads from Fig. 4.1b: $l_q=1133.5 \mu m$ and $w_q=144 \mu m$ for $g/2\pi =108$ MHz, $\omega_q/2\pi =5$ GHz and $\omega_r/2\pi =7.5$ GHz.

4.2 Exploring the Capabilities of Transmission Line Resonators for Quantum Computing

Transmission Line Resonators (TLRs) are commonly used as qubit readout resonators in quantum computing due to their fast and efficient readout capability and ability to multiplex multiple elements using a single feedline, Fig. 2.8a. TLRs are typically implemented using CoPlanar Waveguide (CPW) lines made of aluminum on a silicon substrate, Fig. 2.6c. These resonators have a geometric capacitance and inductance per unit length, C_l and L_l respectively, which can be calculated from the cross-section dimensions of the CPW, Fig. 4.3a. TLRs offer advantages over both lumped-element LC resonators and rectangular cavity resonators, like a higher quality factor, higher mode isolation, easier integrability with other components of the chip, and easier to manufacture. These advantages makes them a popular choice in quantum computing. However, TLRs do have a larger footprint² than lumped-element LC resonators, which can be mitigated by using meandering patterns. TLRs also have the ability to store photons over a long time scale when undercoupled with a large quality factor due to the absence of resistivity of their superconducting material. The resonant frequency of a TLR is controlled by its length and its loaded quality factor is controlled by its capacitive coupling to input and output transmission lines. The wavelength of the propagating wave in a TLR in relation to the LRC equivalent is given by [36]

$$\lambda = \frac{2\pi}{\omega} \sqrt{C_l (L_l^m + L_l^k)}, \quad (4.6)$$

where L_l^m is the geometric inductance and L_l^k is the temperature dependent kinetic inductance. For superconductors, L_l^k refers to the inertia of moving Cooper pairs. L_l^k scales with the temperature de-

²i.e. a 6.4 GHz $\lambda/2$ CPW TLR on silicon is 9.3mm long.

pendent London penetration depth. In TLR the kinetic inductance is significantly smaller than the geometric inductance.

At resonance, the properties of a TLR can be approximated by those of a lumped element, parallel LCR resonator with L, C, and R [39]

$$L_n = \frac{2L_l l}{n^2 \pi^2}, \quad (4.7)$$

$$C = \frac{C_l l}{2}, \quad (4.8)$$

$$R = \frac{Z_0}{\alpha_{att} l}. \quad (4.9)$$

Here, l is the physical length, n denotes the resonance mode number ($n = 1$ for the fundamental mode), Z_0 is the characteristic impedance and α_{att} is the attenuation constant.

When coupled to a transmission line, as in Fig. 2.6, a resonator acts as a short to ground at the resonant frequency, causing a dip in transmission at the resonant frequency. This is mathematically demonstrated looking at the transmission line impedance equation for a lossless line [74]

$$Z_{in} = \frac{Z_L + jZ_0 \tan(\beta l)}{Z_0 + jZ_L \tan(\beta l)}, \quad (4.10)$$

where Z_L is the impedance of the load and βl is the electrical length (l being the physical length and β being the wavenumber). For an open circuit load, $Z_L = \infty$, then (4.10) is $Z_{in} = -jZ_0 \cot \beta l$ and if the physical length is $\frac{\lambda}{2}$, then the impedance of the transmission line is $Z_{in} = j \cot \frac{2\pi}{\lambda} \frac{\lambda}{2} = j \cot \left(\frac{\pi}{2} \right) = 0$ and thus the electromagnetic signal will flow from the feedline towards the resonator at the resonant frequency. There are two common ways to implement a TLR: the $\lambda/2$ resonator, which is open at both ends, and the $\lambda/4$ resonator, which has one open end and one shorted end. Capacitive coupling is used to

connect the resonator to the feedline, with the electromagnetic field being stronger at the first resonant mode, near the open end for $\lambda/2$ resonators, as shown in Fig. 4.3b and c.

The resonant frequency of these resonators can be calculated alternatively to (4.6) by using the physical length, l , and the effective permittivity, ϵ_{eff} , which takes into account the relative permittivity of the media through which the wave is traveling [74]

$$f_0 = \frac{c}{\sqrt{\epsilon_{eff}}kl}. \quad (4.11)$$

Here, k is 2 for $\lambda/2$ resonator and 4 for $\lambda/4$ resonator. The effective permittivity of a CPW line on top of a silicon substrate is approximately calculated by taking the average of the permittivity of silicon and air:

$$\epsilon_{eff} = \frac{1}{2}(\epsilon_{r_{silicon}} + \epsilon_{r_{air}}). \quad (4.12)$$

In this case, the permittivity of silicon is 11.45 (normally 11.68 at room temperature, but we adjust it to 11.45 for operation below 20 mK) [56, 55] and the permittivity of vacuum is 1, resulting in an effective permittivity of 6.225. This simplified method is valid when the thickness of the substrate is much larger than the thickness of the metal and the gap distance. For more complex cases, the effective permittivity can be calculated using elliptical integrals [87].

The resonant frequency of the resonator can be shifted due to capacitive loading caused by the input/output lines. Consequently, the loaded resonator will resonate at a lower frequency with higher coupling. The loaded resonant frequency is given by an equation involving the ideal resonant frequency, $\omega_{\lambda/2}$ [38]

$$\omega_r = \frac{\omega_{\lambda/2}}{1 + Z_0 \cdot \omega_{\lambda/2} \cdot C_{eq}}, \quad (4.13)$$

and the effective capacitance

$$C_{eq} = \frac{C_k C_g}{C_k + C_g}. \quad (4.14)$$

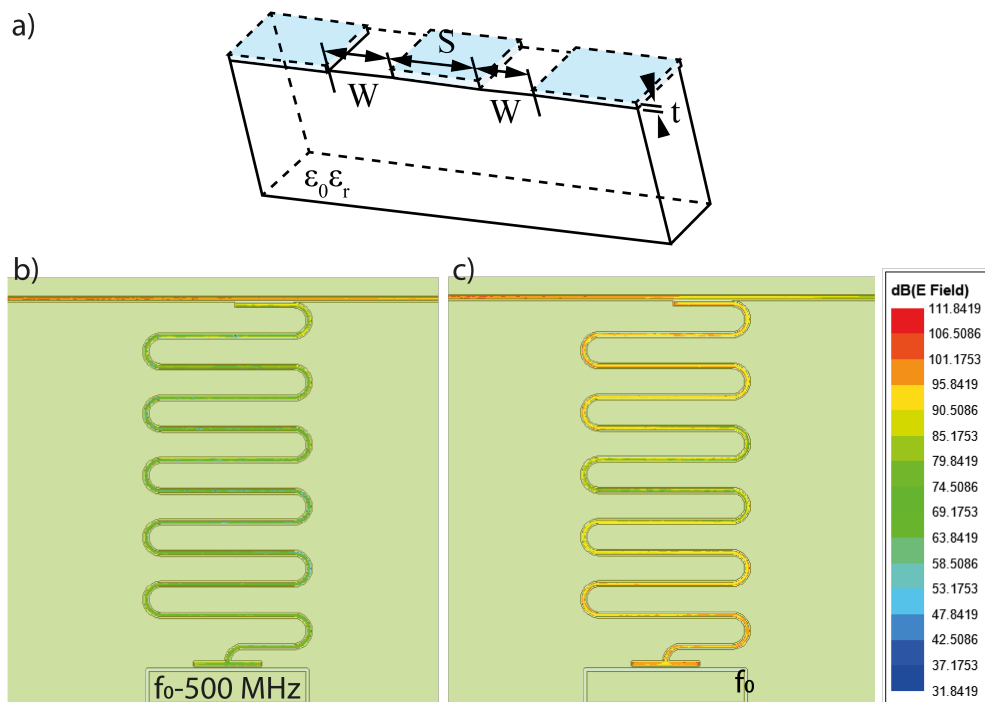


Figure 4.3: (a) CPW structure with a central conductor width S , central conductor to ground plane width W and thickness t , placed on a dielectric material of permittivity $\epsilon = \epsilon_0\epsilon_r$. (b) ANSYS HFSS Modal simulation of the electric field distribution of a $\lambda/2$ CPW resonator capacitively coupled to the feedline at a frequency 500 MHz away from resonator resonant frequency. In this case the electric field is in the feedline and the resonator has no electric field in it. (c) ANSYS HFSS Modal simulation of the electric field distribution of a $\lambda/2$ CPW resonator capacitively coupled to the feedline at the resonant frequency of the resonator. In this case, the electric field then is transferred to the resonator and the maximum field is at the ends of the resonator as predicted.

The capacitance C_g arises due to the equivalent capacitive impedance seen from the edge of the resonator towards the qubit, thus, controlling the coupling strength [82]

$$g = 2 \frac{C_g}{C_\Sigma} \sqrt{\frac{\hbar \omega_r}{2C}} \frac{e}{\hbar}, \quad (4.15)$$

while the capacitance C_k represents the capacitance connected to the feedline [8]

$$C_k = \sqrt{\frac{\pi}{4Z_0^2 \omega_r^2 Q_L^2}}. \quad (4.16)$$

Here, the loaded quality factor of the resonator (Q_L),

$$Q_L = \frac{1}{\frac{1}{Q_e} + \frac{1}{Q_i}}, \quad (4.17)$$

which is affected by the resistive loading, can be controlled through the choice of coupling capacitance, C_k , in the overcoupled regime ($Q_e \ll Q_i$). In the undercoupled limit ($Q_e \gg Q_i$), the loaded quality factor will saturate at the internal quality factor, which is determined by the intrinsic losses of the resonator [39].

A microscope picture of planar implementation of circuit Quantum Electro-Dynamics (cQED) system as the one in Fig. 2.8a is shown in Fig. 4.4. Typical cQED system includes a dispersive read-out circuit with several qubits coupled to resonators connected to the same feedline. This circuit also demonstrates the use of the drive line (purple) for controlling the qubits at their frequency f_q , flux bias line (light green) for tuning the qubits' frequency using current to induce a magnetic field, and resonator buses (pink) for allowing communication between the qubits. To accurately control qubits, it is essential to have carefully designed microwave feed lines. For fixed-frequency transmons, this involves the addition of a capacitively coupled drive line for X- or Y- control of the qubit. On the other hand, flux-tunable

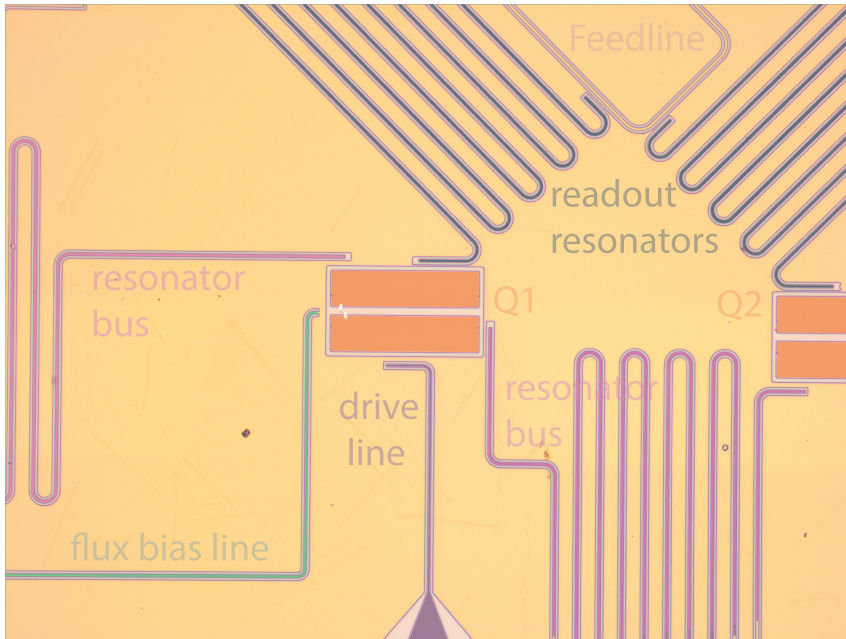


Figure 4.4: False-colored microscope image of a part of a 5 qubit device serves as a representative example of a planar cQED system. The chip architecture features a dispersive readout circuit with several qubits (orange) coupled to resonators connected to the same feedline. Implements a similar circuit and maintaining the same color code as the one in Fig. 2.8a. The circuit also showcases the use of the drive line (purple), flux bias line (light green), and resonator buses (pink).

elements require the use of inductively coupled flux-bias lines, allowing for fast and efficient readout and the potential for use as a quantum bus (two transmons can interact via a mediating resonator mode to realize quantum operations) [10]. However, the incorporation of all these features can also lead to increased coupling to the environment and potentially higher dissipation rates in the device [38].

TLRs are still a preferred choice for readout resonators due to their versatility, ability to be integrated with circuit elements that require on-chip flux biasing and drive lines and ability to achieve good mode isolation. However, an uninterrupted ground plane is necessary to prevent the introduction of unwanted odd modes. SiO_2 dielectric crossovers or on-chip transmission lines can be used to short the inductance presented by bond pads and maintain a continuous ground plane [23]. These considerations are important for the design and manufacture of TLRs in quantum computing, as they affect the efficiency and accuracy of qubit control and measurement. Overall, TLRs play a crucial role in the control and measurement of qubits in quantum computing.

4.2.1 Optimizing Resonator Functionality through Reflection Measurements and Data Fitting

When we look at the spectrum of transmission of a feedline, we see a Lorentzian drop for each TRL coupled by capacitance to the feedline. The resonant frequency of a resonator can greatly affect how it interacts with the feedline, causing the transmission to go down. This is seen in the shape of the line in the frequency spectrum, Fig. 4.5-top left. However, the Lorentzian exhibits an asymmetry. This asymmetry is often attributed to reflections in the feedline, which can be caused by impedance mismatches in the set-up [4].

The complex S_{21} scattering coefficient of a resonator capacitively coupled to a transmission line, Figs. 2.7 and 4.5, can be described by the following equation [75, 4]:

$$S_{21}^{notch}(f) = \underbrace{A \left(1 + \alpha \frac{f - f_0}{f_0} \right) e^{i(\phi_v \omega + \phi_0)}}_{\text{environment}} \underbrace{\left[1 - \frac{\left(\frac{Q_L}{|Q_{ext}|} \right) e^{i\theta}}{1 + 2iQ_L \left(\frac{f}{f_0} - 1 \right)} \right]}_{\text{ideal resonator}}. \quad (4.18)$$

Here, $Q_{ext} = |Q_{ext}| e^{-i\phi}$ is the extrinsic quality factor, related to the coupling quality factor by $1/Q_c = Re(1/Q_{ext})$ [75]. The parameter f_0 is the resonant frequency of the resonator. Finally, the environment term accounts for the influence of the environment, which includes factors such as the slope (α) in the background transmission surrounding the resonant frequency, the transmission amplitude away from resonance (A), and the propagation delays (ϕ_v and ϕ_0) associated with the path length of the cables for signals traveling to and from the sample.

To fit data, we use the least squares method in Python's *lmfit* library. This method is a statistical procedure that finds the best fit for a set of data points by minimizing the sum of the residuals between the points and the plotted curve, predicting this way the behavior of dependent variables. We often break down the 8-parameter fitting problem into several independent fitting problems to increase accuracy and robustness [35]. If further precision is needed, we can then run a refined 8-parameter fitting using the results from the step-by-step method as initial values.

To fit the data, we proceed with the following steps: first, determining the electrical delay (since the cable setup is the same for different chips, measuring the S_{21} phase over a large span of frequencies and playing with the electrical delay parameter in the VNA gives a good global approximate of 192.6 ns); then, we multiply the complex number array by $e^{i2\pi f\tau}$ where τ is the calculated delay. Next, we rotate the data and fit it to a simple Lorentzian to predict the frequency and width of the resonance with a high degree of accuracy also using least squares method. The Lorentzian model follows this equation

$$|S_{21}(f)| = F_{Lorentz}(f) = \frac{A}{\pi} \frac{\sigma}{(f - f_0)^2 + \sigma^2} + B, \quad (4.19)$$

where σ is the full width half maximum, f_0 here is the resonant frequency of the resonator, A is the amplitude (calculated as $A = height \cdot \sigma \cdot \pi$) and B is the offset of the Lorentzian function. Finally, we use this information as a hint or initial points for the least squares method to fit the data to the 8 parameter fitting function in (4.18), resulting in the fitted parameters shown in Fig. 4.5.

In conclusion, by using a notch-type geometry and the least squares method, we are able to fit data and determine the fitted parameters for the resonator with a high degree of accuracy in less than 5 seconds. The obtained fitted parameters provide valuable information about the performance of the resonator and can be used to optimize its design and functionality.

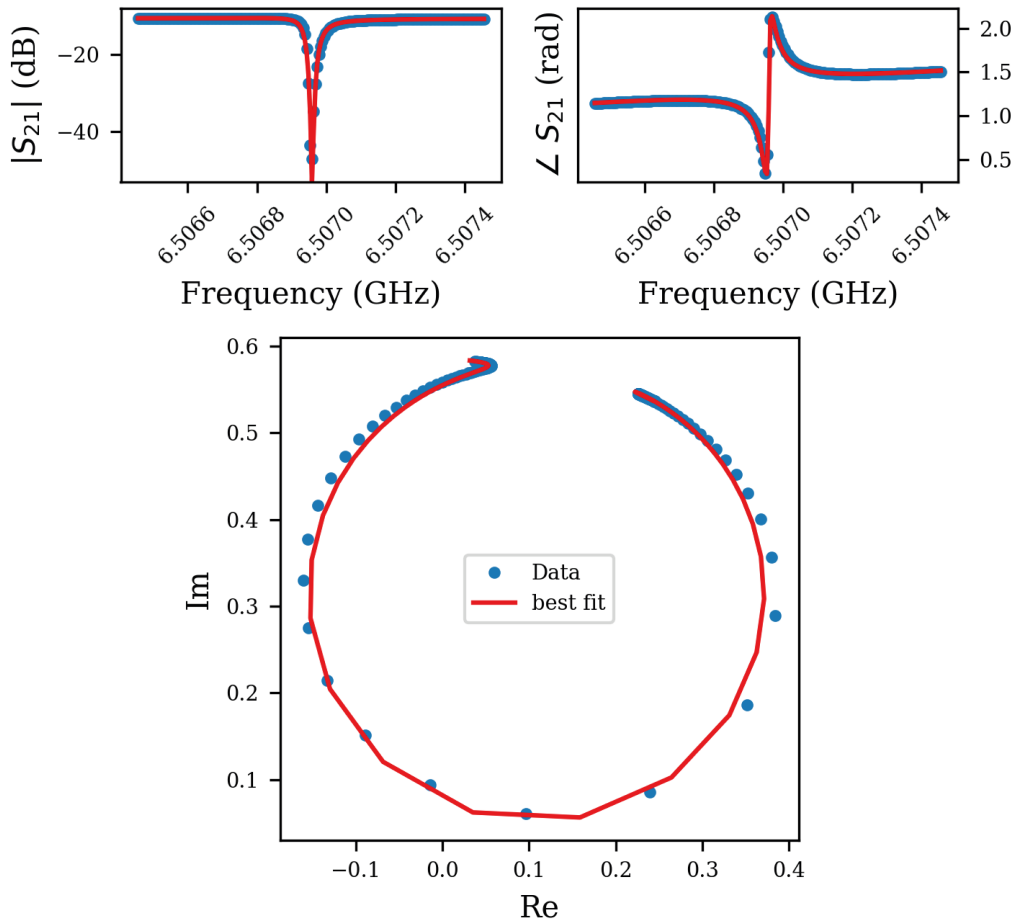


Figure 4.5: Measured data points (blue) vs fitted function to the data (red) shown in magnitude (top left), phase (top right) and complex plane (bottom). The fitted parameters for this resonator, as determined by the least squares method with 400 data points and a model of 8 variables (4.18), are: f_0 : 6.5070 GHz, BW: 0.0417 MHz, Q_L : 155921, Q_i : 1382967, Q_e : 175734, θ : 0.1219, A : 0.5877, α : 0, ϕ_v : 0, ϕ_0 : 1545ns. The fit statistics for this data show that the model was able to fit the data with 232 evaluations in a time of 5 seconds.

Chapter 5

Data Analysis and Findings

In this chapter, we present the results of our data analysis and findings on the characterization and performance of a single qubit in a quantum computing system. This system has been built full stack using the tools and subsystems explained in previous chapters: 3D transmon design (Section 4.1), wiring and control electronics (Sections 3.1 and 3.3), software of control and measurement (Section 3.2) and quantum concepts and procedures to measure and benchmark superconducting qubits (Chapter 2). In addition to the usual qubit performance indicators of decay time (T_1) and readout fidelity, we also include measurements of high-quality factor resonators at low temperature.

All of these are first steps towards a multi-qubit chip like the one shown in Fig. 4.4. The procedures to characterize the qubits either through a TLR or a cavity resonator are the same and the tools developed in this work are used to characterize and calibrate multi-qubit QPUs.

Additionally, a benchmark about the utility of Surface Acoustic Wave filters as Purcell Filters is done.

5.1 Characterizing a Qubit: Punchout and Two-Tone Spectroscopy

In the first part of our analysis, we focus on characterizing the qubit through the readout resonator (in this case the cavity of Fig. 4.1). To achieve this, we measure the frequency transmission spectrum of the resonator at various power levels, a technique known as "punchout measurement". By observing the non-linearity of the coupling of the resonator to the qubit, we are able to extract the dressed frequency of the resonator (2.28) in the qubit's state $|0\rangle$, denoted as $\tilde{f}_{r|0\rangle}$. At a critical photon number (2.32), n_c , of approximately -115 dBm, we observe a shift, Fig 5.1 corresponding to high power frequency dispersive shift (2.27) of -850 kHz. This frequency shift from high power indicates the dressed frequency of the resonator in the $|0\rangle$ state of the qubit (when the system is in its ground state, which we measure to be $\tilde{f}_{r|0\rangle} = 7.3373$ GHz. This measurement is done usually at the beginning to find the resonances of the resonators affected by the qubits. After that, if we measure the same qubit with same setup the frequency and power needed are always the same¹. We choose n_c power level as optimum since at higher powers there is still no shift and at lower powers the SNR is worse.

¹Except if the JJ gets oxidized because exposure to the environment or something like that happens that can make the frequency of the qubit to change and thus the frequency of the resonator at low power to also change slightly.

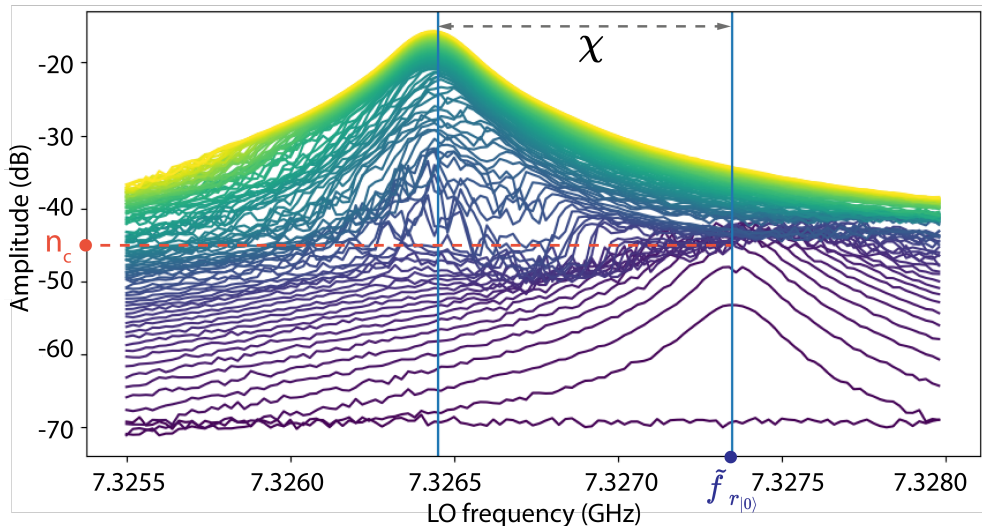


Figure 5.1: Punchout measurement showing the shift in the frequency of the cavity, f_r , dependent on readout “amplitude” ranging from -10 to -70 dB. These amplitude dB show the difference between input and output of the AWG to the ADC for readout shown in Fig. 3.1, with the only difference that we have added an step attenuator after the combiner. The amount of power arriving to the sample (the cavity resonator) ranges from -80 to -140 dbm. This is because the fixed power at the AWG is chosen to be -10 dBm in this experiment and the fixed attenuation in the setup, similar to Fig. 3.9, is chosen to be 60 dB. Then, n_c corresponds to -115 dBm at the sample. The frequency shown is the LO for readout (yellow in Fig. 3.1) but the frequency seen at the sample is LO+IF and the IF is fixed to be 100 MHz, this means that the actual frequencies probed range from 7.3355 to 7.3380 GHz and thus the resonator being at 7.7373 GHz for low power (below n_c) and low temperature (below 30 mK). This measurement shows that the cavity resonator is shifted 850 kHz when critical photon number is reached.

From the measured data, we can deduce the frequency of the qubit. Comparing the frequency of the high-power resonance, f_r ,

with that of the low-power resonance, $\tilde{f}_{r_{|0\rangle}}$, allows us to determine whether the qubit frequency is lower than that of the resonator [66]. We can even estimate the approximate value of the qubit frequency, which helps us narrow down the range of frequencies to scan. However, this estimation requires assuming certain design parameters such as g , Δ , and E_C , and due to manufacturing uncertainties, these parameters may vary. The estimation is based on the measured χ [9]

$$\chi = -\frac{g^2 E_C / \hbar}{\Delta (\Delta - E_C / \hbar)}. \quad (5.1)$$

In this specific case, we expected to find the qubit at approximately 5.5 GHz. However, the actual measurement (Fig. 5.2) reveals that it is located around 3.5 GHz, indicating a possible discrepancy in the value of E_C , which might be higher than initially anticipated. Additionally, we can determine the coupling strength (g) between the resonator and qubit by observing the size of the shift in the resonator. A larger shift signifies a stronger coupling between the two entities [66].

Measuring the resonance frequency of a qubit is a crucial step in characterizing a quantum computing system. One method commonly used for this is known as two-tone continuous-wave spectroscopy, in which we continuously measure the transmission (S_{21}) at $\tilde{f}_{r_{|0\rangle}}$ while applying a second continuous wave drive at frequency f_d . When this second tone is close to the resonance frequency of the qubit, f_q , the qubit is excited and transitions from state $|0\rangle$ to state $|1\rangle$. This causes a qubit excitation and thus a shift in the resonator's frequency to $\tilde{f}_{r_{|1\rangle}}$, which we can observe as a change in transmission (magnitude and phase) at $\tilde{f}_{r_{|0\rangle}}$.

However, finding the correct power level for the spectroscopy tone can be challenging. If the power is too low, the qubit may not be excited even if the drive frequency is close to its resonance, resulting in no shift being observed. On the other hand, if too much power is applied, the linewidth of the resonance will increase due to power broadening, eventually making the peak indistinguishable from the

background [36, 80, 81]. To address this challenge, we can repeat the spectroscopy experiment for different power levels until the resonance shows the highest SNR.

From the measurement shown in Fig. 5.2, we are able to determine the qubit’s resonance frequency at $f_q=3.549$ GHz, and the frequency difference between the qubit and resonator being then $\Delta = 7.33645 - 3.661 = 3.67545$ GHz. This value of Δ was expected it to be around 2.5 GHz, as calculated in Section 4.1. However, the frequency of the qubit was found to be lower than expected due to fabrication uncertainties of the junction area.

Overall, the measurements shown in this section provide important information about the behavior and performance of the qubit and resonator system. By understanding the resonance frequency of the qubit and the coupling between the qubit and resonator, we are able to optimize the system for efficient quantum computing operations.

5.2 Unveiling Quantum Control: Optimizing Gates in Transmon Qubits

In this section, we investigate the behavior of a qubit as it oscillates between the $|0\rangle$ and $|1\rangle$ states in response to an external “impulse”. This effect is typically achieved by applying a pulse at f_q , either with a fixed amplitude and a varying duration (τ), or vice versa [91].

To determine an optimal π -pulse, we must balance two main considerations: On one hand, we aim to minimize pulse duration in order to achieve fast control over the qubit state. On the other hand, we must also consider the fact that transmon qubits are anharmonic oscillators with more than two discrete energy levels, rather than the idealized two-level systems described by the Rabi model. These higher energy levels, although detuned from the first transition frequency, can affect the effectiveness of the π -pulse if not properly

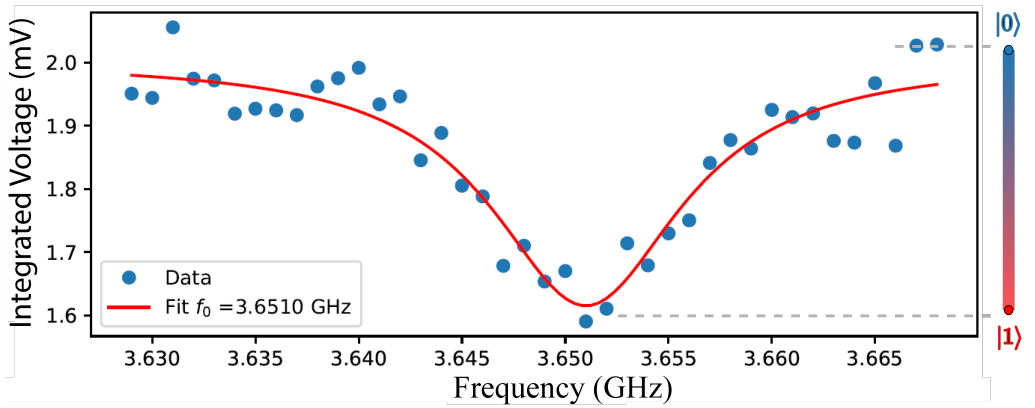


Figure 5.2: Qubit spectroscopy experiment measurement. Showing measured data points (blue) and fitted Lorentian function (4.19) (red). The qubit frequency, f_q , is found at the frequency where the integrated voltage is minimum, that means that the frequency of the resonator has completely shifted from $\tilde{f}_{r|0\rangle}$ to $\tilde{f}_{r|1\rangle}$ as was illustrated in Fig. 2.7.

accounted for, potentially leading to leakage out of the lowest two energy levels. As a result, the pulse duration must be chosen carefully to avoid overlap with the frequencies of these higher transitions. For a typical anharmonicity of $\alpha/2\pi \approx -200$ MHz, a good choice for the pulse duration may be a Gaussian pulse with a standard deviation of 4-6 ns and a total duration of approximately $4\sigma \approx 20$ ns. This ensures having a narrow Gaussian pulse in frequency² and not excite the qubit by having signal in frequencies for other levels different than the $E_{01} = \hbar 2\pi f_q$ (2.11).

The RX gate represents a rotation in the X-axis of the Bloch sphere, with the rotation angle (θ) depending on the amplitude (A) and duration (τ) of the pulse.

To understand the behavior of the qubit under these pulses, we sweep A and τ and plot the resulting oscillations in a colormap plot, as shown in Fig. 5.3a. A 2D cut of this plot, shown in Fig. 5.3b, reveals the Rabi oscillations of the qubit, which range from $V_{|0\rangle} \approx 4.5$ mV to $V_{|1\rangle} \approx 2.5$ mV. The voltages $V_{|0\rangle}$ and $V_{|1\rangle}$ represent the integrated voltage of the digitized signal measured from the resonator³ transmission at a single frequency $\tilde{f}_{r_{|0\rangle}}$, when the qubit is in the $|0\rangle$ and $|1\rangle$ states, respectively. To extract the key values from our Rabi experiment measurements, we use a fit based on a typical damped cosine function, Fig. 5.3a

$$P_{|0\rangle}(t) = A \cos(2\pi f t + \phi) e^{-t/T_R} + B. \quad (5.2)$$

Here, A represents the amplitude of the cosine, f is the oscillating frequency, ϕ is the phase-shift, B is the offset, and T_R is the decay of the Rabi.

We can determine the exact pulse duration (τ_π) required to perform a π -pulse. For example, if we know that a pulse of duration $\tau_\pi =$

²The Fourier transform of a Gaussian pulse is a Gaussian pulse. If we instead used a square pulse in time domain we would have a sinc in frequency domain and thus, some signal at the secondary lobes close to the excitation frequencies of the other qubit levels.

³In this case the rectangular cavity resonator.

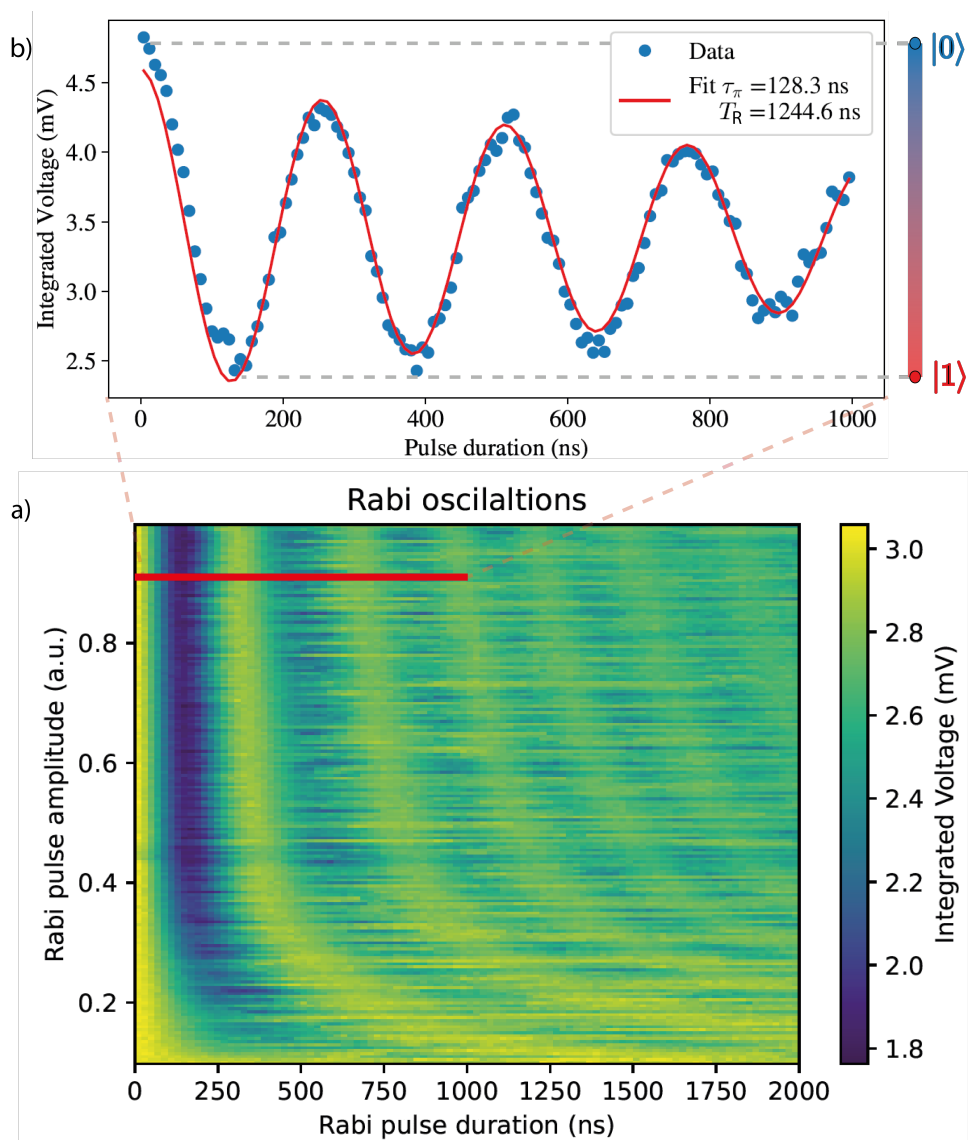


Figure 5.3: (a) Rabi oscillations measurement with variation of the pulse duration, τ , repeated for different pulse amplitude, A . (b) Rabi oscillations 2D cut (red line) from (a) for $A=0.9$. Blue dots represent the measured data and in red the fitted data with an exponentially decayed cosine function (5.2).

110ns at $A = 0.9[\text{a.u.}]$ will excite the qubit to the $|1\rangle$ state when sent at the qubit frequency f_q , we can use this information to optimize our pulse shape and duration for performing π -pulses. These π -pulses are also called X-gates and are the equivalent to the classical NAND gates.

How is it possible that we observe intermediate points between the $|0\rangle$ and $|1\rangle$ states, given that quantum states "collapse" to the voltages $V_{|0\rangle}$ and $V_{|1\rangle}$ respectively when measured? The observed intermediate points are outcomes of statistical averaging, a crucial step to mitigate noise and achieve a high signal-to-noise ratio (SNR). During a single measurement, the quantum state collapses to either the $|0\rangle$ or $|1\rangle$ state, with probabilities influenced by the qubit's polarization and readout fidelity. The potential inaccuracies in the counts obtained are primarily due to the readout fidelity. To estimate this polarization accurately, the qubit must be prepared in the same state and the experiment repeated multiple times, accounting for the influence of readout fidelity on the observed outcomes. For example, if the initial state of the qubit is $|\psi\rangle = |0\rangle$ and we apply a $\frac{\pi}{2}$ -pulse

$$|\psi\rangle \longrightarrow \boxed{X_{\pi/2}} \longrightarrow \boxed{\text{Measurement}} = m$$

the quantum state will be placed at the equator of the Bloch sphere (state $|\phi\rangle$) and will collapse to either $V_{|0\rangle}$ or $V_{|1\rangle}$ when measured with a 50% probability. This process is similar to flipping a coin: any single flip will yield heads or tails, but the probability of obtaining heads or tails can be estimated by flipping the coin many times and taking the ensemble average.

In the case of the data points in Fig. 5.3b, they are the result of averaging the results of this sequence

$$|\psi\rangle \longrightarrow \boxed{RX} \longrightarrow \boxed{\text{Measurement}} = m$$

repeated over 1024 times. So, each pixel is the result of the average of 1024 measurements.

In the case of our qubit measurements we can use this statistical averaging process to improve the accuracy and precision of our results. By collecting a large number of data points and taking the average, we can reduce the impact of any random fluctuations or noise

in the system, allowing us to make more reliable conclusions about the behavior of the qubit, at the cost of longer acquisition times..

In summary, the characterization of a response of the qubit to pulses is an important step in the optimization of quantum gates and the development of high-fidelity quantum circuits. By carefully considering the pulse duration and shape, as well as the specific properties of the qubit, it is possible to achieve accurate and efficient control over the state of the qubit. Statistical averaging techniques, such as repeating an experiment many times and taking the average of the results, can be used to improve the accuracy and precision of our measurements and make more reliable conclusions about the behavior of the qubit.

Decay time measurement, T_1 The decay time, also known as the life-time or relaxation time, can be measured using the following quantum circuit:

$$|\psi\rangle \text{ --- } \boxed{X_\pi} \text{ --- } \overset{t}{\text{---}} \boxed{\text{meter}} = m$$

To measure T_1 , we first apply a π -pulse to excite the qubit, X_π . After a controlled delay of time (t), we measure the state of the qubit. For $t \approx 0$ ns, the measured state (m) will be, with high probability, $V_{|1\rangle}$, while for $t \gg T_1$, the measured state (m) will be, with high probability, $V_{|0\rangle}$, because the qubit naturally decays and will eventually end up in the ground state. By averaging the results of many measurements, we can determine the population probability of the excited state as a function of time, as shown in Fig. 5.4.

We can see from the data that T_1 exhibits an exponential decay, as expected from the mixed state density matrix 2.20. To fit the measurement data, we can use a typical exponential decay function of the form:

$$V(t) = A \cdot e^{-t/T_1} + B, \quad (5.3)$$

where A and B are scaling and offset factors, respectively. By fitting our data to model and assuming qubit exponential decay (5.3),

we can accurately determine the value of T_1 and gain a better understanding of the relaxation behavior of the qubit. This information is important for optimizing the performance of quantum gates and developing high-fidelity quantum circuits. From this measurement we know that the decay time, T_1 , of the our qubit is $11.4 \mu s$.

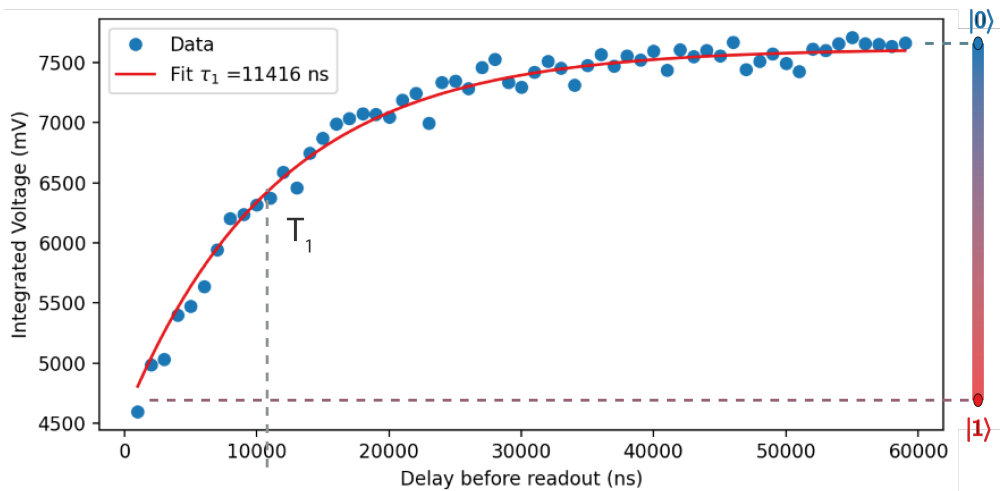


Figure 5.4: Decay time measurement, T_1 , blue dots are the measured data and red line is the fitted function (5.3) to the data.

Fidelity measurement, F When measuring the state of a qubit, the outcome is subject to noise from both quantum fluctuations and electronic components in the readout system. This noise results in time-dependent fluctuations of the measured signal, leading to uncertainty in the demodulated signals. To mitigate this uncertainty, we can integrate the noisy signal over time to obtain a single value, which will follow a Gaussian distribution in the (I, Q)-plane. By comparing the widths of the Gaussian distributions surrounding the mean with the peak separation in the (I, Q)-plane, we can define a signal-to-noise ratio (SNR) to quantify the noise. A good readout should have an SNR much larger than 1 [36].

To measure the $|0\rangle$ and $|1\rangle$ states of the qubit, we repeat the measurement process of Fig. 3.6 by preparing the qubit at $|0\rangle$ state and measuring using the following circuit

$$|\psi\rangle \text{ --- } \boxed{\text{---}} \text{---} \boxed{\text{---}} = m$$

around 8000 times (using our setup) for the gaussian at $|0\rangle$ and repeat the process preparing the qubit at the $|1\rangle$ state using the following circuit

$$|\psi\rangle \text{ --- } \boxed{X} \text{---} \boxed{\text{---}} = m$$

the same amount of 8000 times. The results of this measurement are shown in Fig. (5.5)a.

The SNR can be calculated using the formula [54]

$$SNR = \frac{\delta\theta}{(\Delta\theta_1 + \Delta\theta_0)}, \quad (5.4)$$

where $\delta\theta$ represents the difference between the two states, $\Delta\theta_0$ and $\Delta\theta_1$ represent the noise (2σ) of each distribution, and, ideally, $\delta\theta$ should be equal to 2χ , the dispersive shift.

In addition to the SNR, it is important to consider the fidelity of the measurement, which is a measure of the probability that the qubit state can be accurately assigned based on the measurement outcome. The fidelity is calculated using the formula [54]:

$$\mathcal{F} = 1 - \frac{[P(m=0|1\rangle_i) + P(m=1|0\rangle_i)]}{2}, \quad (5.5)$$

where $|0\rangle$ ($|1\rangle$) mark the state preparation without (with) a π -pulse, and $m=0(1)$ stands for the qubit being assigned to the ground (excited) state. Thus, $P(m=0|1\rangle_i)$ meaning the probability of measuring $m=0$ when the qubit is prepared in the state $|1\rangle$. To ensure a high fidelity, it is important to minimize both the separation error between the two state distributions and any additional errors that may arise due to relaxation of the qubit during the readout process. To achieve this goal, the readout cycle should be completed on a timescale much shorter than the qubit relaxation time.

In general, a good readout system should have both a high SNR and high fidelity to ensure accurate and reliable measurement of the qubit state. By carefully optimizing the readout process and minimizing noise, we can achieve high-fidelity quantum circuits with improved performance.

To optimize the readout process and minimize noise, we aim for a readout system with both a high SNR and high fidelity. By maximizing the fidelity, \mathcal{F} , through signal processing optimization, we can improve the performance of our high-fidelity quantum circuits.

The measured fidelity, \mathcal{F} , obtained from single-shot measurements (no averaging) is around 68%, as shown in Fig. 5.5 and calculated using a fitting procedure and (5.5). The fidelity is maximized by optimizing the readout power and frequency for a given readout pulse length [42].

It is important to note that the measurement of the qubit state is not the only factor that affects the fidelity of a quantum circuit. Other factors, such as the accuracy of quantum gates and the decoherence of the qubit, can also impact the overall performance of the circuit. By carefully optimizing all aspects of the quantum system, we can achieve high-fidelity circuits with improved performance and accuracy. We expect major improvement of the readout fidelity with the use of a TWPA [65]. Probably up to the 90% or more.

In summary, the characterization and optimization of pulse spectroscopy techniques play a crucial role in the development of high-fidelity quantum circuits. By carefully measuring the relaxation dynamics and noise properties of transmon qubits, we can optimize the control and performance of quantum gates, leading to improved performance and accuracy of quantum circuits.

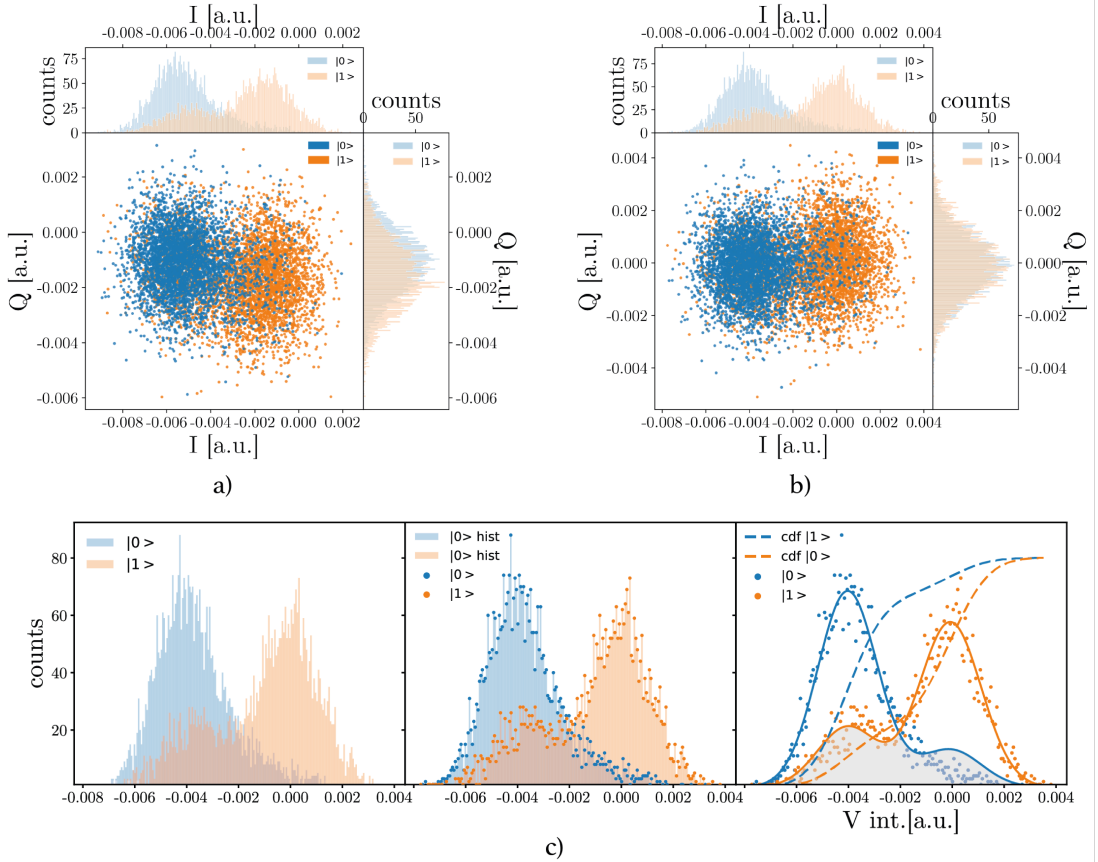


Figure 5.5: (a) Distributions corresponding to 8000 single shot measurements with the qubit prepared in the $|0\rangle$ state (blue) and in the $|1\rangle$ state (orange) before measurement at $f_{r|0\rangle}$. Top (right) shows a histogram in I (Q). (b) Distributions rotated to maximize their separation in the rotated I -axis. (c) Double-gaussian fit of rotated histogram in I . Grey area show the overlap of both distributions. The assignment fidelity is calculated as the maximum difference in the cumulative distribution functions (dashed lines) of the excited and ground histograms.

5.3 Precision Measurements of High-Q Aluminum Resonators at 10 mK

As a final validation of the full microwave packaging developed, we designed, manufactured and wirebonded to the PCB a silicon chip containing an aluminum coplanar transmission line with five aluminum coplanar resonators capacitively coupled to the transmission line. The microwave package containing the wirebonded chip is placed inside the dilution refrigerator and cooled down to 10mK. At that temperature we measure the transmission line, finding dips corresponding to the resonance frequencies of the resonators. The complex data obtained from the resonator responses is postprocessed and fitted using the procedures outlined in section (4.2.1)[63] to determine the internal quality factor of each resonator. The measurements shown in Fig. 5.6 show high internal quality factor of resonators for different powers reaching more than 1 million for high-level powers of -10 dBm at the VNA, corresponding to around -70 dB at the resonator (assuming 50 dB attenuation of the attenuators of the setup, Fig. 3.9, and 10 dB of cable attenuation). At very low powers, two-level system effects reduce the quality factor as observed in Fig. 5.6. These results show no apparent problems with the built package presented in 3.3. In the appearance of any spurious or hybridized mode in the operational frequencies we would observe a reduction of the quality factor of orders of magnitude which is not observed.

Proper shielding, matching and thermalization is demonstrated by measuring aluminum high- Q_i resonators chip at 10mK.

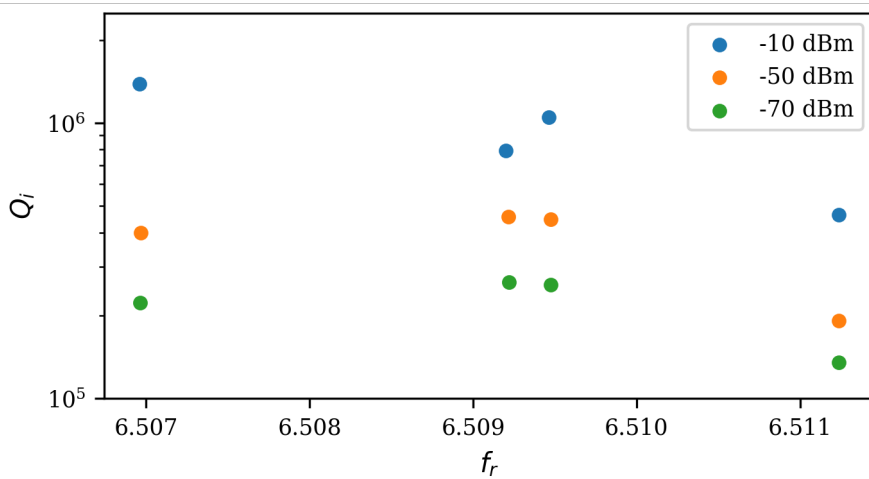


Figure 5.6: TLR aluminum coplanar resonators internal quality factor extracted from fitting measurement data of transmission line containing the resonators capacitively coupled to it. Measurement is repeated for different powers of the VNA; -10 dBm , -50 dBm and -70 dBm (around -70 dBm, -120 dBm and -140 dBm signal power at the resonator).

5.4 Purcell Filters for Quantum Computing: Exploring the use of SAW Filters

Purcell filters play a pivotal role in shielding qubits from external noise, leading to enhanced coherence times and improved precision in quantum computations (as already introduced in Section (2.5)). The use of multiple poles in Purcell filters is a relatively rare but potentially promising approach. These multi-pole filters offer several advantageous features, including a wider and more consistent bandwidth, increased rejection in the stopband, and a sharper transition from the bandpass to the stopband. Such benefits open up the possibility of placing qubits in closer proximity to the resonators, contributing to the advancement of quantum computing technology.

This section presents a comprehensive investigation into the effectiveness and efficiency of Purcell filters using Surface Acoustic Wave (SAW) technology. The primary objective is to provide valuable insights for researchers seeking to optimize their quantum computing systems by understanding the potential advantages and limitations of employing multi-pole SAW filters.

In the telecommunications industry, multi-pole filters with a generalized Chebyshev response are widely used. These filters are implemented using coaxial resonators in telecommunications towers [28] or acoustic resonators for low-power and miniaturized applications like smartphones to put some examples. The generalized Chebyshev response offers benefits over other multipole responses, such as a steeper transition band and higher stopband with the use of lower orders thanks to allowing to tune the position of the transmission zeros.

Regardless of the technology used for implementation, the design of the response and coupling matrices follows a general procedure. If acoustic resonators are chosen, the classical design approach involves arranging series and shunt resonators using a successful pole-zero ap-

proach. This results in a ladder filter that electrically connects series and shunt resonators with carefully chosen frequencies to achieve a desired bandpass response. Typically, the series resonators have identical frequencies to each other, as do the shunt (parallel) resonators [90, 50].

Acoustic filters can be implemented using either Bulk Acoustic Wave (BAW) resonators, the wave propagates through the thickness of the resonator material, or Surface Acoustic Wave (SAW) resonators, the wave propagates along the surface of the resonator material.

SAW resonators consist of reflector gratings defining an acoustic cavity, and an Inter Digital Transducer (IDT), Fig. 5.7, that converts electrical signals into acoustic signals and vice versa. The slow propagation velocity of acoustic waves allows for high levels of miniaturization in devices [50].

The relationship in (2.34) can be further developed so that T_1 can be expressed as function of the scattering parameters of the filter [17]

$$T_1 = \underbrace{\kappa^{-1} \left(\frac{\Delta}{g} \right)^2}_{\text{Bare Purcell limit}} \underbrace{\frac{\text{Re} \{Z_{ext}(\omega_r)\}}{\text{Re} \{Z_{ext}(\omega_q)\}}}_{\text{Purcell filter}}. \quad (5.6)$$

Where the environmental impedance, Z_{ext} , can be extracted from calibrated measurements, i.e. of the filter, by

$$\text{Re} \{Z_{ext}\} = Z_0 \frac{1 - |S_{11}|^2}{|1 - S_{11}|^2}. \quad (5.7)$$

The state of the art of thin film SAW filters allow filter's central frequencies from few MHz up to a typical maximum of 2.5 GHz [90, 1]. The resonant frequency of IDT is pitch defined by

$$f_r = \frac{v_p}{\lambda}, \quad (5.8)$$

where v_p is the phase velocity of a certain wavemode in the piezoelectric and λ is the wavelength that defines the pitch, Fig. 5.7. For the

1.5 GHz thin film SAW resonator measured, Fig. 5.7, the IDT fingers are $0.58 \times 60 \mu m$ and the gap between them is about $0.87 \mu m$. However, to design a thin film SAW resonator at 7 GHz with the same material stack and mode, the IDT finger size would be in the ballpark of $0.16 \times 60 \mu m$ with a similar gap. At those higher than ~ 3 GHz frequencies the fingers of the IDT are so thin and close together that our cleanroom processes make it challenging to manufacture. Therefore, in order to make IDT excited acoustic resonators it's possible to add an air layer below the thin film piezoelectric so that the wave is propagated through the thickness of the resonator and not along the surface. Those kind of resonators are called XBAR (laterally excited Bulk Acoustic Resonators) and their resonant frequency is not pitch defined.

Typical transmon qubits frequencies of control are in the order of ~ 4.5 to ~ 6.5 GHz and the readout resonators are around ~ 7 to ~ 8 GHz. However, flux qubits operate around ~ 1.5 to 3 GHz while maintaining the readout resonators at the same 7-8 GHz range to keep a low thermal noise. We calculate the theoretical improvement on T_1 that using a commercial Wifi 6E band BAW filter would make by using (5.6) and plotting the results over frequency compared to the bare Purcel limit (without any filter) in Fig. 5.8. To perform these calculations we have assumed $g/h = 100$ MHz and a readout resonator at 6.6 GHz with $\kappa/2\pi = 50$ MHz.

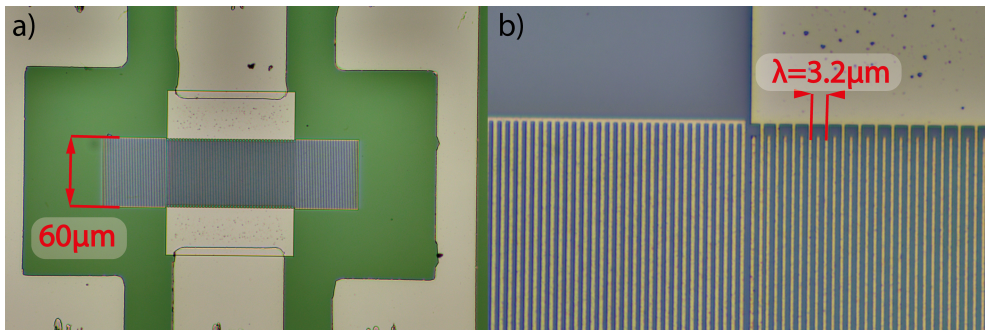


Figure 5.7: (a) Thin Film SAW resonator top view. Green is the Lithium Niobate, the yellowish is the aluminum on top of it. In the middle the IDT can be observed. (b) Zoom of the top left corner of the IDT in (a) showing the IDT detail and left grating.

Fig. 5.8 shows two order of magnitude improvement in T_1 . However, ladder-type filters present a pair of transmission zeros or notches which somehow define the bandpass in its transmission response. The presence of the transmission zeros means that this topology offers a very good selectivity, but also a poor out-of-band rejection. Out of the resonant frequencies, the BAW resonator behaves as a pure capacitor, and the out-of-band rejection is thus given by the natural capacitor divider, making rejection decrease slowly as frequency moves away from central frequency of the filter. Taking this into account, it is straightforward to state that improving the out-of-band rejection, initially entails increasing the order of the filter, thus, the area [90].

In [17] the theoretically greater improvement in T_1 comes at assuming $R_s = R_0 = 0$ at cryogenic temperatures for the BAW resonators. However, will kinetic inductance, Two Level System losses and other effects manifest at the measurement environment conditions for qubits in acoustic resonators? Will those conditions have an effect on the acoustic resonator response?

We measure one Thin Film SAW resonator manufactured and characterized in [41] at measurement environment conditions of the

qubit. This resonator is designed to have good results on the Shear Horizontal (SH0) mode and is manufactured using 30°YX-cut LNOI (Lithium Niobate on insulator) wafer structure. The resonator is designed to have the resonant frequency to be around 1.5GHz. This is done by adjusting the pitch of the IDT to be a wavelength of the operational frequency at the propagation velocity of the acoustic wave in the LNOI piezoelectric. Furthermore, the SiO layer is designed to have a thickness of $\lambda/4$ at 1.5 GHz in SiO so it provides isolation from the substrate to shear waves propagating towards the silicon in the vertical direction.

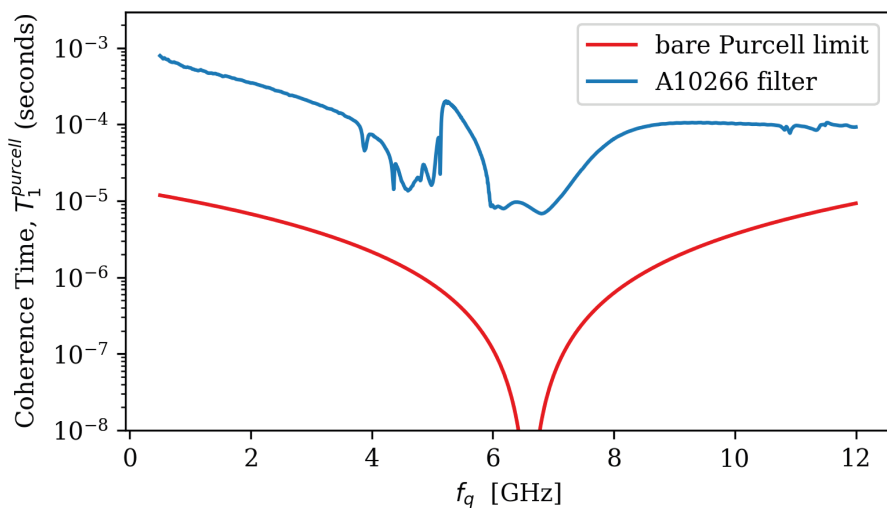


Figure 5.8: (a) Theoretical T_1 improvement due to using commercial A10266 Acoustic filter for WiFi-6E band (blue) (5.6) vs the bare Purcell limit (2.25)(red).

Measurement environment conditions of the qubit means to measure at temperatures around 30 mK with powers around -120 dBm. First, we attach the resonator die to the PCB and microwave housing (explained over section (3.3)) and check the parameters with a controlled setup at room temperature.

We measure a resonance at 1.45169 GHz and an antiresonance at 1.46519 GHz.

From these values we can also extract the electromechanical efficiency

$$k_{eff}^2 = \frac{\pi^2}{4} \frac{f_a - f_r}{f_a}, \quad (5.9)$$

where f_a is the antiresonance and f_r is the resonance of the resonator. In this case, k_{eff} is around 15%, which matches what was measured by [41]. We also obtain the quality factor of the resonator [32]

$$Q(\omega) = \frac{2\pi f \tau |S_{11}|}{1 - |S_{11}|^2} \quad (5.10)$$

where $\tau = -\frac{\delta(\angle S_{11})}{2\pi\delta f}$ is the group delay. We seem to obtain worse impedance ratio and half the quality factor (Q), Fig. 5.9, but that is probably because we are measuring with uncalibrated SMA to SMP adaptors, uncalibrated PCB trace and uncalibrated 2 mm wedge-bonds to the sample instead of directly with calibrated probe station, as in [41].

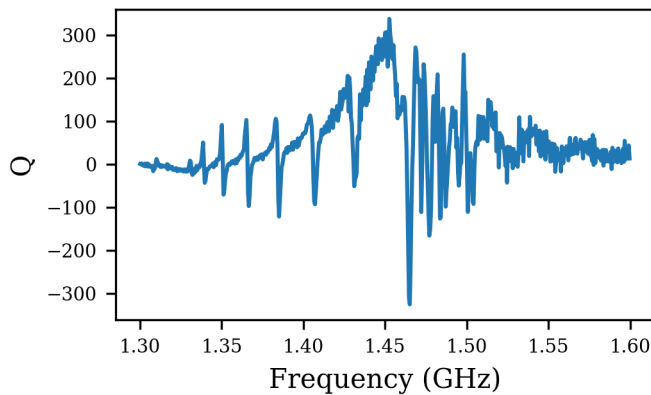


Figure 5.9: Quality factor of the resonator obtained from (5.10) and S_{11} measurement at room temperature.

We use the Qinu Sinludi XL dilution refrigerator to cooldown the sample down to 30 mK, Fig. 3.9. The input port comes from port 1 of the VNA and the output port goes to port 2 of the VNA. Usually, a circulator is used after the Device Under Test (DUT) to avoid effects from the noise generated by the 4 K stage LNA. Because we don't have a circulator for the operating frequencies, we have used a 6 dB attenuator to compromise noise vs signal level attenuation. To be more accurate we can calculate the exact number of photons per second, and thus, the number of dB we need to attenuate from the LNA [86]

$$N_{IL} = \frac{1}{2} \coth \left(\frac{hf}{2k_b T_{IL}} \right) (A_{IL} - 1), \quad (5.11)$$

where T_{IL} is the physical temperature of the LNA, k_b is the Boltzman constant, h is the Planck's constant, $A_{IL} = 1 + T_{NIL}/T_{IL}$ is the insertion loss factor, f is the frequency of the readout and T_{NIL} is the added noise by the LNA. In this case, $f \sim 1.5$ GHz. Then, the total attenuation to compensate the 3 K added from the LNA should be 16 dB. However, with such attenuation before the first LNA measurements would be too noisy.

We perform a transmission measurement each 5 minutes during cooldown, Fig. 5.10.

We observe several findings in Fig. 5.10; We can identify the dip. Corresponding to the resonator resonance frequency f_r , and peak. Corresponding to the resonator antiresonance frequency f_a , of each $|S_{21}|$ trace⁴. Typical on any acoustic resonator, we can see that as temperature gets lower, losses get lower until reaching almost no losses below 1K due to Aluminum becoming superconductor. Finally,

⁴As seen in [41], a SAW resonator measured in series in a calibrated high frequency probe station shows a low impedance at the resonant frequency. This implies that when measuring transmission we would have to observe transmission at the resonant frequency and not a dip but a peak in $|S_{21}|$. This change might have been caused due to the huge inductance added to the setup. Since the measurements are done with the calibration plane outside the cryostat and we add meters of cable as well as attenuators and amplifiers that are not calibrated.

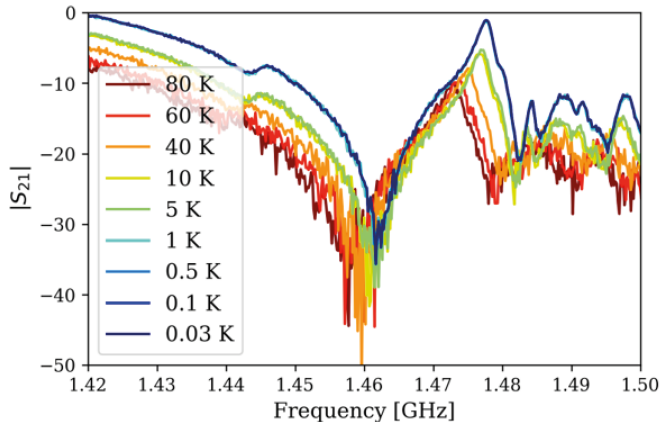


Figure 5.10: Measured transmission response of our Lithium Niobate (LiNbO) Thin Film SAW resonator for 9 significant temperatures.

we also observe a shift of the trace in frequency with temperature. We post-process the data and get the value of f_r and f_a at lowest temperature, 30 mK, and subtract it from the f_r and f_a of other temperatures such that we are left with the shift in frequency respect to that low temperature measurement over all the measured temperatures. This frequency shift is plotted in Fig. 5.11a for the resonance (blue) and antiresonance (orange) over a temperature sweep from 80 K to 30 mK. We found that the resonance and antiresonance shifts up to ~ 5 MHz from 80 K to around 30 mK.

Since f_r and f_a have almost the same shift in temperature, the electromechanical coefficient is maintained constant over temperature as seen in Fig. 5.11b. Therefore, over the temperature range used, the resonant frequencies are shifting but the electromechanical coefficient (5.9) is maintained constant.

Once at 30 mK, we perform a power shift with the VNA from -5 to -70 dBm. The power that arrives to the sample input after the attenuators, is between -60 and -130 dBm corresponding to typical single photon levels. The resonance and antiresonance are constant

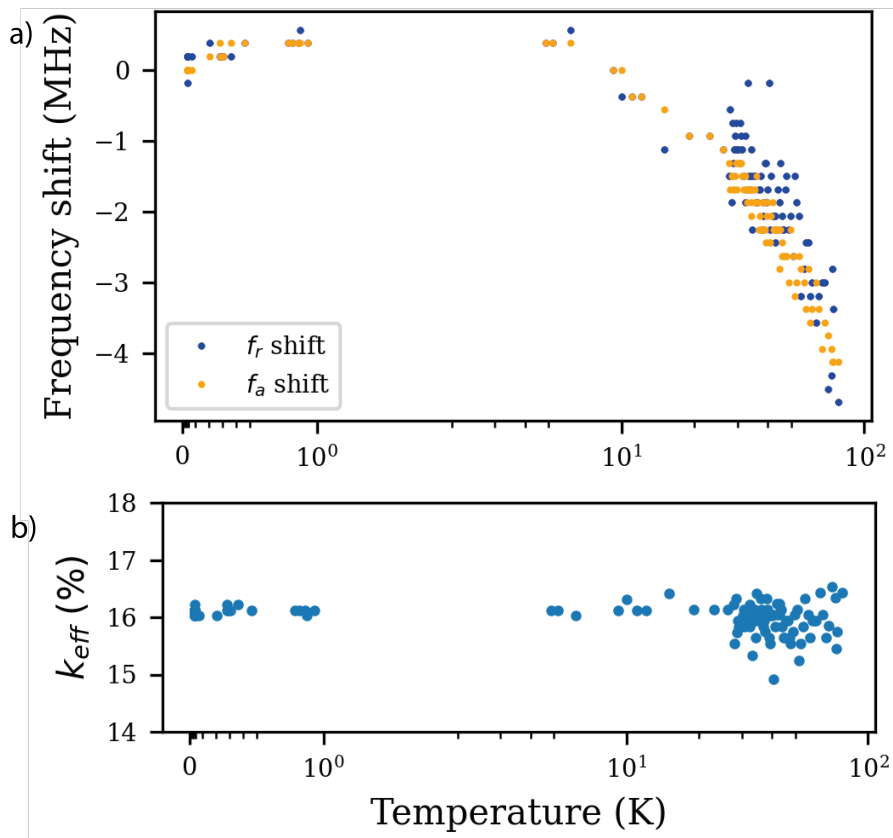


Figure 5.11: (a) Antiresonance (orange), f_a , and resonance (blue), f_r , shift over temperature sweep from 80 K to 30 mK. (b) Electromechanical coefficient, k_{eff} , over temperature, extracted from (a) using (5.9).

and no shift is observed due to the power sweep.

Although the cause of this frequency shift with temperature is yet to be determined, it could be attributed to changing permittivity of the materials over temperature or the kinetic inductance of the aluminum coming into play.

In this section, we have explored the potential and challenges of using acoustic resonators as Purcell filters for superconducting qubit processors. We have compared the performance and characteristics of commercial SAW and BAW filters and evaluated their suitability for this application. Our main findings are:

- Prototypes developed in our group for bandpass or lowpass filters using thin film SAW resonators at 1.5 GHz could be used as filters for flux lines. The possibility of using them as stopband filters for readout was studied but discarded since the observed simulated losses at the out of band higher frequencies, Fig. (5.12).
- XBAR filters are more suitable as Purcell filters, because they have a high bandwidth, a low insertion loss a small frequency shift over temperature and higher operating frequencies in the band of interest (5-8 GHz). Moreover, in comparison with the common implementation of the lossy TLR feedline as Purcell filter, XBAR filters would provide a flat bandpass with less losses, allowing faster readout, higher feedline reuse (more resonators inside the same feedline because of the increase of bandwidth) and higher isolation of the qubits and thus higher decay times as shown in simulations of Fig. 5.8. However, these filters need bulk-micromachining process which is time-consuming and requires specialized equipment and expertise. The filter design process and the circuit simulations using the BVD are mostly the same as the studied ones with SAW filters, only the layout and final implementation will change to adapt for XBAR resonators.

- The observed frequency shift that depends on the thermalization process needs to be taken into account when designing and operating acoustic filters for superconducting processors. Moreover, the use of off-chip Purcell filters in general complicates the manufacturing process and can add impedance mismatch errors and other uncontrolled parameters that shift the frequencies and leave some readout resonators unprotected.

These results provide useful insights and guidelines for future research and development of acoustic filters for quantum computing applications.

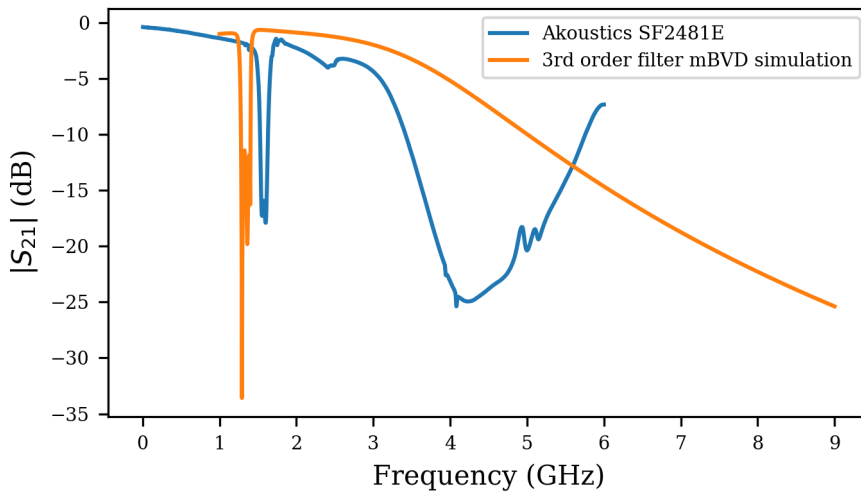


Figure 5.12: Circuitual simulation of a third order 1.3 GHz stopband filter using the BVD model for resonators (orange) and a transmission measurement of the Akoustis SF2481E 1.6 GHz stopband filter using thin film SAW resonators. In this comparison it can be seen that any acoustic stopband filter will have losses out of its operational band. Due to spurious the measured response being even worse in performance than the simulation with BVD models.

5.5 Evolution of the Lab and Advancements in Quantum Technology in Spain

This subsection provides a historical account of the evolutionary journey of our laboratory, showcasing its pioneering contributions to the field of quantum computing and quantum information processing in Spain. As one of the first students to participate in this distinguished industrial PhD program, my involvement in the lab's progression from its inception to its current status as a leading center for quantum research and development is also outlined. Despite limited resources during the nascent stages, the team's unwavering dedication to pushing the boundaries of quantum science fostered an environment of exploration and innovation. Fig. 5.13 visually captures the early lab setup, where researchers embarked on their ambitious pursuit of quantum technologies.

In the subsequent years, our lab achieved remarkable milestones that laid the foundation for groundbreaking quantum advancements in Spain:

2020: Introduction of the first cryostats and 3D transmon qubits, which proved crucial in calibrating subsequent setups and developing sophisticated code now utilized for our 5-qubit devices.

2021: Establishment of a second lab, broadening our experimental capabilities and contributing to comprehensive quantum exploration.

2022: Successful implementation of necessary instrumentation and components to effectively control up to 5-qubit devices, marking a leap forward in the lab's quantum capabilities.

2023: Projections to expand the first lab with two setups, one with 30-qubit instrumentation and another with 10-qubit instrumentation, both incorporating more professional software with automated calibration routines. Additionally, seamless integration of intervender instrumentation into Qililab facilitates enhanced collaboration and research potential.

2024: Relocation to a new and expanded facility, providing space for more setups and further advancements, solidifying the lab's status

as a leading quantum research hub.

Building upon foundational research, the laboratory achieved a significant breakthrough by developing the first quantum computers in Spain. Recognizing the importance of democratizing quantum computing and fostering widespread accessibility, the laboratory took strides towards progress by offering online access to its quantum computers [45, 47, 19, 29, 83]. This initiative allowed researchers and enthusiasts worldwide to remotely engage in quantum experiments, fostering collaboration and driving innovation in the field. These achievements represented a critical advancement in the country's quantum technology landscape, positioning Spain as a formidable player in the global quantum computing arena.

Looking ahead, our research endeavors aim to design and manufacture larger-scale quantum processors with an increased number of qubits capable of entangled communication. This requires a deeper understanding of various factors such as the impact of drive lines on qubits, optimized readout techniques, FPGA optimization, filter design, and other custom cryogenic components. Prioritizing thermalization and scalability is of paramount importance to achieve these goals. Additionally, detailed investigations into coupling mechanisms and electrical models are envisaged to gain insights into the underlying operations of these quantum structures.

Efforts to promote the accessibility and affordability of quantum computing remain a central aspect of our research agenda. We actively participate in the development of open-source software, cloud-based services, and user-friendly platforms that enable continuous testing and improvement of quantum computers, making them more accessible to researchers and the broader community.



Figure 5.13: Lab evolution over the years of this Industrial PhD thesis: 2020 to 2023.

Chapter 6

Conclusions and Future Work

The central focus of this doctoral thesis has been the exploration and advancement of quantum computers, with a specific emphasis on identifying the needs of quantum computers from a microwave engineering perspective. Throughout this work, we have presented comprehensive insights into various aspects of quantum computing, laying the foundation for further advancements in this rapidly evolving field.

In *Chapter 2*, we provided non-quantum engineers with a comprehensive introduction to the fundamental concepts of quantum computing. We explored the quantum information layer, delving into the Bloch Sphere representation of quantum states, the importance of one-qubit gates, and the use of the density matrix for characterizing quantum information. Additionally, we addressed the challenges of noise and decoherence in quantum computing and investigated the potential of Purcell filters in enhancing quantum measurements.

Chapter 3 focused on effective control and measurement strategies for qubits in quantum computing. We introduced the use of IQ modulation for precise quantum state control and explored digital signal processing techniques for qubit state determination. Addition-

ally, this chapter establishes a readout scheme that incorporates microwave instruments and cryogenic microwave components, enabling accurate measurement of qubit states in a quantum computing system. Furthermore, we introduced "Qilimanjaro's Quantum Operating System," a full-stack software framework developed for benchmarking QPU performance in quantum computers and executing quantum algorithms. This chapter also highlighted the significance of advanced microwave packaging techniques in enhancing quantum computing performance. The integration of microwave instruments and cryogenic components in the readout scheme, together with the Qilimanjaro's Quantum Operating System, provides a robust platform for characterizing and optimizing quantum processing units, paving the way for more efficient and accurate quantum computations.

Chapter 4 presented the design of our quantum processing unit (QPU) chips, featuring a single qubit prototype with a 3D transmon in a rectangular cavity resonator for enhanced qubit coherence. Additionally, we explored the potential of transmission line resonators for quantum computing and optimized their functionality through reflection measurements and data fitting. These design efforts pave the way for more robust and scalable quantum information processing.

In *Chapter 5*, we validated the methods and components discussed in *Chapters 3* and *4* by extensively characterizing and calibrating a single qubit performance, with a primary focus on readout. Moreover, we validated high-quality TLRs to achieve high quality factors and expected responses. This chapter also addresses the question of how to optimize readout pulses to accurately measure qubit performance, which is critical for achieving precise quantum state determination. By addressing these challenges, this chapter played a crucial role in defining and characterizing the building blocks of a QPU, encompassing resonators and qubits and achieving a state of the art 11 μs decay time as well as a 68% readout fidelity in our first qubit. We expect to increase the readout fidelity up to at least 90% with the use of a TWPA. The scripts developed in this chapter are reused for characterizing and calibrating more complex QPUs. Furthermore, we

explored considerations and current restraints on scaling up the first Quantum Computing prototypes, identifying research areas and market opportunities for microwave engineering. Finally, we embarked on a comprehensive exploration of acoustic wave Purcell filters as a potential avenue with various advantageous attributes like an extended and more consistent bandwidth, augmented stopband rejection, and a sharper bandpass-to-stopband transition. The resultant benefits create opportunities for closer placement of qubits to resonators in frequency. The advancements made here, along with the insights gained from this research, contribute to the continuous advancement of quantum computing and pave the way for future developments in the field.

As we look ahead, it is clear that quantum computing is still in its nascent stages, and many challenges lie ahead on the path to building large-scale, fault-tolerant quantum computers. The work presented in this thesis serves as a stepping stone toward this ambitious goal. As the field progresses, it will be essential to continue exploring novel methods for qubit control, enhancing qubit coherence and minimizing sources of decoherence. Moreover, efforts to improve qubit readout fidelity and optimize resonator design will play a pivotal role in realizing scalable quantum processors.

In conclusion, this doctoral thesis has made strides in advancing our understanding of quantum computing from a microwave engineering perspective. The research presented here has contributed to the development of QPU, effective control and measurement strategies for qubits, and resonator designs. As the journey towards practical quantum computing continues, the pursuit of novel solutions and innovative approaches remains vital to unlock the full potential of this transformative technology.

6.1 Microwave Engineering challenges in Superconducting qubit Quantum Computing

Superconducting qubit quantum computing holds immense promise in the pursuit of quantum advantage. However, this approach presents notable challenges in the realm of microwave engineering. In this section, we will explore these significant obstacles that researchers and engineers encounter while working on superconducting qubit quantum computing. These challenges play a crucial role in determining the feasibility and scalability of this quantum computing paradigm. By understanding and addressing these hurdles, we can pave the way for scalable and efficient quantum computers capable of achieving quantum advantage.

Low-Loss Microwave Components The successful operation of superconducting qubit systems hinges upon the utilization of microwave components with minimal signal loss. Among these, parametric amplifiers play a pivotal role by enhancing delicate microwave signals during the readout process. Formerly, the design of parametric amplifiers posed significant challenges. However, a recent breakthrough study by [65] has bridged the terminology divide between parametrically coupled circuits and band-pass/impedance matching networks. This integration now permits the application of network synthesis techniques from the field of microwave engineering to the creation of parametrically coupled devices.

Presently, only a handful of commercial providers offer TWPAs, with Silent Waves standing out as a notable startup. Nonetheless, TWPAs remain relatively high-priced and encounter obstacles in large-scale manufacturing. Similarly, the availability of cryogenic low-noise High Electron Mobility Transistor (HEMT) amplifiers is limited, with Low Noise Factory being the most prominent supplier. Another critical challenge lies in crafting compact, high-frequency connectors and

interconnections that ensure minimal loss and robust thermalization. Encouragingly, recent years have witnessed the emergence of commercial solutions aimed at tackling these interconnection hurdles, including Delft Circuits, Arden Concepts, and Scalingq.

Electromagnetic Interference Control Electromagnetic interference (EMI) is a significant challenge in superconducting qubit quantum computing because it can lead to errors in the measurement and control of the qubits. Shielding techniques, filtering techniques, and careful circuit design are required to address this challenge. EMI control is essential to minimize the impact of environmental noise on the performance of the qubit.

High-Fidelity Microwave Pulse Shaping Techniques Achieving accurate and efficient control of many qubits requires the implementation of high-fidelity microwave pulse shaping techniques. This involves the design of complex microwave pulses that can accurately manipulate the qubit states while minimizing errors due to imperfections in the microwave hardware. High-fidelity microwave pulse shaping techniques are essential for achieving the required level of precision and control necessary for superconducting qubit quantum computing.

Scalability Scalability is one of the key challenges in quantum computing, including in the field of microwave engineering. As the number of qubits in a quantum computer grows, the number of electronic and microwave components required increases. For instance, a simplified 3000- qubit setup would require 16000 attenuators, 500 TWPA, 1000 LNA, 6000 low pass filters, 3500 band-pass filters, and 9500 infrared filters, among other components, Fig. 6.1. This configuration would require around 100 racks, spanning the length of an Olympic swimming pool, solely to accommodate the RT electronics. However, it is currently impossible to fit all the needed lines and components inside a single cryostat, not only due to size but also due to the cooling

power needed to thermalize all of them, so multiple wired cryostats are needed like KIDE cryogenic platform from Bluefors.

Efforts are being made to develop scalable solutions, such as integrating filters in the same transmission lines that interconnect the stages of the DR using flex-PCB and stripline stepped-impedance filters embedded like the Cryoflex cables from Delft Circuits. Another approach is to investigate the use of cryo-CMOS technology [14] to reduce the number of electronic components needed outside the cryostat. However, this technology is still in its early stages and has only achieved the control of two qubits so far.

Regarding the readout of qubits, the current approach using a TLR for each single qubit is inefficient, as it results in a huge area of on chip just for resonators, in the 3000 qubit case we would need 3000 readout resonators, one for each qubit as shown in Fig. 6.1, and each resonator takes a space of at least 0.5 mm^2 , so the planar chip would take around 15 cm^2 which would induce several non desired resonant modes among other problems as thermalization. Researchers are investigating new ways of readout, including the use of 3D stack and flip-chip technology [20]. However, the challenge of connecting all the components remains, and new readout techniques are needed [57].

Despite the challenges, the potential benefits of quantum computing are significant, and research and development efforts are ongoing to improve their performance and capabilities. Advances in microwave engineering will play a critical role in the development of practical quantum computing systems based on superconducting qubits. However, it is important to carefully assess the suitability of quantum computers for specific tasks and to consider any potential limitations or challenges that may arise. The specialized infrastructure and expertise required to operate quantum computers can also limit their availability and accessibility to certain organizations or individuals [25].

In conclusion, the challenges in microwave engineering for superconducting qubit quantum computing are significant, but encouraging progress is being made to address them. The future of quantum

computing holds great promise, as ongoing research and development efforts are expected to lead to more advanced quantum computers with diverse applications. The collaborative effort between academia, industry, and government agencies remains crucial, drawing upon a multidisciplinary approach involving experts in physics, computer science, engineering, materials science, chemistry, math, etc.

As we continue to advance and scale up quantum processors, the development of reliable and standardized system models for quantum computing prototypes will pave the way for their potential industrialization. This will likely increase accessibility to quantum computing, driving further innovation and discoveries across various domains. The transformative potential of quantum computing is notable, with applications ranging from simulating quantum systems to optimizing logistics and cryptography.

While challenges persist, the collective dedication of researchers, industries, and governments worldwide is propelling us closer to realizing the potential of quantum computing. By addressing technical hurdles and fostering collaboration, we can contribute to unlocking the true power of quantum computing, which may have significant implications for computation and problem-solving in the 21st century and beyond.

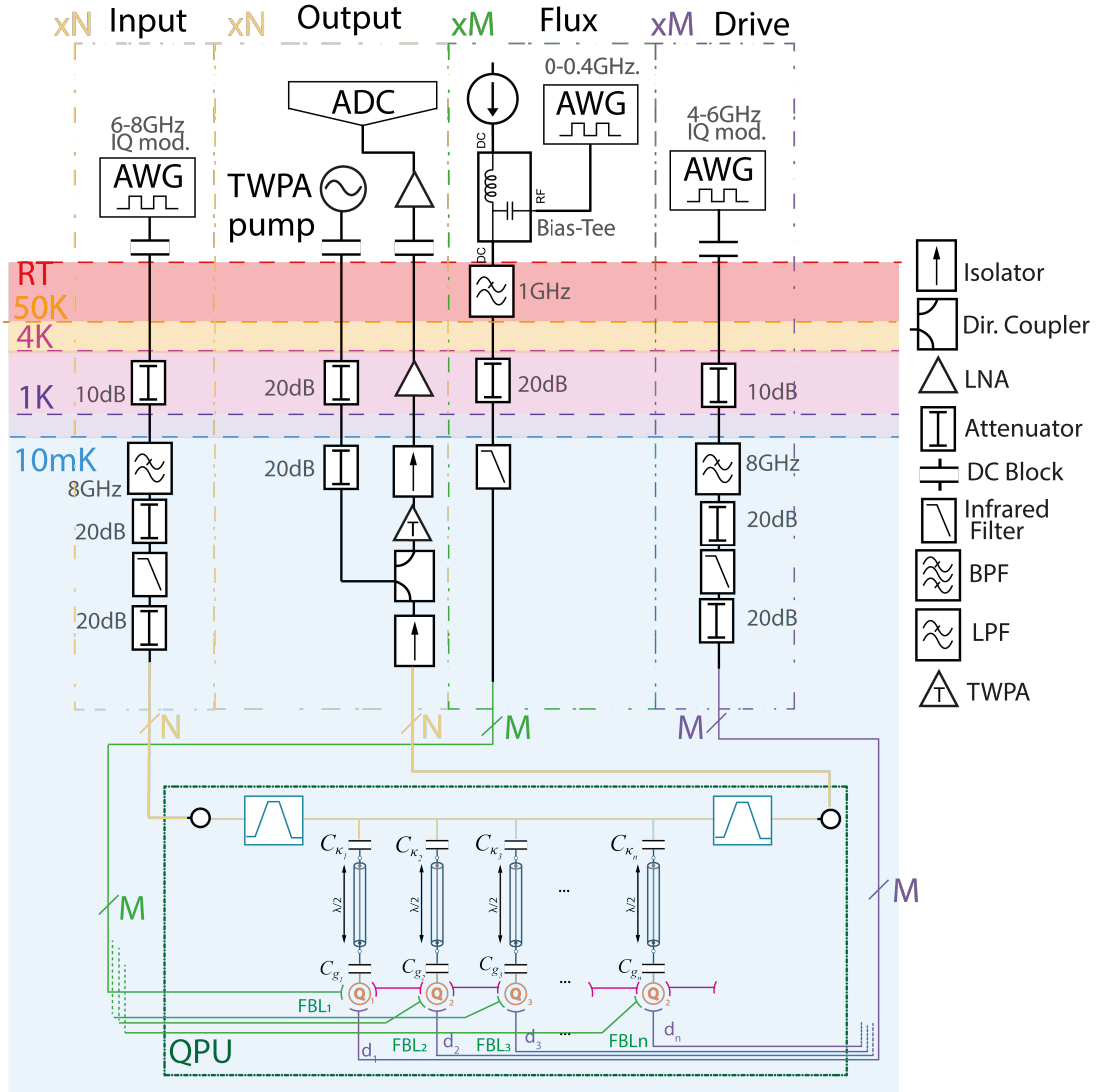


Figure 6.1: Schematic of setup for a simplified M qubit setup with 1 flux and one drive line for each qubit showing the main components and interconnections (assuming each feedline contains n qubits then $N=M/n$). In the case that $M=3000$ and $n=5$, the setup includes 16000 attenuators, 500 TPA, 1000 LNA, 6000 low pass filters, 3500 band-pass filters, and 9500 infrared filters among other components. The sheer number of components needed for such a setup highlights the scalability challenge in superconducting qubit quantum computing.

Bibliography

- [1] Akoustis. AKOUSTIS RFMi catalog. Technical report, 2022.
- [2] Artur García-Saez Albert Solana, Joel Pérez, Javier Sabariego, David Eslava. QIBO: THE OPEN SOURCE QUANTUM OS, 2022.
- [3] F. Arute. Quantum supremacy using a programmable superconducting processor. *Nature*, 574:505–510, 2019.
- [4] Serwan Asaad. *Exploring frequency re-use with transmon qubits in a cQED architecture*. PhD thesis, TU Delft, 2015.
- [5] A. S. Averkin, A. Karpov, K. Shulga, et al. Broadband sample holder for microwave spectroscopy of superconducting qubits. *Review of Scientific Instruments*, 85(10), 2014.
- [6] Harrison Ball, William D. Oliver, and Michael J. Biercuk. The role of master clock stability in quantum information processing. *npj Quantum Information*, 2(1), 2016.
- [7] Joseph C Bardin, Daniel Sank, Ofer Naaman, and Evan Jeffrey. Quantum computing for uW engineers. *IEEE Microwave Magazine*, 21:24–44, 2020.
- [8] Rami Barends. *Photon-detecting superconducting resonators*. PhD thesis, TU Delft, 2009.

- [9] Alexandre Blais, Arne L Grimsmo, S M Girvin, and Andreas Wallraff. Circuit quantum electrodynamics. *Rev. Mod. Phys.*, 93(2):25005, may 2021.
- [10] Alexandre Blais, Ren Shou Huang, Andreas Wallraff, S. M. Girvin, and R. J. Schoelkopf. Cavity quantum electrodynamics for superconducting electrical circuits: An architecture for quantum computation. *Physical Review A - Atomic, Molecular, and Optical Physics*, 69(6):1–14, 2004.
- [11] Nicholas T Bronn, Yanbing Liu, Jared B Hertzberg, et al. Broadband Filters for Abatement of Spontaneous Emission in Circuit Quantum Electrodynamics. *Applied Physics Letters*, pages 1–5, 2015.
- [12] C.C. Bultink. *Protecting quantum entanglement by repetitive measurement*. PhD thesis, TU Delft, 2020.
- [13] V. Canivell, P. Forn-Díaz, A. Garcia-Saez, and R. Sagastizabal. Startup Qilimanjaro-towards a European full-stack coherent quantum annealer platform. *EPJ Quantum Technology*, 8(1), 2021.
- [14] Edoardo Charbon, Fabio Sebastiano, Masoud Babaie, and Andrei Vladimirescu. *Cryogenic-CMOS for Quantum Computing*, pages 501–525. Springer International Publishing, Cham, 2020.
- [15] J. M. Chow. *Quantum information processing with superconducting Qubits*. PhD thesis, Yale University, 2010.
- [16] M Chow, D I Schuster, L Frunzio, and R J Schoelkopf. Fast Reset and Suppressing Spontaneous Emission of a Superconducting Qubit. *Applied Physics Letters*, 96(203110):1–4, 2010.
- [17] Agnetta Y. Cleland, Marek Pechal, Pieter Jan C. Stas, et al. Mechanical Purcell filters for microwave quantum machines. *Applied Physics Letters*, 115(26), 2019.

- [18] The Jupyter Book Community. Qiskit Textbook.
- [19] Computing.es. El primer computador cuántico español supera la primera fase, 2023.
- [20] C R Conner, A Bienfait, H.-S. Chang, et al. Superconducting qubits in a flip-chip architecture. *Applied Physics Letters*, 118(23):232602, jun 2021.
- [21] Andrew Cross, Ali Javadi-Abhari, Thomas Alexander, et al. OpenQASM 3: A Broader and Deeper Quantum Assembly Language. *ACM Transactions on Quantum Computing*, 3(3):1–50, 2022.
- [22] Andrew W. Cross, Lev S. Bishop, John A. Smolin, and Jay M. Gambetta. Open Quantum Assembly Language. 2017.
- [23] Daniel Thomas Sank. *Fast, Accurate State Measurement in Superconducting Qubits*. PhD thesis, UC santa barbara, 2014.
- [24] L DiCarlo, J M Chow, J M Gambetta, et al. Demonstration of two-qubit algorithms with a superconducting quantum processor. *Nature*, 460(7252):240–244, 2009.
- [25] Christian Dickel. A Cloud Quantum Computer Business Plan, 2018.
- [26] Stavros Efthymiou, Sergi Ramos-Calderer, Carlos Bravo-Prieto, et al. Qibo: a framework for quantum simulation with hardware acceleration. *Quantum Science and Technology*, 7(1), 2022.
- [27] David Eslava, Eloi Guerrero, Lluís Acosta, et al. Surface Acoustic Wave Filters for Superconducting Qubits. In *2023 IEEE/MTT-S International Microwave Symposium - IMS 2023*, pages 676–679, 2023.

- [28] David Eslava Sabaté and Pedro de Paco Sánchez. *Characterization and modeling of a coaxial cavity quadruplet based filter for mobile phone LTE-2 band*. PhD thesis, Universitat Autònoma de Barcelona, 2016.
- [29] Expansión. *Avanza la instalación del ordenador cuántico del BSC*, 2023.
- [30] Olivier Ezratty. Perspective on superconducting qubit quantum computing. *The European Physical Journal A*, 59(5):94, 2023.
- [31] Johannes Fankhauser. *Frequency-tunable Transmon qubit in a 3D copper cavity*. PhD thesis, ETH Zurich, 2016.
- [32] David A. Feld, Reed Parker, Richard Ruby, Paul Bradley, and Shim Dong. After 60 years: A new formula for computing quality factor is warranted. *Proceedings - IEEE Ultrasonics Symposium*, 6:431–436, 2008.
- [33] Jay Gambetta. *Quantum-centric supercomputing: The next wave of computing*, 2022.
- [34] Jay Gambetta, Alexandre Blais, M. Boissonneault, et al. Quantum trajectory approach to circuit QED: Quantum jumps and the Zeno effect. *Physical Review A - Atomic, Molecular, and Optical Physics*, 77(1):1–18, 2008.
- [35] Jiansong Gao. *The Physics of Superconducting Microwave Resonators*. PhD thesis, California Institute of Technology, 2008.
- [36] Yvonne Y. Gao, M. Adriaan Rol, Steven Touzard, and Chen Wang. Practical Guide for Building Superconducting Quantum Devices. *PRX Quantum*, 2(4):1, 2021.
- [37] Elizabeth Gibney. *Google Publishes Landmark Quantum Supremacy Claim*, 2019.

- [38] Jonathan Gnanadhas. *Microwave Circuit Analysis of Multi Transmon Qubit System*. PhD thesis, Delft University of Technology.
- [39] M. Göppl, A. Fragner, M. Baur, et al. Coplanar waveguide resonators for circuit quantum electrodynamics. *Journal of Applied Physics*, 104(11), 2008.
- [40] Emily Grumbling and Mark Horowitz. *Quantum Computing: Progress and Prospects*, volume 9781461418. 2018.
- [41] Eloi Guerrero, Lluís Acosta, Carlos Caballero, et al. On the Influence of Electrode Thickness in the Spurious Mode Reduction of Lithium Niobate-On-Insulator SH0Acoustic Wave Resonators. *IEEE MTT-S International Microwave Symposium Digest*, 2022-June:1037–1040, 2022.
- [42] Johannes Heinsoo, Christian Kraglund Andersen, Ants Remm, et al. Rapid High-fidelity Multiplexed Readout of Superconducting Qubits. *Physical Review Applied*, 10(3):1–13, 2018.
- [43] Jared B. Hertzberg, Eric J. Zhang, Sami Rosenblatt, et al. Laser-annealing Josephson junctions for yielding scaled-up superconducting quantum processors. *npj Quantum Information*, 7(1), 2021.
- [44] Dorit S Hochbam. Approximation Algorithms for NP-Hard Problems Introduction (Abridged). *ACM Sigact News*, 28(2):40–52, 1997.
- [45] Hpcwire.com. Qilimanjaro Advances Quantum Innovation in Spain with QaaS Delivery to BSC, 2023.
- [46] Sihao Huang, Benjamin Lienhard, Greg Calusine, et al. Microwave Package Design for Superconducting Quantum Processors. *PRX Quantum*, 2(2):1, 2021.

- [47] Interempresas.net. Qilimanjaro Quantum Tech y GMV superan la primera fase del proyecto Quantum Spain, 2023.
- [48] Frantisek Janicek, Anton Cerman, Milan Perny, et al. Applications of superconducting quantum interference devices. In *2015 16th International Scientific Conference on Electric Power Engineering (EPE)*, pages 429–432, 2015.
- [49] Evan Jeffrey, Daniel Sank, J. Y. Mutus, et al. Fast accurate state measurement with superconducting qubits. *Physical Review Letters*, 112(19):1–5, 2014.
- [50] Mercedes Jimenez Blasco. *A coupling matrix vision for mobile filtering devices with micro-acoustic wave technologies. A systematic approach*. PhD thesis, Universitat Autònoma de Barcelona (UAB), 2015.
- [51] X. Y. Jin, A. Kamal, A. P. Sears, et al. Thermal and Residual Excited-State Population in a 3D Transmon Qubit. *Physical Review Letters*, 114(24), 2015.
- [52] J Kelly, R Barends, A G Fowler, et al. State preservation by repetitive error detection in a superconducting quantum circuit. *Nature Physics*, 2015.
- [53] Jens Koch, Terri M. Yu, Jay Gambetta, et al. Charge-insensitive qubit design derived from the Cooper pair box. *Physical Review A - Atomic, Molecular, and Optical Physics*, 76(4):1–21, 2007.
- [54] Philip Krantz, Morten Kjaergaard, Fei Yan, et al. A Quantum Engineer’s Guide to Superconducting Qubits. *Applied Physics Reviews*, 6(021318), apr 2019.
- [55] Jerzy Krupka. Measurement of Permittivity, Dielectric Loss Tangent Float-Zone Silicon at microwave frequencies. *IEEE transactions on microwave theory and techniques*, 54(11):3995–4001, 2006.

- [56] Jerzy Krupka, Waldemar Karcz, Paweł Kamiński, and Leif Jensen. Electrical properties of as grown and proton irradiated floating zone silicon. *Nuclear Instruments and Methods in Physics Research Section B: Beam Interactions with Materials and Atoms*, 380:76–83, 2016.
- [57] Chuan-Hong Liu, Andrew Ballard, David Olaya, et al. Single Flux Quantum-Based Digital Control of Superconducting Qubits in a Multi-Chip Module. *arXiv*, (Mcm):1–15, 2023.
- [58] Ferdinand Loacker. *Design and characterization of a superconducting beam-splitter for quantum information processing*. PhD thesis, Technische Universität München, 2013.
- [59] J Majer, J M Chow, J M Gambetta, et al. Coupling Superconducting Qubits via a Cavity Bus. *Nature*, 449:443–447, 2007.
- [60] Vladimir E Manucharyan, Jens Koch, Leonid I Glazman, and Michel H Devoret. Fluxonium: Single Cooper-Pair Circuit Free of Charge Offsets. *Science*, 326(5949):113–116, 2009.
- [61] John M Martinis. Superconducting phase qubits. *Quantum Information Processing*, 8(2):81–103, 2009.
- [62] Adam Nykoruk McCaughan. *High-Q Superconducting Coplanar Waveguide Resonators for Integration into Molecule Ion Traps*. PhD thesis, Massachusetts Institute of Technology, 2010.
- [63] Corey Rae Harrington McRae, Haozhi Wang, Jiansong Gao, et al. Materials loss measurements using superconducting microwave resonators. *Review of Scientific Instruments*, 91(091101), 2020.
- [64] Stephanie Miller. *A tunable 20 GHz transmon qubit in a 3D cavity*. PhD thesis, Swiss Federal Institute of Technology Zurich, 2018.

- [65] Ofer Naaman and José Aumentado. Synthesis of Parametrically Coupled Networks. *Physical Review Applied*, 3(2):020201, 2022.
- [66] Mahdi Naghiloo. *Introduction to Experimental Quantum Measurement with Superconducting Qubits*. PhD thesis, 2019.
- [67] Y Nakamura, Yu. A Pashkin, and J S Tsai. Coherent control of macroscopic quantum states in a single-Cooper-pair box. *Nature*, 398(6730):786–788, 1999.
- [68] Isaac L. Nielsen, Michael A. and Chuang. *Quantum Computation and Quantum Information*. Cambridge University Press, 2011.
- [69] T P Orlando, J E Mooij, Lin Tian, et al. Superconducting persistent-current qubit. *Phys. Rev. B*, 60(22):15398–15413, 1999.
- [70] Hanhee Paik, D. I. Schuster, Lev S. Bishop, et al. Observation of high coherence in Josephson junction qubits measured in a three-dimensional circuit QED architecture. *Physical Review Letters*, 107(24):3–7, 2011.
- [71] Michael Peterer and Master Thesis. *Investigating the Suppression of External Sources of Decoherence in Transmon Qubits*. PhD thesis, ETH Zurich, 2012.
- [72] Luca Planat, Arpit Ranadive, Rémy Dassonneville, et al. Photonic-Crystal Josephson Traveling-Wave Parametric Amplifier. *Phys. Rev. X*, 10(2):21021, 2020.
- [73] James R. Powell. The quantum limit to Moore’s law. *Proceedings of the IEEE*, 96(8):1247–1248, 2008.
- [74] D. Pozar. *Microwave Engineering*. John Wiley Sons, Inc., 1990.
- [75] S Probst, F B Song, P A Bushev, A V Ustinov, and M Weides. Efficient and robust analysis of complex scattering data under

- noise in microwave resonators. *REVIEW OF SCIENTIFIC INSTRUMENTS*, 024706:7, 2015.
- [76] M. D. Reed, B. R. Johnson, A. A. Houck, et al. Fast reset and suppressing spontaneous emission of a superconducting qubit. *Applied Physics Letters*, 96(20), 2010.
- [77] B. Rosas. The Design and Test of Broadband Launches up to 50 GHz on Thin and Thick Substrates. Technical report, 2011.
- [78] Marco Roth. *Influence of Additional Pads on the Electrical Properties of a 3D Transmon*. PhD thesis, 2015.
- [79] A. Sain. *A Study On The Effects Of Ground Via Fences , Embedded Patterned Layer , And Metal Surface Roughness On Conductor Backed Coplanar Waveguide*. PhD thesis, The University of Arizona, 2015.
- [80] D. I. Schuster, A. A. Houck, J. A. Schreier, et al. Resolving photon number states in a superconducting circuit. *Nature*, 445(7127):515–518, 2007.
- [81] D. I. Schuster, A. Wallraff, A. Blais, et al. Ac Stark shift and dephasing of a superconducting qubit strongly coupled to a cavity field. *Physical Review Letters*, 94(12):1–4, 2005.
- [82] David I. Schuster. *Circuit Quantum Electrodynamics*. PhD thesis, 2007.
- [83] Sciencebusiness.net. BSC: Spanish consortium to install first quantum computer in southern Europe, 2023.
- [84] Eyob A Sete, John M Martinis, and Alexander N Korotkov. Quantum theory of a bandpass Purcell filter for qubit readout. *Physical Review A*, pages 1–15, 2015.

- [85] Peter W. Shor. Polynomial-time algorithms for prime factorization and discrete logarithms on a quantum computer. *SIAM Journal on Computing*, 26(5):1484–1509, 1997.
- [86] Michaël Simoen. *Parametric interactions with signals and the vacuum*. PhD thesis, Chalmers University of Technology, 2015.
- [87] Rainee N. Simons. *Coplanar Waveguide Applications*, volume 7. 2003.
- [88] Southwest. Optimizing Test Boards for 50 GHz End Launch Connectors Grounded Coplanar Launches and Through Lines on 30 mil Rogers 4350 with Comparison to Microstrip. Technical report, 2007.
- [89] Kevin A Delin Terry Orlando. *Foundations of Applied Superconductivity*. ADDISON-WESLEY, 1991.
- [90] Jordi Verdu. *Bulk Acoustic Wave Resonators and their Application to Microwave Devices*. PhD thesis, Universitat Autònoma de Barcelona, 2010.
- [91] A. Wallraff, D. I. Schuster, A. Blais, et al. Approaching unit visibility for control of a superconducting qubit with dispersive readout. *Physical Review Letters*, 95(6):2–6, 2005.
- [92] Edward Xie. *A scalable 3D quantum memory*. PhD thesis, TECHNISCHE UNIVERSITÄT MÜNCHEN, 2018.

Appendix A

Crafting Cryogenic Cables with NbTi Superconductors for Quantum Processing Units

This appendix provides information on constructing NbTi superconducting cables used to establish cryogenic temperature access to the quantum processing unit. These cables are critical to transmitting microwave signals in the C-band (4-8 GHz) from room temperature electronics to the quantum processing unit, which operates at 10 mK. The construction and soldering process must be precise to meet a stringent 20 dB return loss specification and minimize losses. Any mismatch in the cables at these frequencies can distort the pulses sent to the qubits, leading to errors in quantum computing and measurements.

To ensure a strong and reliable connection, NbTi, a superconducting material, is used in the construction of these cables. The soldering process for NbTi differs from standard procedures due to the metal's hard nature and lack of adhesion to regular tin. An ultrasonic soldering station and a specialized tin called CERASOLZER are used

to achieve a secure bond. CERASOLZER contains trace amounts of elements such as Zn, Ti, Si, Al, Be, and Rare Earth metals, which have a strong chemical affinity with oxygen. During the bonding process, these metals combine with oxygen in the air to form oxide, which is then chemically bound to the surface of the glass, ceramics, metal oxide, etc.

It is worth noting that a comprehensive guide for soldering these types of cables was not found, so this appendix provides an overview of the process that has been successfully developed and tested. The 2.19mm NbTi coaxial cables used in this process come from Coaxco in Japan. The use of such a large diameter and superconductor material minimizes losses, but as the computer scales in the number of qubits, smaller alternatives are needed for thermalization. Superconducting materials are also 10 times more expensive than other materials like CuNi, which can be used for less critical lines.

There are other techniques available for assembling these cables, such as using flux or oxidation techniques or having copper at the ends of the cable, which prevents the use of ultrasonic soldering. Clamping connectors is also an option. It should be noted that while the technique described in this appendix is effective for achieving the best matching and minimizing losses, it is not scalable. However, companies are currently working on scaling these processes.

A.0.1 Process followed for Assembling superconducting high quality NbTi coaxial cables

1. Calculate the required length of cable before bend. Each cable needs to take into account the stage to stage space of the fridge, add the extra length that the bending of the cable will add and subtract the length of attenuators, connectors and other components.
2. Cut the desired cable length using cut pliers (these semirigid coaxial cables are usually bought in 1m batches).

3. Tag the cable with unique identifier. The identifier should include the stage of temperature, the material and the line of usage of this cable.
4. Cut 2mm of cable ends with table-top dremmel.
5. Mark (not cut) 5mm of external shield with table-top dremmel.
6. With flat pliers break the outer shield (too much bend here can deform the teflon and inner pin).
7. Thermalize: the teflon needs to come out at least 3 mm for each side. Apply heat with the heat gun with a bit of an angle pointing the teflon. Don't overdo the thermalization, you shouldn't see the cable changing colour (meaning oxidation of the metal due to excess of temperature) when it starts to do so rotate the cable.
8. Remove imperfections of the cut. This is done by applying some scotchbrite and polishing with algodón mágico. Later, clean the corrosive chemicals of algodón mágico with isopropanol.
9. Let the ultrasonic solder, USS-9210 AIR MkII from MBR electronics, heat up to 335° and prepare a mixture 1/1 (usually with 0.5cm is enough) of CERASOLZER GS120 and CERASOLZER CS297 on a glass plate using also hot air to level 2-3.
10. Fix the ultrasonic solder looking upwards with a vice. Set it to 250-280° and hot air activated.
11. Apply some tin (prepared mixture in step 7) on the tip of the solder.
12. Apply the tin in the outer shield. 0.5cm or so. I recomend to rotate the cable and do circular movements. A thin layer of the prepared tin should stick to the outter shield. Press the pedal to activate the ultrasonic vibration just when there is

good surface contact between outer shield and soldering tip. No longer than 5 sec. in a row. Clean the tip periodically to remove excess of solder or burnt solder tin.

13. Cut the dielectric with special craft knife. The cut should be perfectly straight at 90° with the outer shield.
14. Cut the center pin to be 2.54mm with the small side cut pliers. (assuming ezform non magnetic SMA connectors (every connector has it's distance)). For the 4K to 1K cables we use the Johnson (Cinch) SMA connectors (same as for CuBe cables) but for the 1K to MXC you should use the non magnetic ones, which also have the teflon part and the outer connector separated.
15. Reshape the tip to be a bit conical with the small sandpaper and 45° angle. If you apply too much strength the tip will bent and the cable will be useless.
16. Clean the tip with isopropanol.
17. Fix the ultrasonic solder looking upwards with a vice. Set it to 350° . (hotair OFF).
18. Apply some tin , CERASOLZER CS297 , on the tip of the solder.
19. Fix the connector center pin with the third hand soldering stand. Put the inner part of the connector as far out as it is stable so that you have more surface to heat with the solder tip.
20. Introduce the soldering tin (normal one) until you see it through the hole. Apply heat to the connector center pin with the solder tip. The needed amount of soldering tin should remain inside the connector center pin.

21. Heat the inner connector while you introduce the tip of the cable. The connector should be heated with a clean soldering tip. I recommend the spoon tip. The soldering of the tip should be fast, otherwise you overheat and cause problems to the teflon. Ideally it should not touch the teflon. If done right the connector center pin should look like a cylinder without visible hole. The tin must not be too much so to go out of the hole or too little just to make the hole visible. These errors can be more or less reworked although the optimal procedure is to get it good at the first try. If too tin gets out of the hole you can wait until cold and remove with the craft knife. (if too strength is applied the pin will bent and the cable will remain useless). If too little tin is applied the hole is visible. You can place some extra tin in the hole with a very thin solder tip.
22. Place the outer connector. If it doesn't fit it means too much solder was applied to the outer shield. Put the cable perpendicular to a surface that can stand heat (connector touching the surface) and heat the zone between cable and connector while pushing. This also needs to be fast enough not to burn the teflon or overheat the connector that can make the center pin to desolder again. The ultrasonic tip must be used since we are using special soldering tin but no need to use ultrasound.
23. Put CERASOLZER CS186 tin between cable and connector and give some quick heat with ultrasonic solderer at 340° and hot air.
24. Fix the ultrasonic solder looking upwards with a vice. Set it to 340° and hot air. Give some lateral angle this time. 15° angle or so.
25. Place a SMA female to the connector to be soldered and wear thermal protection gloves to protect you from burning.
26. Use the ultrasonic solderer to solder the outer connector to

the cable. I also recommend to rotate the cable and move the solder tip from cable to connector until the contact surface looks flat and a bit conical. Only connector body heated by hot air. This is a critical step since if no enough strength is applied on top of the connector or too much time is spent, the connector will move and shortcircuit with the inner pin and will leave the cable completely useless. First around the cable, later around the conector, the connector gets lossy then pressure and rotate the connector. Finally wait 20s mantaining the pressure.

27. Check continuity with multimeter to ensure that the shielding has not been shortcircuited with the center pin.
28. Repeat the first 27 steps for the other end of the cable to solder the other connector.
29. Measure the cable using the VNA. To do so, connect the cable at the end of the VNA measuring cable of port 1 and recall state containing the calibration of this measuring cable. After this, connect a 50ohm load at the end of the assembled cable and measure S_{11} magnitude in dB. If the $|S_{11}|$ is below -20dB for the whole range (300 KHz to 8-5 GHz) the cable is good for use and trace is plotted in Fig. A.1b.

Additionally in Fig. A.1b we test the assembled cables inside cryostat at room temperature before cooling down the system. The setup inside the cryostat follows a configuration similar to Fig. 6.1 without filters or TWPA. Measurement at room temperature of three drive lines blue, orange and green. The three of them with identical configuration and 50 dB attenuation. Measurement from RT input of the criostat to the MXC using a VNA. Readout line (red) at room temperature bypassing at MXC from input to output. Showing proper signal transmission after the 50 dB attenuation of the input line and amplification of the amplification chain consisting of LNAs at 4K and RT.

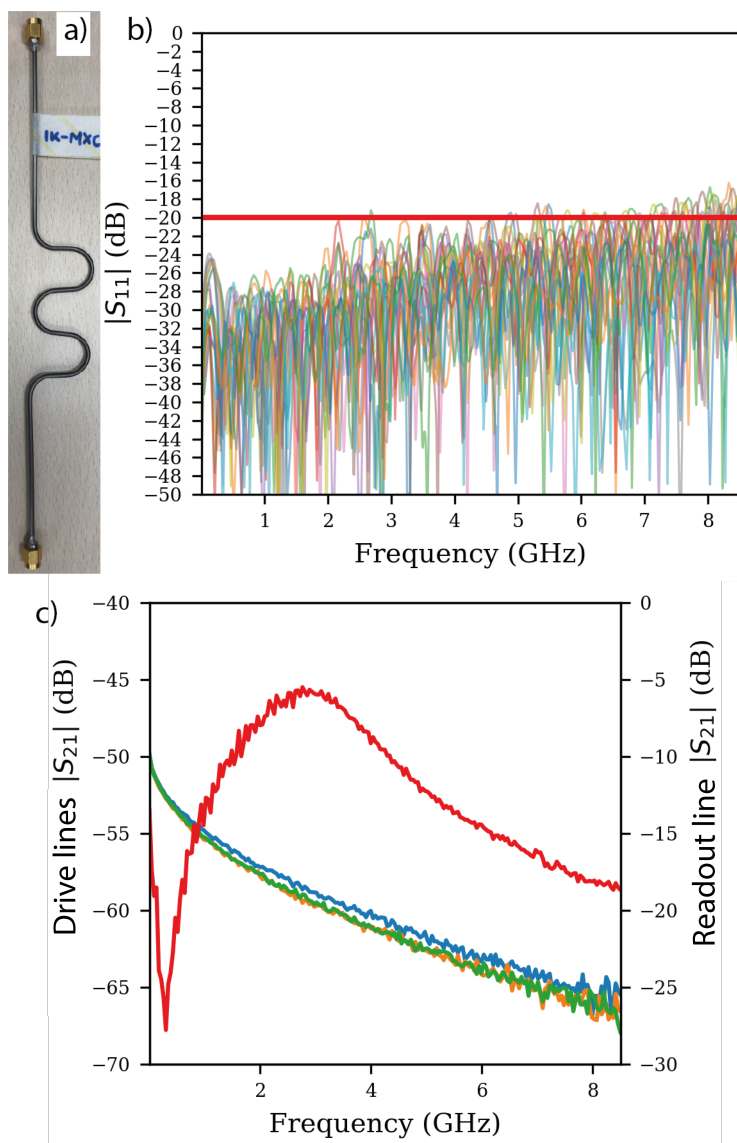


Figure A.1: (a) Sample of high quality rigid coaxial cable assembled following the guide. The bends are needed to avoid connector breakage due to thermal expansion and also to add some flexibility in the cables for mounting. (b) Reflection measurement with a 50 ohm load at the other end of 36 cables that were assembled correctly showing >20 dB RL. (c) Measurement of the bypassed readout line (red) and three drive lines (other three colors). More details in text.

Appendix B

List of Author's Contributions

B.1 International Congress

1. A. Solana, J. Pérez, J. Sabariego, D. Eslava, A. García-Saez, “QIBO: THE OPEN SOURCE QUANTUM OS”, *Superconducting Qubits and Algorithms.*, 2022. [2]
2. D. Eslava, E. Guerrero, L. Acosta, P. Jamet, Y. Chen, J. Pérez, C. Hensel, A. Solana, D. Szombati, R. Sagastizabal, P. de Paco, P. Forn-Díaz, “Surface Acoustic Wave Filters for Superconducting Qubits”, *American Physical Society March Meeting.*, 2023.
3. D. Eslava, “Building a Quantum Computer in an Industrial Situation”, *Spring School on Superconducting Qubit Technology.*, 2023
4. D. Eslava, E. Guerrero, L. Acosta, R. Sagastizabal, P. Jamet, P. Forn-Díaz, P. de Paco, “Surface Acoustic Wave Filters for Superconducting Qubits”, *International Microwave Symposium.*, 2023. [27]

